Nonequilibrium statistical physics applied to biophysical cellular processes

Kate E P Sugden

Doctor of Philosophy
The University of Edinburgh
2009

Abstract

The methods of statistical physics are increasingly being employed in a range of interdisciplinary areas. In particular, aspects of complex biological processes have been elucidated by bringing the problems down to the level of simple interactions studied in a statistical sense. In nonequilibrium statistical physics, a one dimensional lattice model known as the totally asymmetric simple exclusion processes (TASEP) has become prominent as a tool for modelling various cellular transport processes. Indeed the context in which the TASEP was first introduced (MacDonald et. al., 1968) was to model ribosome motion along mRNA during protein synthesis. In this work I study a variation of the TASEP in which particles hop along a one dimensional lattice which extends as they reach the end. We introduce this model to describe the unique growth dynamics of filamentous fungi, whereby a narrow fungal filament extends purely from its tip region while being supplied with growth materials from behind the tip. We find that the steady state behaviour of our model reflects that of the TASEP, however there is an additional phase where a dynamic shock is present in the system. I show through Monte Carlo simulation and theoretical analysis that the qualitative behaviour of this model can be predicted with a simple mean-field approximation, while the details of the phase behaviour are accurate only in a refined approximation which takes into account some correlations. I also discuss a further refined mean-field approximation and give a heuristic argument for our results. Next I present an extension of the model which allows the particles to interact with a second lattice, on which they diffuse in either direction. A first order mean-field continuum approximation suggests that the steady states of this system will exhibit some novel behaviour. Through Monte Carlo simulation I discuss the qualitative changes that arise due to the on-off dynamics. Finally I study a model for a second biological phenomenon: the length fluctuations of microtubules. The model describes stochastic polymerisation events at the tip of a microtubule. Using a mean-field theory, we find a transition between regimes where the microtubule grows on average, and where the length remains finite. For low rates of polymerisation and depolymerisation, the transition is in good agreement with Monte Carlo simulation.

Declaration

I do hereby declare that this thesis was composed by myself and that the work described within is my own, except where explicitly stated otherwise.

Kate E. P. Sugden
March 5th 2009

Ackowledgements

Thank you Martin[1] for your dedicated guidance, support and good humour throughout my Ph.D. Thanks also Wilson[2], for taking me to the bio side and for your continued support and advice; and Graeme Ackland, Nick Read and Graham Wright for helpful discussions.

I'd also like to give a special thanks to Jean-Luc Beaumont, Albrecht Ott and all those involved in the best summer school ever, in St Etienne de Tinée, Les Alpes Maritimes. The PHYSBIO school was one of the true highlights of my Ph.D. and I'm ever grateful for having had the opportunity to take part.

An especial thanks also to my fantastic 4306-, 4305- and latterly 2510-mates: it has been a pleasure and an honour. Also to all those within and outside the department who have offered their time and critical thinking on the topics of my thesis at some point or another.

And finally, thank you to (extended) family, Cosmo, and all those with whom I've played basketball, made music, watched good films, eaten mochis, drunk tea and bicycled during my post-graduate years.

---

[1] M.R. Evans, my principal supervisor

[2] W.C.K. Poon, my secondary supervisor

Contents

Chapter 1

Introduction

The force that through the green fuse drives the flower, drives my green age; that blasts the roots of trees...

Dylan Thomas

From the times of the Greek philosophers, until the early 20th Century, conventional wisdom held that even the lowliest of living cells must be stirred by a force unique to life; something above and beyond the forces and energies of the inorganic universe. In the last century, the concept of 'vital forces' has largely been replaced in the scientific realm, with the belief that even in something as mysterious and astounding as a living organism, what goes on inside can be described within the laws of physics. Biology, thus provides a limitless playground for the physicist.

The challenge of biophysics is to use the tools and concepts developed in physics to gain insight into biological processes. With the help of massive advances in computing power and microscopic imaging techniques, the field has developed rapidly in the last thirty years [Egelman 07]. However, in the study of complex and little-understood living systems, physicists are constantly coming up against the frontiers of our understanding of physics itself. Biophysics thus goes hand-in-hand with the development of new analytical techniques, and the pursuit of a deeper understanding of the origins of some of the more subtle physical phenomena.

Of special relevance to biological systems, (and the topic of this thesis) is the physics of systems which are out of equilibrium [Stinchcombe 01]. Most systems in nature are indeed just that. This means, for example, that the methods of statistical physics, which were developed for dealing with systems comprising a very large number of particles [Feynman 98], and which so elegantly allow us to make predictions about the macroscopic properties of equilibrium systems, are not in general applicable. A unified framework for nonequilibrium physics, like that of the Gibb's free energy formalism in equilibrium statistical physics [Huang 87], is still highly sought after [Crooks 99, Derrida 01, Blythe 01, Ruelle 03, Kurchan 07].

One of the standard practices of statistical physics is to envisage the dynamics of a system that is made up of very many parts as a series of stochastic transitions from one microscopic configuration (i.e. a set of positions, velocities and accelerations for each particle) to another, where the next configuration depends only on the present configuration and not on the history of the system. This type of chain of events is called a Markov chain. In order to distinguish between an equilibrium and a nonequilibrium system, it is useful to consider whether the Markov chain is reversible according to a principle known as *detailed balance*. Detailed balance is characteristic of an equilibrium system and hails from the intrinsic time reversal symmetry of classical mechanics. It states that for every pair of configurations C and C', the probability of the system being in configuration C and transforming into configuration C' is equal to the probability of the converse. Every transition is balanced in probability with its reverse transition. For a nonequilibrium system, detailed balance is not necessarily present. For example, it may be that a driving force such as an electric current or a difference in chemical potential causes particles to flow preferentially in a particular direction through the system. This can cause the emergence of a rich spectrum of complex behaviours that are neither observed in equilibrium systems nor explained with equilibrium physics.

Because of the lack of a general theory, one of the primary tools for unearthing the fundamental principles of nonequilibrium systems is through the study of the behaviour of simple models, often based on low dimensional lattices. A large number of simple models have been introduced and studied intensively over the past two or three decades. See e.g. [Privman 97] for an overview. Of these, many have found relevance in, and indeed been motivated by, a variety of problems outside of pure theory; not least in the area of biophysics. It thus becomes apparent that there is something of a symbiotic relationship between nonequilibrium statistic physics and biophysics. In our attempt to explain biological systems using physics, we are forced to recognise that while existing tools are useful, they are not complete. It is therefore important to develop our ideas in nonequilibrium physics, and we may do so by studying models motivated by biological problems. As such, the two fields are developing simultaneously.

The combination of nonequilibrium physics and biology is today a broad and active area of research [Physbio 07], encompassing a great number of fascinating and diverse problems. At a glimpse, these include topics such as the physics of gene regulation [Lässig 07], the statistics of RNA conformations [Bundschuh 05], the theory of complex natural networks [Palla 05], cellular mechanics, motility and the cytoskeleton [Kruse 05, Nishinari 05], the hydrodynamics of collections of bacteria [Stark 06] and aspects of pattern formation in biology [Deutsch 05]. The work in this thesis, also, sits on the interface between these two subjects.

Let us look now at the contents of the thesis. This work is primarily a theoretical study of two models, which were constructed with the aim of capturing the essential features of two different systems appearing in biology, namely the growth of narrow fungal filaments known as hyphae, and the dynamic instability of microtubules, which perform important roles within a cell. The techniques employed in the construction and analysis of these models hail from statistical nonequilibrium physics, and the models, while helping us to gain some physical insight into these biological processes, also serve to further our understanding of nonequilibrium behaviour in general.

I begin (in Chapter 2) by reviewing the totally asymmetric simple exclusion process (TASEP). This is a one-dimensional model for a driven, diffusive system: one of the paradigms of nonequilibrium statistical physics. It is this model that forms the basis of the following work, and as such, I proceed by using it as an example to introduce some of the techniques used for studying models of this type. The techniques include mean-field approximation, kinematic wave theory and Monte Carlo Simulation.

The TASEP model was originally introduced to describe a biological transport process, and it remains an important player in the field of biophysics. I review some of the biological studies that have been made using models based on the TASEP, before going on to introduce a novel biological system to which the TASEP can be applied: that of fungal hyphal tip growth.

Fungal hyphal tip growth has been a source of great intrigue to biologists for many years. To a fungus, the ability to form polarised tubes, which grow into its surroundings is of key importance to its survival and to its role within the ecosystem. The scenario sounds simple enough: a tube that is filled with cytoplasm extends from one end. Yet the questions of how the tip maintains its polarity and a steady growth velocity remain central and largely unanswered.

Our present understanding of the growth mechanism of a fungal hypha is based on studies of the detailed infrastructure of the hyphal tip, which I overview (in Subsections 2.2.1–2.2.2). I discuss several of the models which have been proposed to explain the observations, before presenting (Subsection 2.2.3) a new model, based on the TASEP, which incorporates an extending system size. We argue that this can serve as a coarse grained model for the growing hyphal tip. The analysis of this model is the topic of Chapter 3, where we determine through mean-field approximation techniques and Monte Carlo simulations, the stationary state properties of the model and its phase diagram.

After characterising the basic model, we discuss (in Chapter 4) a more detailed picture of the dynamical process leading to fungal hyphal tip growth, and we extend the model of Chapter 3 to encompass this extra detail. The new model has some extra degrees of freedom and we therefore expect that the qualitative behaviour may be different from that of the original model. We carry out a qualitative analysis (Section 4.3), in order to determine the new stationary behaviour, again appealing to techniques of mean-field approximation. The results are explored with the aid of Monte Carlo simulation (Section 4.4).

The second subject of interest in this work concerns a microscopic model for the phenomenon of *dynamic instability* of microtubules. Dynamic instability is the name given to the process whereby a microtubule within a cell undergoes a series of polymerisation and depolymerisation events, resulting in large fluctuations in the length of the microtubule. These fluctuations are vital to the functions performed by microtubules within a cell, and as such much research effort has been directed towards the modelling and understanding of this dynamic system.

One of the challenges in modelling microtubule dynamic instability has been to use the least detail to reproduce the observed types of stochastic growth patterns. Prevalent in the literature, is the concept of a so-called *GTP-cap* which stabilises the tip of the microtubule and thus has a central role in the dynamics of the length fluctuations. A microscopic model which encompasses the role of a GTP-cap in the dynamic instability of microtubules has previously been found to be successful in predicting periods of microtubule growth and decay that are in keeping with observation. We are interested to discover whether one can identify a phase transition for this model, between a regime where a microtubule is growing unbounded and one where the microtubule ultimately remains of finite length. We approach the problem using techniques that have been developed in Chapter 3, and arrive at a new result, which we probe with Monte Carlo simulations of the model. The simulation results reveal the successes and limitations of our approach.

In summary, the thesis is organised as follows: Chapter 2 contains the background to all the work, including both an introduction to the relevant topics of theoretical nonequilibrium statistical physics, and a full biological background to both of our problems of interest. The next two chapters, Chapter 3 and Chapter 4, are devoted to the theoretical analysis of the model which we develop to describe fungal hyphal growth in the framework of nonequilibrium statistical physics. In Chapter 5, we move on to the study of a model for microtubule dynamic instability; and finally, some concluding remarks are made in Chapter 6.

Chapter 2

Background

The work in this thesis is of an interdisciplinary nature and as such, I must introduce in this chapter both the relevant theory of nonequilibrium statistical physics and the biological background to our problems of interest.

I begin with the theory, which is the backbone of our subsequent work. The focus here is on one of the fundamental models of nonequilibrium statistical physics, the totally asymmetric simple exclusion process (TASEP). This model has found broad application in the field of biophysics, while also playing an important role in the theoretical study of nonequilibrium phenomena. After introducing the model, I outline some of the techniques used to study it (which we shall be employing later in our study of a related model). I then go on to discuss its history of application to biophysical problems.

In the next section, I give a detailed discussion of the current understanding of a very interesting nonequilibrium problem in biology: the growth and maintenance of growth of a fungal hypha. This problem has been studied within the biological sciences for many years, and some of the features of growth have been described with the help of mathematical theories. It has not, however, been approached from the perspective of nonequilibrium statistical physics. After reviewing the complex structures and processes believed to be involved in the growth mechanism, I propose a novel model for fungal growth, based on the TASEP.

The final section in this chapter is an introduction to a second biological problem, not entirely unrelated to the first one: the dynamic instabilities of microtubules. In common with a fungal hypha, this system has a non-conserved system size. I discuss the current biological understanding of this phenomenon, and review a recent study of a microscopic model based on these ideas. Finally, I pose an open question regarding this microscopic model.

This provides the context and tools required for progressing to the analytic Chapters 3–5, where we explore in depth our model for fungal hyphal tip growth, and address our question on the topic of dynamic instability.

2.1 Nonequilibrium physics: models and methods

A major branch of nonequilibrium statistical physics is concerned with the study of simple models which are designed to embody the essential dynamics of the system's constituent parts. It has been discovered through the study of these simple models that even in one-dimension, a system through which particles are driven by an external force (a driven diffusive system) is capable of exhibiting non-trivial behaviour such as phase ordering and phase separation [Evans 00]. The interest in such phenomena is equally motivated by a desire to understand the dynamic principles behind nonequilibrium macroscopic behaviour, as it is by a diverse range of possible applications across biology, chemistry and physics [Privman 97].

2.1.1 Asymmetric simple exclusion processes and the TASEP

I begin by introducing a one dimensional model known as the *asymmetric simple exclusion process* (ASEP). This is one of the simplest models of a driven diffusive system and has thus provided a starting point for those wishing to understand some of the behaviours peculiar to nonequilibrium systems [Evans 02]. This type of model has also been a popular choice for studying transport problems in biology, because it naturally lends itself to the description of transport processes associated with molecular motor motion within cells (See Subsection 2.1.5 later, for a discussion).

The ASEP consists of a one dimensional lattice along which particles can hop, with some bias in direction. The only constraint on the particles is that they are mutually exclusive, i.e. no more than one particle can occupy the same lattice site. It describes in a simple sense a system which is held far from equilibrium, i.e. particles moving subject to an external force such as charged particles in an electric field; or particles moving between two differing potentials such as when transferring between reservoirs of different chemical potential. Although the ASEP is now widely considered one of the fundamental models for simple nonequilibrium systems [Blythe 07], its history is rooted in biological physics. The concept was originally introduced by MacDonald [MacDonald 68] in 1968 to model ribosome motion along messenger RNA during the synthesis of proteins. Many variations on the ASEP theme have since been introduced to describe different biological systems, for example exclusion processes with modified boundary conditions, multiple particle types with different hopping probabilities, 'defective' lattice sites where the particle dynamics are altered and long range hopping dynamics, amongst others. Some of these models will be discussed in 2.1.5.

For now, we shall consider a special case of the ASEP: the open boundary *totally asymmetric simple exclusion process* (TASEP). In this model particles hop along the one-dimensional lattice in a single direction only. At the lattice boundaries particles are injected at one end and extracted from the other end with rates α and β respectively, which are the only control parameters for the model. In the bulk of the lattice, the hops occur with uniform rate 1. Figure 2.1.1 illustrates the TASEP schematically. The particle transitions occur stochastically, with transition rates defined as the probability per infinitesimal time interval of a transition occurring. Since the TASEP particle hopping rate is unity, in an infinitesimal time interval dt, a hop will be attempted with probability dt.

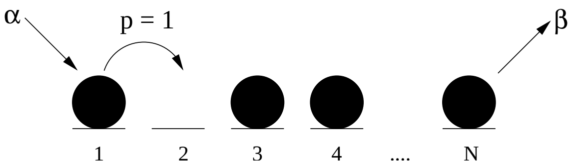

Figure 2.1: A schematic of the TASEP. Particles enter at the left with rate α, hop forward one site with rate 1 and are extracted from the right-most site with rate β. Particle transitions can occur only when the target site is vacant.

The behaviour of the system is categorised in terms of its *steady state phases.* A steady state is reached when the 'density' of each site, that is the time-averaged occupancy, no longer changes with time. Equivalently, when the system is in a steady state, the current of particles hopping along the lattice is the same everywhere. The phases are distinguished by the system's macroscopic properties in the large system limit i.e. the density profile across the lattice and the particle current between any two neighbouring lattice sites. Phase transitions are induced by varying the boundary conditions, controlled by parameters α and β.

The exact phase behaviour of the TASEP is well understood from an exact analytical solution [Derrida 93, Schütz 93] as well as mean-field [Derrida 92] and other approaches [Blythe 07]. Three distinct steady state phases exist. For low input, $\alpha < 0.5$, and $\alpha < \beta$, the system is in a low density phase, where the bulk of the lattice is equal to α and the current is equal to $\alpha(1-\alpha)$. At $\alpha = \beta$, there is a discontinuous phase transition and the system enters a high density phase, now limited by a low output rate $\beta < 0.5$. The bulk of the lattice in this phase is at a high density equal to $1-\beta$ and the current is equal to $\beta(1-\beta)$. When α and β are both > 0.5, the system enters a phase of maximal current. The transition to this phase is continuous. Here the system is no longer controlled by the input and output rates, instead the bulk density is 1/2 and the current is 1/4. Furthermore, the density profile decays algebraically from the boundaries towards the bulk value 1/2. The results are summarised in the phase diagram of Figure 2.1.1.

2.1.2 Time evolution equation and the mean-field approximation

The analysis of the TASEP requires first a mathematical description of the particle dynamics. This can be formulated as follows: Consider the expectation that a particular lattice site i is occupied by a particle. We denote this $\langle \tau_i \rangle$, where τ_i is *occupancy* and can take a value 0 or 1, and the angle brackets denote the statistical average. Correspondingly, the expectation that a site i is not occupied is $\langle 1 - \tau_i \rangle$. These expectation values are functions of time, and we are interested in how they evolve towards a steady state where

$$\frac{d\langle \tau_i \rangle}{dt} = 0 \quad \forall i \ .$$

Now to find an expression for $\frac{d\langle \tau_i \rangle}{dt}$ consider what happens to τ_i when a particle

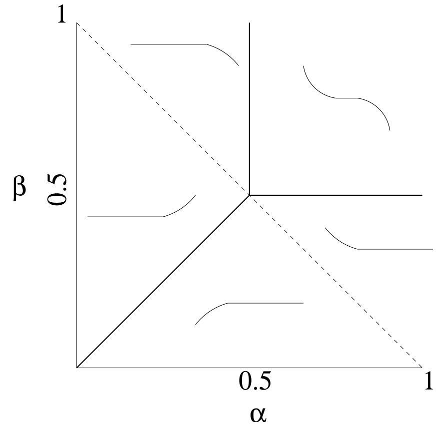

Figure 2.2: The phase diagram of the TASEP, deduced from exact results, mean-field approximation and other methods. Three phases are present: high density phase (lower right portion), low density phase (left-most portion) and maximal current phase (top right portion). Schematic density profiles in the respective phases are also indicated.

transition occurs. Denoting the original occupancy τ_i and the occupancy after the transition τ_i', we have:

$$\tau_i \rightarrow \tau_i' = \tau_i + \tau_{i-1}[1-\tau_i] - \tau_i[1-\tau_{i+1}] \; . \tag{2.1}$$

i.e. If $\tau_i = 0$ and $\tau_{i-1} = 1$, then site i gains a particle from neighbouring site $i-1$; if $\tau_i = 1$ and $\tau_{i+1} = 0$, site i loses a particle to neighbouring site $i+1$. Now let us consider how the occupancy changes with time. In a discrete time step dt, a transition occurs with probability dt, thus the expectation value for the occupancy at time $t+dt$ can be written as:

$$\langle \tau_i(t+dt) \rangle = \langle \tau_i(t)' \rangle dt + \langle \tau_i(t) \rangle (1-dt) \; , \tag{2.2}$$

which simply states that with probability dt, the occupancy transforms to τ_i', while with probability $1-dt$ it remains unchanged. Equation 2.2 along with (2.1), and taking the limit $dt \rightarrow 0$, gives us the exact equation for the time evolution of $\langle \tau_i(t) \rangle$:

$$\frac{d\langle \tau_i \rangle}{dt} = \langle \tau_{i-1}(1-\tau_i) \rangle - \langle \tau_i(1-\tau_{i+1}) \rangle \tag{2.3}$$

Note however that solving (2.3) is not a trivial matter. The right hand side contains both one-point and two point correlation functions. One must therefore first find the two point correlations, which in turn require higher order correlation functions, and so on, until every correlation in the system is included in the equation. At this point we may find we wish to make some simplifying approximations.

A standard approach is to simply assume that the correlations are small and can be neglected. In this case, we may make the factorisation:

$$\langle \tau_i \tau_j \rangle = \langle \tau_i \rangle \langle \tau_j \rangle \tag{2.4}$$

This is generally understood as a *mean-field* approximation. The master equation becomes a function of one-point correlations only, and along with the boundary conditions forms a closed system of equations. In a few special cases, including the TASEP [Mukamel 00], the mean field approximation leads to the exact phase diagram.

2.1.3 Kinematic wave theory

A concept which proves very useful when considering the solutions to equations of the type (2.3), is that of kinematic wave theory. This formulation was introduced by Lighthill and Whitham in 1955 [Lighthill 55] as a means of understanding one dimensional flow problems. They postulate that if there exists an approximate functional relationship between the particle current J and the particle density ρ at each point in some flowing system, then points of constant density propagate through the system with a velocity given by $\partial J/\partial \rho$. The evolution of the density can thus be described as a travelling wave, which the authors coin a kinematic wave.

The theory follows from the conservation law:

$$\frac{\partial J(\rho)}{\partial x} + \frac{\partial \rho}{\partial t} = 0 \; . \tag{2.5}$$

Supposing that $J = J(\rho, x)$, then we may define

$$c = \frac{\partial J}{\partial \rho} \; ,$$

and rewrite 2.5:

$$\frac{\partial \rho}{\partial t} + c\frac{\partial \rho}{\partial x} = 0 \; .$$

This first order nonlinear partial differential equation is solved with the arbitrary wave function:

$$\rho = f(x_0 - ct)$$

i.e. ρ is constant at points in space that are travelling with velocity c.

Since the wave velocity c is a function of ρ, points of different density propagate through the system with different velocities. The kinematic waves can thus collide and amalgamate. When this occurs, the solution to 2.5 is multi-valued [1], and a discontinuity in the density arises. The discontinuity, sometimes referred to as a *shock* or *domain wall*, propagates through the system with a velocity derived from mass conservation. If we label the current and density on either side of the discontinuity $J_\pm$ and $\rho_\pm$, then the shock velocity is,

$$v_{shock} = \frac{J_+ - J_-}{\rho_+ - \rho_-} \; . \tag{2.6}$$

Kinematic waves provide us with a useful phenomenological description of how

---

[1] Technically at this point, the equation 2.5 breaks down, however the phenomenological description is still valid.

information propagates through a one dimensional flowing system. In the case of an open boundary problem such as the TASEP, we may understand it as a mechanism by which information from the boundaries of the system can penetrate its bulk. The dynamics of the shock can be thought of as the result of a competition between the effects of the two boundaries, with the dominant boundary condition driving the shock toward the opposing boundary.

Kinematic wave theory and the TASEP phase diagram

We can use the theory of kinematic waves to explain the phase behaviour of the TASEP. By considering the shock dynamics, controlled by the boundary rates α and β, one can identify all of the phases described above, in Subsection 2.1.1.

We start by expressing Equation (2.3) in terms of particle current J:

$$\frac{d\langle\tau_i\rangle}{dt} = \langle\tau_{i-1}(1-\tau_i)\rangle - \langle\tau_i(1-\tau_{i+1})\rangle = J_{i-1,i} - J_{i,i+1} \ . \tag{2.7}$$

Taking a mean-field approximation and assuming that the density is varying slowly enough that we may denote $\langle\tau_i\rangle = \langle\tau_{i+1}\rangle = \rho$, we deduce an approximate current-density relation:

$$J = \rho(1-\rho) \tag{2.8}$$

From this, we find the kinematic wave velocity associated with a particular density,

$$c = 1 - 2\rho \ ,$$

and the velocity of the shock:

$$v_{shock} = 1 - \rho_1 - \rho_2$$

where subscripts 1 and 2 denote regions to the left and right of the shock respectively. To meet the boundary conditions, the density at the site furthest to the left is α, and at the other boundary it is $1-\beta$. If the input and output rates are less than 0.5, then the kinematic waves associated with each boundary will move into the bulk of the system. The resulting shock wave will travel with a velocity $v = \beta - \alpha$, which tells us immediately that the direction of the shock changes when $\alpha = \beta$. For $\alpha > \beta$, the shock travels to the left boundary and the density in the bulk of the system is $1-\beta$. For $\alpha < \beta$, the shock travels to the right boundary and the bulk density is α. When $\alpha > 0.5$, the kinematic wave does not penetrate the system from the left boundary. A wave originating from the right boundary will thus travel unimpeded to the left. Conversely, if $\beta > 0.5$ a kinematic wave originating from the left boundary will travel all the way to the right boundary. For both α and β greater than 0.5, the kinematic wave velocity associated with each boundary is directed out of the system, and no shock forms. Here the density profile evolves according to second order terms which were neglected in this theory. The resulting phase diagram is the same diagram exactly as was presented in Figure 2.1.1.

2.1.4 Monte Carlo simulation

Numerical simulations are an invaluable tool for studying the problems of statistical physics, which by nature consist of very many particles and degrees of freedom. Not only are they useful for testing the validity of our theories, but also for guiding us in our analytics and for providing answers when analytic solutions are impossible to come by. The most prominent numerical technique in the field of statistical physics is Monte Carlo simulation. The key idea of the Monte Carlo simulation is to simulate the random fluctuations of a system by employing random numbers to explore the set of microstates.

Much of the emphasis in developing Monte Carlo simulations is on how to map a physical system onto a lattice model, which can then evolve according to some dynamic rules, leading ultimately to a correct probability distribution [Newman 99]. In the case of nonequilibrium statistical physics, many of the models are already defined on a lattice, and as such, the Monte Carlo simulations are fairly straightforward to implement.

As an example, consider the TASEP. Provided rates α and β are less than 1, this can be implemented simply as follows:

1. Construct an array of N Boolean values $\tau_i \quad i = 0..N-1$
2. Select an element i from the array at random
3. Attempt to update the element:
    - if $i = 0$ and $\tau_0 = 0: \quad \tau_0 \to 1$ with probability α
    - else if $i = N-1$ and $\tau_{N-1} = 1: \quad \tau_{N-1} \to 0$ with probability β
    - else if $i = 0..N-2$, $\tau_i = 1$ and $\tau_{i+1} = 0: \quad \tau_i \to 0$ and $\tau_{i+1} \to 1$ with probability 1
    - else do nothing.
4. For each Monte Carlo time step, repeat steps $(2-3)$ N times.

Typically, the system will take several thousand time steps to relax to a steady state (depending of course on the system size N), after which one may begin measurements on the steady state properties of interest.

Note that in this type of algorithm, known as a *discrete time algorithm*, the success rate of transitions is sometimes extremely low. For example if the lattice is very highly populated, the majority of sites chosen will not be eligible for update since their neighbouring site is already occupied. In this case, one can sometimes greatly increase the efficiency of a simulation by considering instead a *continuous time algorithm*, such as the Gillespie algorithm [Gillespie 77]. Rather than choosing a site at random, the continuous time algorithm chooses from a list of possible update events. In this way, one update is performed at every time interval Δt. The choice of event is random, but weighted by the relative rates of the different transitions. The time increment Δt is calculated according to the sum of all the possible rates out of the present configuration i.e.

$$\Delta t = \frac{1}{\sum\limits_{\mu \neq \nu} p(\mu \to \nu)} ,$$

where $p(\mu \to \nu)$ indicates the transition rate from configuration μ to configuration ν.

Although this algorithm has the advantage of eliminating all null transitions, it has added complexity in that it requires at all times the knowledge of all the possible moves out of the current configuration. Depending on the system, the extra computational time required to keep a list of possible transitions up to date can outweigh the advantages of this algorithm over the discrete time algorithm.

2.1.5 Exclusion process models in biophysics

Over the years the application of the TASEP has been wide and varied, but in particular it has been shown to lend itself to the modelling of transport phenomena in biology, for example the motion of molecular motors along microtubule filaments, and on a larger scale, the motion of ants along a pheromone trail [Hinsch 05, Chowdhury 05].

In order to capture the essence of specific biological processes, the TASEP has been augmented with many additional features. While the added complexity often makes model analysis considerably more involved, many variations have been tackled successfully, resulting in the emergence of some interesting and novel behaviour.

Here I give a brief tour of some of the biophysical problems which have been approached with models of TASEP inspiration in recent years. In collating the key results of these models, I build up a general picture of the behaviour of the exclusion processes, and illustrate the extent to which the TASEP phase behaviour is robust to variations in the details of the model mechanics.

The first application of an exclusion process in biology was in 1968 [MacDonald 68]. The aim of this seminal work was to study the procession of ribosomes, which move along a strand of messenger RNA (mRNA) to synthesise a protein. They argue that since several ribosomes move along a single strand of mRNA at once, the effects of collective motion of the ribosomes would have significant effects on protein synthesis rates. Furthermore, ribosomes are unable to overtake each other or simultaneously occupy the same mRNA site, suggestive of exclusive dynamics on a one dimensional track. The model they devised was exactly the TASEP. The ribosomes are identified with the particles and the lattice sites are identified with the mRNA subunits (codons). It is in this paper that the phase diagram presented in Section 2.1.1 was first derived, using a mean-field approximation.

The idea of the TASEP as a model for protein synthesis was carried forward in [Lakatos 03] and [Shaw 03], where the effect of allowing particles of larger spatial extent on the lattice was studied. This extension to the model was to mimic more closely the ribosomes, which are known to cover more than one site at a time as they progress along the mRNA. In [Lakatos 03], the generalised properties of the TASEP dynamics such as the steady state current and phase diagram for particles of arbitrary size d are derived. Qualitatively similar phases to the TASEP are present in this model, but the phase boundaries are shifted significantly for different values of d. The phase diagram remains symmetric in $\alpha - \beta$, while the transition to the maximum current phase is shifted to a lower value of α and β. This is rather intuitive result, as the larger particle size means that less particles are required in the bulk of the system before their collective effects become significant. In the case of $d = 1$, the properties of the TASEP are recovered.

Also related to the synthesis of proteins is a work [Szavits-Nossan 06], which allows the particles to make long range hops. The idea here is that before beginning the protein translation process, ribosomes search for a target site on the mRNA by temporarily disassociating from it and rebinding at a different site. If the ribosome remains within the electrostatic potential of the mRNA, then the new site will be spatially correlated to the old one. In this model the hopping distances are hence selected with a probability that decays as a power law with distance. For a strong power law decay, the phase diagram is found to be unmodified from the TASEP, while the current is altered by a factor depending on the power law exponent. The character of the phase transitions however was found to be affected, since here long range correlations are important. One effect is the localisation of the domain wall at the phase transition between high and low density phases.

A great many works have been motivated by the study of the collective motion of molecular motors such as kinesin, myosin and dynesin along microtubules and actin filaments. Molecular motors are biological structures which are able to convert chemical energy from the organic compound adenosine triphosphate (ATP) into mechanical energy [Howard 02]. They are a vital component of all eukaryotic cells as they are involved in the transport of materials and organelles from one part of a cell to another, in chromosome positioning during cell division and also in organism locomotion itself, e.g. through the contraction of muscle fibres. The motors process by interacting with associated polymer filaments (microtubules for kinesin and dynesin, and actin microfilaments for myosin). The polymer filaments act as tracks, on which the motors perform a directed motion of discrete steps. That many motors can process along a single polymer filament is what makes the TASEP a natural choice for modelling this traffic-like phenomenon.

In [Chowdhury 08], the authors use TASEP based models to treat the motion of various molecular motors with an analysis inspired by traffic science. They suggest that many of the features of vehicular traffic also apply to molecular motor traffic. The quantities they discuss are the current-density relation and the distance and time head-way distributions. In this work and several others, the biochemical processes involved in the motor motion are also incorporated. The authors argue that the stochastic motion of the motors depends on a pathway of chemical reactions, which they include in the models by introducing further particle states. Their results show promising quantitative agreement with experimental imaging of real motor distributions on microtubules [Greulich 07]. Some of the theoretical results however, such as the distance head-way distribution, are found to be independent of the particular biochemical process.

The inclusion of further particle states was also studied in [Reichenbach 06] which allows a particle to be in one of two states, and allows multiple occupancy of a single site provided the particles are in different states. The model is proposed for several applications including the representation of hydrolysed and unhydrolysed motors on filament tracks. Particles on the lattice can switch between states or move to an adjacent site with different rates. The resulting behaviour is very interesting. The authors find a large region of the $\alpha - \beta$ phase diagram in which there is phase coexistence. Here a domain wall separates regions of different densities. The wall's position is localised in space and depends on the three model parameters of input rate, extraction rate and state switching rate. This two-state scenario was found to be equivalent to a two lane TASEP, studied in [Helbing 01].

The multilane TASEP is relevant to biological transport phenomena since cells often contain several filament tracks, which the motors are free to transfer between. This leads us to a consideration of utmost importance when studying molecular motor transport; that during a typical transport process, a molecular motor will progress along a microtubule for a short time only, before unbinding from it and diffusing into the surrounding cytoplasm. At a later time the motor may reattach to the microtubule, or to another microtubule and continue along its directed path. A motor will thus only reach the end of a microtubule after a series of unbinding and binding events. This feature is known as 'processivity' and has been incorporated into the TASEP dynamics in several works.

In [Parmeggiani 03, Parmeggiani 04], a model is studied which combines the TASEP with Langmuir kinetics. It is assumed that the concentration of molecular motors in the cytoplasm is large, and can be represented by a reservoir with which particles on the lattice are able to exchange. Two new parameters are introduced to control the rate at which a particle can leave the lattice, and the rate at which a particle from the bulk reservoir may attach to a vacant site of the lattice. The transfer of particles between this bulk reservoir and the lattice is an equilibrium Langmuir process, while on the lattice the nonequilibrium driven dynamics of the TASEP remain. It was found that when the rates of attachment and detachment are small, so that a particle processing from one end of the lattice to the other will only leave the lattice with a rate comparable to the boundary rates, there is a competition between the bulk Langmuir kinetics and the normal boundary effects of the TASEP. As in the previous two-state/two-lane case, the resulting phase diagram includes whole regions where the density profiles exhibit a domain wall or *shock*, between two coexisting phases. This is in contrast to the TASEP, which only has a shock solution on the transition line between the high and low density phases, $\alpha = \beta$.

Another attempt to integrate the on-off dynamics of motors was taken in [Klumpp 03]. In this work the unattached motors are explicitly taken into account by coupling a second lattice to the TASEP, which represents the unattached motors. Since the unattached motors are freely diffusing, they can hop in either direction with equal rates. These dynamics describe a *symmetric* simple exclusion process (SSEP). The outcome of this model was a modified phase diagram, but qualitatively unaffected phases. Later it was shown that a TASEP coupled to a SSEP in the limit of strong symmetric coupling is equivalent to a so-called *partially* asymmetric simple exclusion process (PASEP), while weak couplings revert the model to TASEP like behaviour [Tsekouras 08]. In all cases studied, the phases of the TASEP are present, with phase boundaries controlled by the strength and symmetry of the couplings.

The above review is in no way extensive, but serves as an introduction to the role that TASEP type models are currently playing in the field of biophysics. Many other important contributions have been made in recent years [Campás 06, Evans 03, Klein 05], some of which are reviewed in [Chowdhury 05]. The many variations from a common base model are helpful in providing a broad picture of the effects of different model components on the overall TASEP behaviour.

2.2 Fungi

The inspiration for the main body of our work comes from a problem in fungal biology that has been a topic of intense research for many years: the growth mechanism of filamentous fungi. Fungi form a hugely important biological group which includes, amongst the lesser known organisms, mushrooms, moulds and yeasts. As a taxonomic group, they are distinct from both plants and animals and there are an estimated 1.5 million species of fungus in the world [ToL]. For a comprehensive introduction to the kingdom of fungi and its human significance see e.g. [Deacon 06].

The importance of fungi within the environment cannot be underestimated. While many species form mutually beneficial symbiotic relationships with plants and animals, fungi are also powerful pathogens. Dutch elm disease, chestnut blight and corn smut are all examples of the destructive capabilities of fungi. Their role within the environment is also as decomposer of organic matter; a vital part in the cycle of nutrients.

To man, fungi also have direct importance [Kavanagh 05]. Species of fungus are used extensively in medicine (antibiotics i.e. penicillin), food manufacture (yoghurt, beer, bread) and industry (lactic acid, enzymes, detergents). On top of this, fungi are of great interest genetically as they have many shared physiological properties with animal cells. For this reason they are important model organisms for the study of gene function. Indeed, the fungal species *Neurospora crassa* was one of the first species to have its genome fully sequenced [Galagan 03].

Most species of fungus are made up of a fruiting body, e.g. mushroom, along with a network (often hidden underground) of fine filaments called the *mycelium.* The mycelium is responsible for exploring the environment and uptaking nutrients. (And explore it does: the mycelium of one fungus of the *Armillaria ostoyae* species has been recorded to have reached a size of 2200 acres, qualifying it as the largest known organism! [Ferguson 03]) The filaments of the mycelium, or *hyphae*, grow in such a way that they are able to penetrate even hard organic matter, and it is largely this ability that gives fungi their special status within the ecosystem. Figure 2.3 shows the hyphae of three common fungal species.

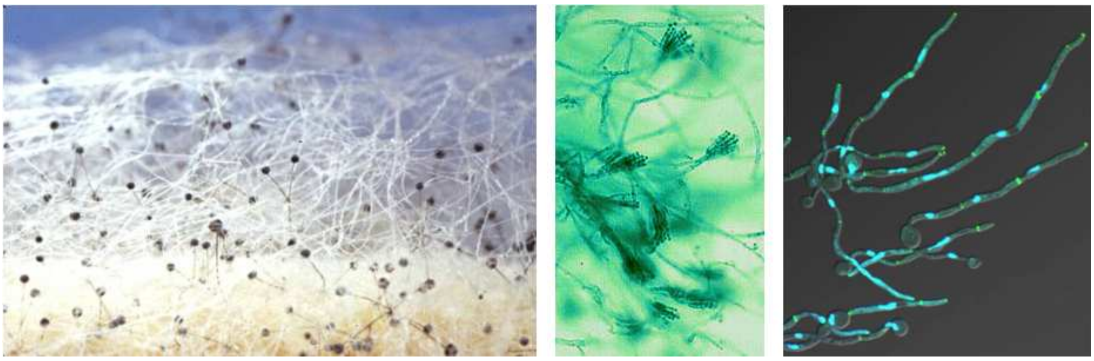

Figure 2.3: From left to right: *Rhizopus stolonifer*, a common bread mould, showing the interwoven hyphae of the mycelium; Hyphae of *Penicillium chrysogenum*, widely found in nature and the source of several antibiotics including penicillin.; *Candida albicans*, a type of yeast found in the human gut that can cause dangerous infections. (Images L-R from www.encarta.msn.com, www.biology.iastate.edu, www.natureasia.com:©Indragit Sinha.)

2.2.1 Fungal hyphal tip growth

Because of its fundamental role in the specialist functions of fungi, the growth mechanism of fungal hyphae has attracted a great deal of attention [Gow 95]. The defining feature of this growth is that it is highly polarised, occurring primarily at the tips of the hyphae. It is this essential physiological trait, known as *apical growth*, that gives the hypha tip the ability to apply enough force to penetrate hard matter.

In the very simplest sense, a fungal hypha is an extending tube between $1 - 10\mu$m in diameter, that is filled with cytoplasm, organelles, enzymes and proteins moving continuously towards the tip [Riquelme 07]. At the site of growth, the enzymes and materials required for cell building interact with the cell wall, causing the local elongation of the hypha tip. The result is the rapid and polarised growth of the hypha into its surrounding environment. Figure 2.4 shows a hyphal tip of the fungus *Neurospora. crassa*, captured over the course of approximately five minutes, illustrating the rapid extension achieved within short periods of time.

The full description of fungal hyphal growth however, necessarily involves an extremely complex interplay of biophysical processes including cytoskeletal dynamics and organisation, intracellular transport processes, turgor pressure, endo- and exocytosis, lysation of the cell wall, and precise intracellular organisation. Indeed, determining the exact roles of each of these components in the apical growth of fungal hyphae is still a very active area of research [Bartnicki-García 02, Bezzi 03, Harris 05]. Many of the current ideas and progress in the biology of fungal cell growth have been reviewed recently in [Steinberg 07a]. The essential points are summarised below.

Tip infrastructure and growth

The exact biochemical make-up of the hyphal tip is still under investigation, though many elements have been identified in studies employing electron microscopy [Vargas 93] (See

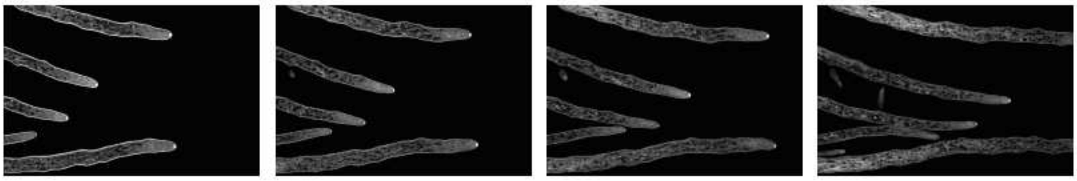

Figure 2.4: The apical growth of *Neurospora crassa* hyphae, captured at approximately 1.25 minute intervals. Each hypha is of approximately 10 μm diameter.

e.g. Figure 2.5, discussed later). Inside the cytoplasm are small sacs known as vesicles. These are of varying sizes and are thought to contain the cell wall building materials. Microtubules and actin filaments are also observed, along with their associated motor proteins. These are organised in a variety of configurations depending on the species. Ribosomes responsible for protein synthesis, and protein processing centres known as golgi apparatus are also present, but the area directly behind the tip is dominated by vesicles.

Enclosing it all is the cell wall, which is tubular, with a parabolic dome shape at the tip and an increasing degree of plasticity as the apex of the tip is approached [Wessels 94]. The wall is made up of a matrix of fibres such as chitin and glucan chains. In order to expand in a polarised fashion, fibres at the tip must be soft and susceptible to pressure, while those at the sides must solidify into the final tubular shape. The expansion during growth has been shown to be orthogonal across the growth area [Bartnicki-García 02], implicating turgor as a provider of the physical force for the expansion.

Directly behind the hyphal tip of many species of filamentous fungi is a conspicuous accumulation of vesicles, known in the literature as the *Spitzenkörper*. First discovered in [Girbardt 57], this dense vesicle cloud has attracted a great deal of attention in the search for understanding the mechanism of fungal growth [Löpez-Franco 96]. Its position has been shown to be inextricably linked to the direction of growth and shape of the tip: most convincingly in experiments where optical tweezers are used to manipulate the Spitzenkörper position, revealing its direct influence on the direction of tip growth [Bracker 97, Wright 07].

Mounting evidence exists in support of the importance of the cytoskeleton in maintaining polarised growth of hyphae [Schuchardt 05, Steinberg 07b]. The cytoskeleton consists of actin microfilaments, microtubules and their associated motor proteins. It is of structural importance to cells as well as being the basis for intracellular transport processes [Seiler 97, Seiler 99]. Both actin microfilaments and microtubules are present in fungal hyphae, and experiments inhibiting either structure result in dramatic disruption to normal apical growth and hyphal tip shape [Torralba 98, Horio 05]. Inhibition of the motors associated with microtubules, namely kinesin [Wu 98] and dynein [Riquelme 00] have also resulted in a reduced growth rate, and the loss of polarity. Given the importance of the Spitzenkoi̇per in determining growth direction, these findings suggest that the cytoskeleton is also involved in the positioning of the Spitzenrkoi̇per [Riquelme 98].

The actin filaments have been shown to have a vital role in the initial emergence of a

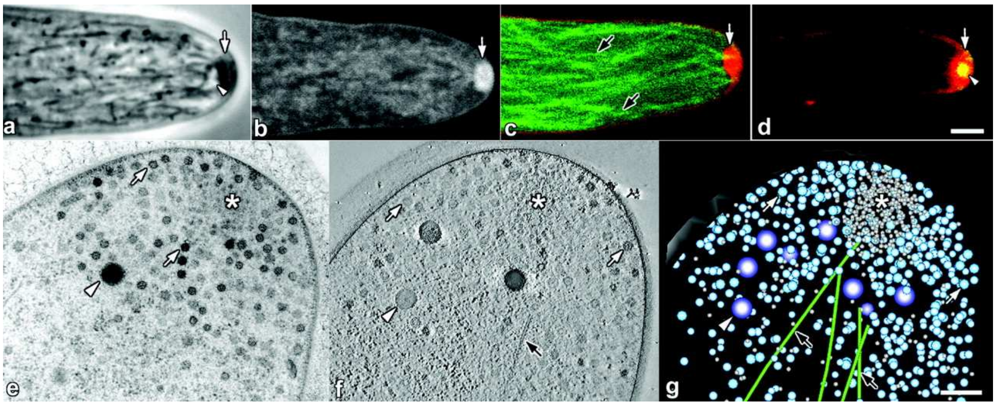

Figure 2.5: (a to d) Live-cell imaging of growing hyphal tips of *N. crassa* (a to c) and *A. nidulans* (d) treated with various dyes. The Spitzenkörper is clearly visible, composed of a cloud of secretory vesicles (arrows) and a bright core (arrowheads). Microtubules (black arrows) can be seen extending into the Spitzenkörper. Scale bars = 2.5 μm. (e to g) Transmission electron micrographs of a hyphal tip of *A. nidulans*. These images show a cluster of microvesicles within the Spitzenkörper core (asterisks) surrounded by apical vesicles (white arrows), electron dense spheres (white arrowheads), and microtubules (black arrows). (g) Is a model of image (f), showing the 3D distribution of cytoplasm through an ≈ 170 nm thick section. Scale bar = 250 nm. (Image from [Harris 05].)

hypha from a germtube [Harris 99] and are believed to be primarily involved in the short distance transport of materials from the region of the Spitzenkörper to the apical wall. Microtubules on the other hand are believed to be important for the long range transport of vesicles to the growth zone [Fischer 08]. In [Mouriño-Pérez 06], confocal microscopy provides clear images of the distribution of microtubules within the model species *N. crassa* (See Figure 2.5(c)). The microtubules are visible as dynamic populations of loosely entwined filaments, which extend into the hyphal tip and associate with the Spitzenkörper, consistent with their proposed role.

The key physiological features of a typical growing fungal hypha can be seen in the live imaging and electron microscopy images of Figure 2.5, including the Spitzenkörper, microtubules and vesicles.

2.2.2 Theoretical models for a growing fungal hypha

Drawing from the observations discussed above, several biological hypothesis for the mechanism of fungal hyphal tip growth have emerged in the modelling literature. These are summarised below:

Steady state model

[Wessels 86] This model aims to explain the mechanism of cell wall expansion at the tip. It assumes that polymer chains are delivered to the growing region of the hyphal apex in a plastic state and that the hyphal tip grows as a result of pressure from the cytoplasm, coupled with a gradual rigidification of the new cell wall. The 'steady state' refers to the balance between the rates of deposition and ridigification of the new wall building material, allowing for the constant expansion of a uniformly shaped tip. This model however does not provide a quantitative explanation for the particular shape of the tip.

Vesicle supply centre model

[Bartnicki-Garcia 89, Gierz 01, Tindemans 06] This model is based on the belief that the softening and building of the hyphal apex is the result of vesicles fusing with the cell wall [Grove 70, Howard 81, Koch 82], and recognises that the controlling apparatus of hyphal tip growth must therefore be that which delivers the vesicles to the growth zone. The model proposes that vesicles are dispatched from a distribution centre, or *vesicle supply centre*, located behind the apex. Indeed, a prime candidate for the job of vesicle supply centre is the *Spitzenkörper*, due to its positioning in the hyphal tip and its evident involvement in the tip growth [Bartnicki-Garcia 95].

Amoeba model

[Heath 99] The amoeba model emphasises the importance of the cytoskeleton over the cell wall formation process. It has been observed that mutant specimens lacking a cell wall express some amoeboid behaviour, including the ability to form tendrils, or pseudopodia, and ‘crawl’ [Steinberg 93]. It is thus proposed that the cytoplasm of the hypha is an amoeba encased in a cell wall. The force propelling the tip forwards is thought to be the result of cytoskeletal forces.

There have been many attempts to quantify these ideas using mathematical approaches. These are reviewed extensively in [Gow 95] and some of the more recent mathematical studies are discussed in [Davidson 07].

Most of the models for fungal hyphal tip growth have an emphasis on the biomechanics at the cell wall and in its immediate vicinity. Although this has led to some very striking theoretical results (such as a mathematical model based on the vesicle supply centre idea which produces convincing replications of the exact shape of the hyphal tip [Bartnicki-Garcia 89]), some fundamental questions remain unanswered. Of foremost interest are questions concerning the role of long distance mass transport in the hypha. Does this affect the formation and maintenance of the Spitzenkörper? How is the velocity of the tip, and therefore the velocity of a so-called vesicle supply centre, affected by the supply of vesicles from distant parts of the hypha?

In [Regalado 97], a mathematical model is proposed to address some of these questions. Here the cytoplasm, vesicles and cytoskeleton within the hypha are modelled as a visco-elastic fluid. It is found that visco-elastic forces in the fluid can cause an increase in concentration of vesicles near the hyphal tip, suggesting a connection between the perceived interactions of vesicles with the cytoskeleton, and the formation of the Spitzenkörper. This work, however, assumes *a priori* a steady state of hyphal growth, and the tip velocity is not explicitly taken into account in the model.

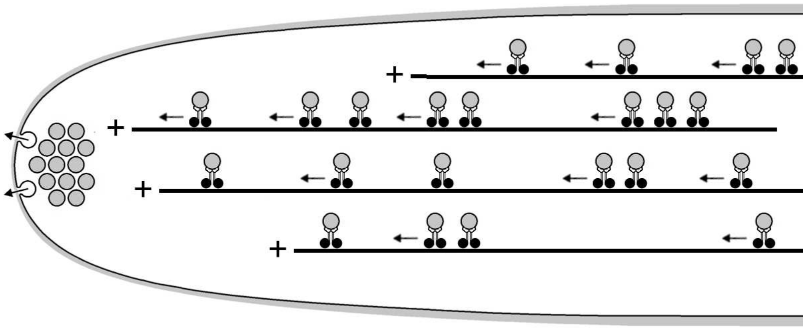

Figure 2.6: A simplified diagram of the process of polarised secretion resulting in tip growth in a fungal hypha. Secretory vesicles are transported by kinesin molecular motors (not to scale) along microtubules towards their growing "plus" ends. The vesicles accumulate within the so-called Spitzenkörper at the hyphal tip before fusing with the apical plasma membrane. The secretory vesicles deliver membrane proteins and lipids, cell wall synthesising enzymes and possibly cell wall precursors to the growing fungal tip. Hyphal widths typically vary between 5 and 15 μm.

We also wish to develop a model which makes a connection between the long distance transport of vesicles and some of the macroscopic properties of a growing fungal hypha. Our approach, however, is to draw from our experience of nonequilibrium driven diffusive systems (and particularly our knowledge of one-dimensional models such as the TASEP, reviewed above); and to study hyphal tip growth as a nonequilibrium transport problem. We shall make a direct connection between the supply of materials from distant parts of the hypha, their transport through the hypha and the resulting extension of the hypha as they reach the tip. Since we shall assume that mass reaching the hyphal tip is responsible for the extension of the hypha, our model is consistent with the vesicle supply centre model of [Bartnicki-Garcia 89]. We wish to address some simple physical questions about the particle distribution inside a growing hypha and its effect on the growth velocity.

2.2.3 The DEEP; a statistical physics model for hyphal growth

Our model is based on the picture of fungal growth illustrated in 2.6. Inside the hypha is an array of continuous microtubule tracks along which vesicles are transported to the site of growth. Once directly behind the tip, the vesicles fuse with the cell wall, resulting in the local elongation of the hypha. This is obviously a very simplified picture of the hypha infrastructure and growth dynamics, but it nonetheless serves to embody the fundamental growth mechanism in which we are interested: that of mass being driven towards a continuously advancing tip.

Note that in a real fungal hypha, rather than continuous microtubules running toward the tip, there is a complex mesh of microtubules (See Figure 2.5). The continuous microtubules that we envisage can be understood as a coarse-grained description, which simply describes the *average effect* of motor transport through the hypha.

In the spirit of the models outlined in section 2.1.5, we propose a simple, one dimensional lattice model with hopping particles and TASEP dynamics to describe the process of vesicle transport through the hypha. The vesicles are represented by the particles, while the microtubule is represented by the lattice. In this system however, the hypha and therefore the lattice itself, is extending as a direct result of the arrival of particles at its 'dynamic' end. Our model is thus coined the *dynamically extending exclusion process* or the DEEP. The whole hypha is envisaged as an array of such DEEPs.

As in the open boundary TASEP, particles are injected at one end and extracted at the other with rates α and β respectively; hopping along the intermediate lattice in a single direction only with rate 1. The DEEP however necessarily includes a further mechanism, by which the lattice can increase in size. The process of growth is incorporated into the model with the inclusion of a third parameter γ. This is the rate at which a particle reaching the final lattice site will act to extend the lattice, through a transformation: *particle* $\rightarrow$ *new site*. Biologically, γ represents the rate at which secretory vesicles fuse with the hyphal tip, α represents the vesicle density far from the tip and β allows vesicles to reach the tip without contributing directly to growth.

We justify our model with a simple order of magnitude test. We first identify the lattice repeat with the step size of a typical kinesin molecular motor: 8 nm [Bray 01]. In the model organism *N. crassa*, a 10 μm wide hypha growing at 25° C has as extension rate of ~ 0.5 μm per second. It has been estimated that ~ 600 vesicles per second must fuse with the tip to provide enough plasma membrane and other materials to maintain this hyphal extension rate [Collinge 74]. Thus, the extension of a hypha by one model lattice unit (~ 10 nm) is equivalent to the arrival of the order 10 vesicles. If each particle delivered to the end contributes to lattice extension ($\beta = 0$), we require ~ 10 equivalent effective microtubules in a typical hyphal cross section. This is acceptably within an order of magnitude of the number of microtubules observed near the Spitzenkoïper within the growing hyphal tip of *N. crassa* [Mouriño-Pérez 06].

The DEEP is clearly a highly idealised model, neglecting all of the complexities of the real biological interactions occurring inside the cytoplasm and at the cell wall. In particular, the model coarse-grains the trajectories of the motors, which as with most molecular motor transport processes, likely involve transfer between a number of microtubules before reaching the hyphal tip. What the model provides however, is a very simple framework within which we may address some physically relevant questions. For example, we may ask: Can a fixed supply of vesicles originating far from the tip support a steady state growth velocity? And if so, how does this velocity depend on the density far from the tip and the growth parameters at the tip?

In constructing the model, we also introduce a novel feature into the TASEP; that the system size is determined by the dynamics of its microscopic constituents. The study of this simple model thus contributes to our understanding of both "biological traffic" and non-equilibrium systems.

2.3 Microtubule dynamic instabilities

2.3.1 Introduction

The second biological problem we shall explore concerns the dynamics of microtubules. Microtubules are polymer filaments found within the cytoplasm of cells. They are hollow cylindrical structures, composed of bundled linear protofilaments. The protofilaments in turn consist of polymerised tubulin dimers. A microtubule is typically composed of between 10 and 15 protofilaments [Desai 97].

We have already encountered (in Subsection 2.1.5) one of the roles performed by microtubules inside cells: that of providing the tracks on which molecular motors can process during cellular transport processes. The functions of microtubules however go far beyond this single example. They are a part of the scaffolding of a cell, and provide structural support as well as in some cases motility, in the form of cilia or flagella. They are also involved in the positioning of chromosomes during mitosis. Importantly, the microtubules are capable of generating forces [Dogterom 05], which are exploited by the cell in many different ways.

In order to perform their various functions, microtubules are often highly dynamic structures, which undergo growth and decay through polymerisation and depolymerisation at either end. Large fluctuations in the length of a microtubule are known as *dynamic instabilities* and are characterised by prolonged periods of growth alongside periods of sudden drastic decay (‘catastrophe’), all on the timescale of seconds and minutes [Mitchison 84]. Among other functions, this particular characteristic has been identified as a vital component in the mechanism by which a cell is able to locate its centre prior to division [Howard 09].

2.3.2 Microtubule growth and decay

The growth of a microtubule is by the addition of GTP-tubulin. This is a protein dimer bound to a molecule of the energy carrier guanosine triphosphate (GTP). The tubulin dimers are incorporated into the linear protofilaments, which associate laterally to form the hollow cylindrically shaped microtubules. Some time after its incorporation into the microtubule, the GTP-tubulin is hydrolysed to form GDP-tubulin. The structure of GDP-tubulin protofilaments are such that their stable configuration is curved. While integrated into the microtubule, they are forced into a straight configuration, however, if the end of the microtubule becomes unstable, the GDP-tubulin protofilaments can be released, splaying out and causing a rapid shortening of the microtubule. (See Figure 2.7).

In [Cassimeris 88], real time observations were made of microtubule dynamics within living cells. Figure 2.8 shows a plot from this study, which shows the length of an individual microtubule measured over the course of several minutes. One can see random switching between periods of growth and decay. Within both phases the velocity is roughly constant and the velocity of decay is greater than the velocity of growth.

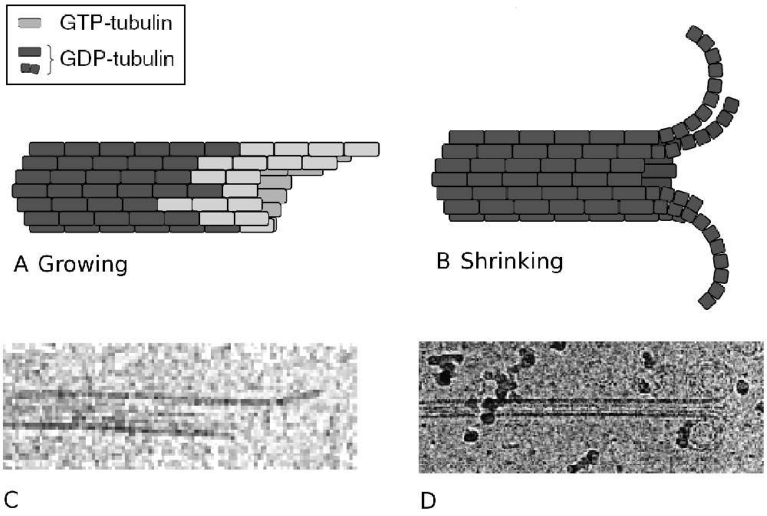

Figure 2.7: The tip of a microtubule in a growing (A) and shrinking (B) state. Microtubules grow by addition of GTP-tubulin subunits (red). Subunits are subsequently hydrolysed to become GDP-tubulin (green). In its unbound state, GDP-tubulin has a curved configuration. If released from the structure of the microtubule, it splays out, causing rapid shrinkage. (C,D) show cryo-electron micrograph images of microtubules in growing (C) and shrinking (D) states. (Image from [Burbank 06].)

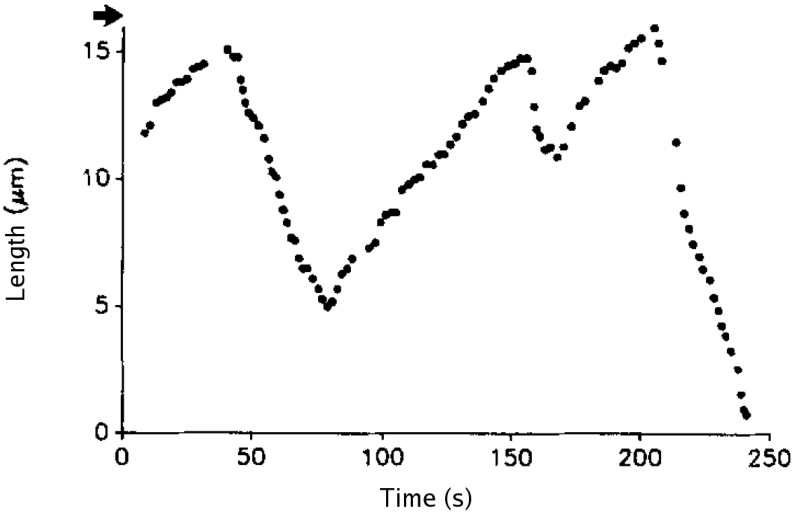

Figure 2.8: The assembly dynamics of an individual microtubule. The microtubule length is measured at ≈ 0.5s time intervals. Microtubules exist in phases of either elongation or rapid shortening, with each phase proceeding at relatively constant velocity. The transitions between phases are abrupt. (Image from [Cassimeris 88].)

2.3.3 The GTP-cap model

The first models for microtubule growth and decay were based on an assumption of equilibrium between the microtubule and the surrounding concentration of tubulin dimers. Extensive experimental work on the phenomenon however revealed that there is a more detailed structure to the process (see e.g. Figure 2.8) than a simple equilibrium exchange of dimers between the microtubule end and its environment. In 1984, the current model for explaining the growth and decay dynamics was proposed by Mitchison and Kirscher [Mitchison 84]. Their model is known as the GTP-cap model.

The essence of the GTP-cap model is that GTP-tubulin dimers at the end of the microtubule form a stabilising 'cap' that prevents the microtubule from shrinking. A microtubule with a GTP 'cap' is thus in a growing phase. Only in the event that the GTP cap is lost completely are the GDP-tubulin protofilaments exposed, and free to peel apart and depolymerise. When this happens, the microtubule switches from a growing to a rapidly shrinking phase. The relative rates of GTP-tubulin addition, hydrolysis from GTP→GDP, and GDP-tubulin degradation thus determine the dynamics of a microtubule. A GTP-cap is maintained when the rate of hydrolysation is less than the rate at which new GTP-tubulins are added. In high concentrations of tubulin, the rate of addition is high and the GTP-cap will only be lost through very rare fluctuations. However, as the tubulin concentration decreases, the average size of the GTP-cap decreases and the chance of a cap loss become larger. Once in the shrinking phase, the microtubule will continue to depolymerise until it is degraded entirely, or until a new GTP-cap forms and regrowth begins. The latter is a rare event, termed 'rescue'.

2.3.4 A microscopic study of the GTP-cap model

In [Antal 07a] an idealised realisation of the GTP-cap model, first introduced in [Zong 06], is studied. This model makes an explicit connection between the dynamics of the microscopic constituents of a microtubule (i.e. the GTP and GDP tubulin subunits), and their effect on the macroscopic microtubule growth and decay dynamics. The model is constructed very simply from the assumptions of the GTP-cap model. A microtubule is represented as a one dimensional array of GTP and GDP monomers. The microtubule polymerises from one end through the addition of GTP monomers, which form the stabilising GTP-cap. While GTP remains at the end of a microtubule, there can be no depolymersation. GTP decays to GDP at the fixed rate of hydrolysis. If the microtubule tip decays to GDP, then depolymerisation can occur.

Note that this simplistic model treats the growth of a microtubule as a single polymerisation event, whereas in reality the growth by one unit of length involves the polymerisation of up to 15 GTP-tubulin subunits, depending on how many protofilaments compose the microtubule, as illustrated in Figure 2.7. This minimalistic model is not supposed to capture any of the (still not well understood) detail of the polymerisation process at the tip, but rather to allow us to study general dynamic properties of growth and decay in a statistical sense.

The dynamics of the model are controlled by 3 parameters; the rate of polymerisation of GTP at the tip (λ), the rate of depolymerisation of GDP from the tip (μ), and the rate of hydrolysis, which causes the decay from GTP→GDP (1). An additional parameter p can be included, which alters the rate of growth should the last monomer be GDP i.e. the rate of growth in this case is $p\lambda$. Denoting GTP $+$, GDP $-$, GTP/GDP $\cdot$ and the dynamic microtubule end $\rangle$, the microtubule thus evolves according to the following transitions:

$$|\cdot\cdot{+}\rangle \quad \rightarrow \quad |\cdot\cdot + +\rangle \tag{2.9}$$

$$|\cdot\cdot{-}\rangle \quad \rightarrow \quad |\cdot\cdot - +\rangle \tag{2.10}$$

$$|\cdot\cdot + \cdot\cdot\rangle \quad \rightarrow \quad |\cdot\cdot - \cdot\,\cdot\rangle \tag{2.11}$$

$$|\cdot\cdot\cdot\cdot{-}\rangle \quad \rightarrow \quad |\cdot\cdot\cdot\cdot\rangle \tag{2.12}$$

where (2.9) occurs with rate λ, (2.10) occurs with rate $p\lambda$, (2.11) occurs with rate 1 and (2.12) occurs with rate μ.

The behaviour resulting from these simple dynamics is a rich interplay between growth and decay events which can lead to drastic fluctuations in the length of the microtubule. Depending on the parameters, a microtubule's length can grow indefinitely, or remain finite in the long time limit and a phase transition between these two regimes is proposed.

2.3.5 Analysis of the idealised GTP-cap model

Due to the simplicity of the idealised GTP-cap model, significant analytic progress was possible [Antal 07b], including the derivation of many statistical properties of the system, such as the exact microtubule and GTP-cap length distributions, and distributions for the length of the GTP and GDP islands found within the bulk of the microtubule. A scaling law was also found for the time between catastrophes, where the microtubule length shrinks to zero. And a phase transition was proposed to exist between parameter regions where the microtubule is growing unbounded and where it remains of finite size.

We are interested in whether one can map the GTP-cap model onto a dynamic lattice model such as the one introduced in Subsection 2.2.3, and study the growth and decay dynamics using a mean-field analysis, such as that which has been successful in treating the TASEP (Subsection 2.1.1). In particular we would like use this approach to see if one can find an analytical expression for the phase transition, for *general* parameter values. This is in contrast to the work of [Antal 07b], where a phase transition was approximated by piecing together the behaviour of the system for different extremes of the parameter values, such as for zero and infinite decay rates.

Chapter 3

The dynamically extending exclusion process

3.1 Introduction

We now move on to the central theme of the thesis: the development and analysis of the dynamically extending exclusion process, introduced in Chapter 2 as a model for fungal hyphal growth. Our aim is to ascertain, with the aid of mean-field treatments and Monte Carlo simulation, the dynamic behaviour of this simple one-dimensional system; and to characterise the structure of its phase diagram with respect to the three parameter phase-space of the model. We shall also discuss the model in relation to other exclusion processes and ultimately how it might fare against observation in fungal biology.

The chapter is organised as follows. I begin by defining the model precisely. This is made rigorous with a set of exact equations defining the dynamics of the system. The moving boundary conditions are discussed as a point of particular interest in this model. I shall then begin the analysis with a simple mean-field approximation. This is the first port of call and gives us a prediction of the sort of steady states that our system can support. However, as with all mean-field theories, we do not expect that this basic analysis is quantitatively precise. I shall then show that with a straightforward refinement of the simple mean-field theory, one obtains results which are in very good agreement with Monte Carlo simulations. I show that interestingly, a logical progression of our refined mean-field approximation to a 'further refined theory' does not improve on the results of the previous approximation. A heuristic argument for the DEEP phase structure is also given, with some remarks on the relation of this model to another of the exclusion processes discussed in Section 2.1.5; I conclude the chapter with a summary of results and some comments on the suitability of the DEEP in the context from which it was born.

3.1.1 The model

The dynamically extending exclusion process (DEEP) is defined on a one-dimensional lattice. Particles progress stochastically along the lattice according to a set of dynamic rules. These rules are expressed in terms of the *rates* at which the following processes occur: particles in the bulk hop to the left with rate 1; particles enter the lattice from the right with rate α; and at site 1 two processes may occur: particles detach from site 1

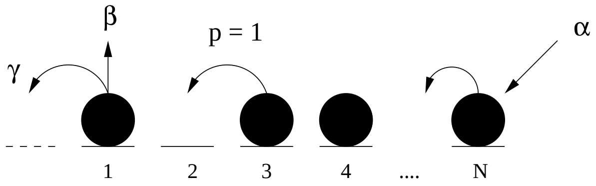

Figure 3.1: The dynamically extending exclusion process. Particles enter the lattice at the right with rate α, progress to the left in single hops of rate 1, leave the left-most site with rate β and transform into a new lattice site with rate γ. The left-most site is defined as site 1.

with rate β and particles may transform into a new lattice site with rate γ. The model is illustrated schematically in Figure 3.1. Thus γ is the parameter controlling the lattice growth, β allows particles to leave the end of the lattice without extending it and ratio γ/β controls the efficiency with which the lattice extends.

Indicating the presence of a particle by 1 and an empty lattice site by 0 the stochastic dynamics is

$$01 \rightarrow 10 \quad \text{with rate} \quad 1\,, \tag{3.1}$$

$$\text{at site 1} \quad 1 \rightarrow 0 \quad \text{with rate} \quad \beta \tag{3.2}$$

$$\text{at site 1} \quad 1 \rightarrow 00 \quad \text{with rate} \quad \gamma\,, \tag{3.3}$$

$$\text{at the rightmost site} \quad 0 \rightarrow 1 \quad \text{with rate} \quad \alpha\,. \tag{3.4}$$

Note that the leftward direction of particle hopping is chosen for reasons which will soon become apparent.

This stochastic model may be realised with random sequential dynamics. This means that in a time interval Δt, on average each site attempts one probabilistic update, though the order in which the updates are attempted are random. The random sequential dynamics allows that in some instances a site will attempt more than one update while in others it will attempt none, however when averaged over a large ensemble or a large time interval, the rates at which the updates occur correctly converge to those stipulated by the model. To demonstrate this process, a realisation of the model dynamics for a system of initial size $N = 10$ is illustrated in Figures 3.2 and 3.3. In Figure 3.2, the dynamics during a single time interval is plotted. Each transition is shown in the order in which they occur within one Δt. Figure 3.3 shows the configuration of the same lattice at each time interval between $t = \Delta t$ and $t = 500\Delta t$. During this time the lattice grows from $N = 12$ to $N = 94$. We shall see in Section 3.2 how the growth velocity can be accurately predicted using a simple mean-field theory.

3.1.2 Exact correlation equations

Following the prescription outlined in Chapter 2, Section 2.1.2, we now construct some exact correlation equations for the model dynamics. Since the lattice is not static, we must

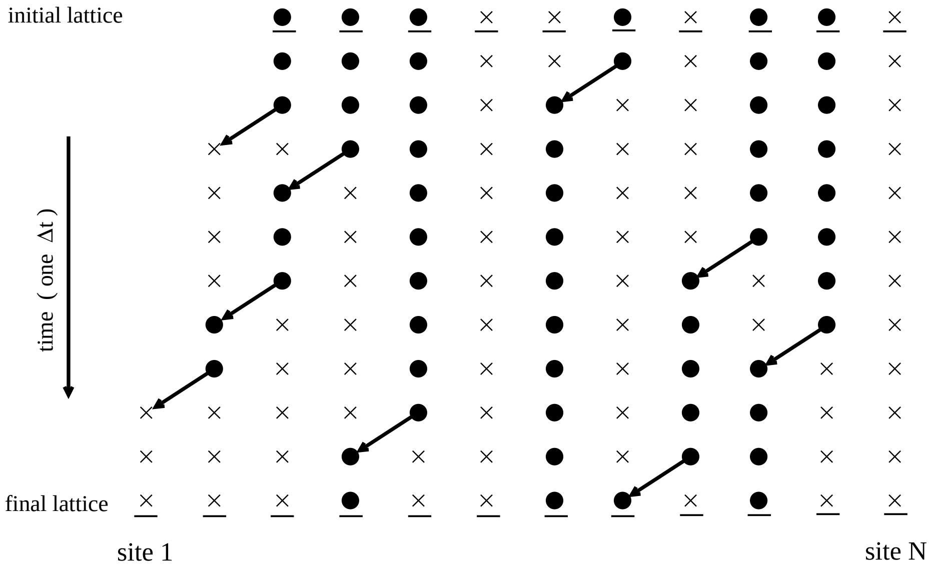

Figure 3.2: The evolution of the DEEP during a single time interval. The initial lattice configuration (top) comprising particles (black circles) and vacant sites (x) evolves stochastically to the final lattice (bottom). The parameters used in this realisation are $\alpha = 0.4$, $\beta = 0.1$, $\gamma = 0.8$. During this particular time interval all of the particles perform at least one hop to the left, two growth events occur, no particles enter and no particles leave without contributing to the growth.

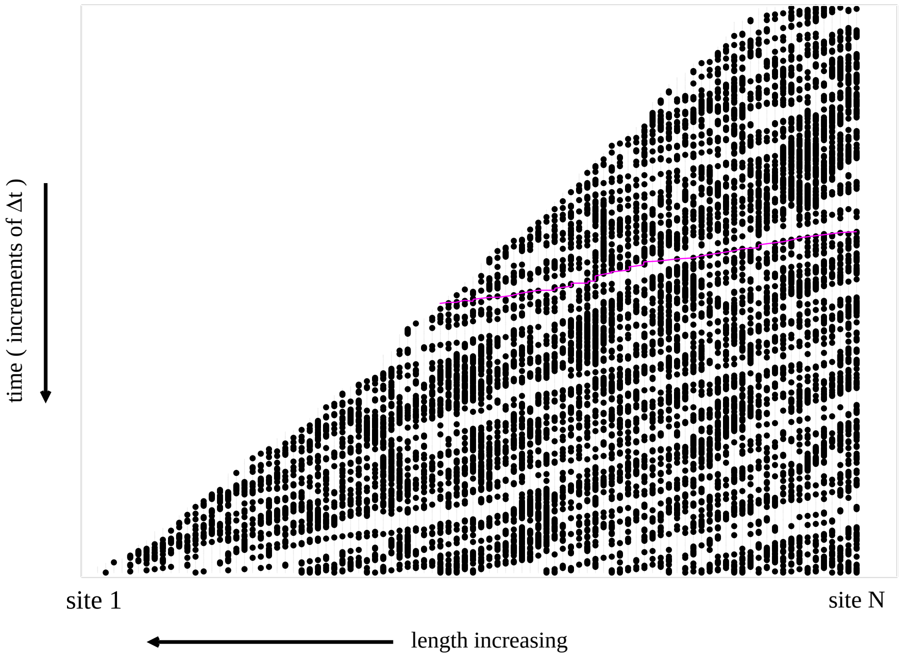

Figure 3.3: The DEEP particle dynamics during 500Δt, with parameters $\alpha = 0.4$, $\beta = 0.1$, $\gamma = 0.8$. Each horizontal array of particles (black circles) and vacant sites (grey dots) represents the lattice at the end of a time increment Δt. The initial lattice (top) grows from $N = 12$ to a final length of $N = 94$ (bottom). The trajectory of a particle added at $t \approx 200\Delta t$ is indicated (magenta line). The particle traverses the lattice, and contributes to the growth.

choose a reference frame in which to do this. Our choice is to consider the reference frame of the tip. In this way we explicitly take into account the special dynamics occurring at the site of growth. The leftmost site is thus identified with the tip and always labelled as site 1.

Consider now the change in the average occupancy of a given site, with time. We denote the occupancy at site i, τ_i, which can take on a value 1 or 0. Using angle brackets to denote a statistical average, we have for site 1 the following correlation equation:

$$\frac{d\langle\tau_1\rangle}{dt} = \langle[1-\tau_1]\tau_2\rangle - (\gamma+\beta)\langle\tau_1\rangle \tag{3.5}$$

The first term is the average flow of particles into site 1 given it was initially empty and site 2 was occupied. The second term describes the loss of particles out of site 1 given it was initially occupied, due to lattice growth with rate γ and particle disassociation from the lattice with rate β.

For site 2, we have the following equation:

$$\frac{d\langle\tau_2\rangle}{dt} = \langle[1-\tau_2]\tau_3\rangle - \langle[1-\tau_1]\tau_2\rangle - \gamma\langle\tau_1\tau_2\rangle \ , \tag{3.6}$$

Here, the first term is the flow in as described above. The second term is flow out due to particles hopping from site 2 into an unoccupied site 1. The third term describes a loss of particles from site 2 due to the growth of the lattice. This is an effect of the reference frame: when a growth event occurs (3.3), it is necessary to relabel all sites $i \rightarrow i+1$ so that the new lattice site is labelled site 1. A particle from site 2 is thus now found in site 3.

For sites $i \geq 3$, all the equations have the same form:

$$\frac{d\langle\tau_i\rangle}{dt} = \langle[1-\tau_i]\tau_{i+1}\rangle - \langle[1-\tau_{i-1}]\tau_i\rangle + \gamma\langle\tau_1[\tau_{i-1}-\tau_i]\rangle \quad i \geq 3 \ . \tag{3.7}$$

Again, the final term describes the transfer of particles to the right due to site relabelling. Here in the bulk of the system a particle may be gained from site $i-1$, or lost from site i when the labels are updated.

3.1.3 Boundary conditions

In the DEEP, the system size continually increases, therefore special care must be taken when considering the conditions at the lattice boundaries. As we shall be solving with respect to a stationary tip, it is the far boundary that will be receding as the lattice grows. We may consider the far boundary to be connected to a reservoir of density α from which particles enter the lattice. As time $t \rightarrow \infty$ the system size $N(t) \rightarrow \infty$, therefore we may write a boundary condition far from the tip:

$$\alpha = \lim_{N\rightarrow\infty} \langle\tau_N\rangle \ . \tag{3.8}$$

The boundary condition at site 1 is simply controlled by the growth rate and the tip velocity:

$$v = \gamma\langle\tau_1\rangle\ . \tag{3.9}$$

3.1.4 Steady state

The steady state is defined as the state in which the statistical average of the occupancy at each site i is stationary in time.

$$\frac{d\langle\tau_i\rangle}{dt} = 0$$

This means that the flow of particles through the system is equal everywhere. In our growing system a steady state is categorised by the stationary values of $\langle\tau_i\rangle$. Steady states with different macroscopic properties, such as tip velocity and bulk density are said to be in different *phases*.

3.1.5 Particle current

Equations 3.5–3.7 may be understood in terms of the particle flow through the system, or particle *current*, J. One may separate the terms into those representing the current of particles crossing between sites $i-1$ and i, and those representing the current crossing between sites i and $i+1$ (see Figure 3.4). Since in the steady state, the particle flow is equal everywhere, we obtain the following system of exact equations for J.

$$J_{1,tip} = J = (\gamma+\beta)\langle\tau_1\rangle\ , \tag{3.10}$$

$$J_{2,1} = J = \langle\tau_2[1-\tau_1]\rangle\ , \tag{3.11}$$

$$J_{i+1,i} = J = \langle\tau_{i+1}[1-\tau_i]\rangle - \gamma\langle\tau_1\tau_i\rangle \quad i \geq 2\ . \tag{3.12}$$

The rate of lattice extension, or tip velocity, was given by Equation 3.9:

$$v = \gamma\langle\tau_1\rangle\ ,$$

which leads us to a relation between the current and velocity:

$$J = v(1+\frac{\beta}{\gamma}). \tag{3.13}$$

Our approach will be to solve this system of equations (3.10–3.12) in the steady state.

3.2 Simple mean-field theory

We now begin our analysis of the exact correlation equations, starting with the simplest mean-field prescription described in Section 2.1.2. We make the replacement:

$$\langle\tau_i\tau_j\rangle = \langle\tau_i\rangle\langle\tau_j\rangle \qquad \forall i,j\ (i \neq j)\ , \tag{3.14}$$

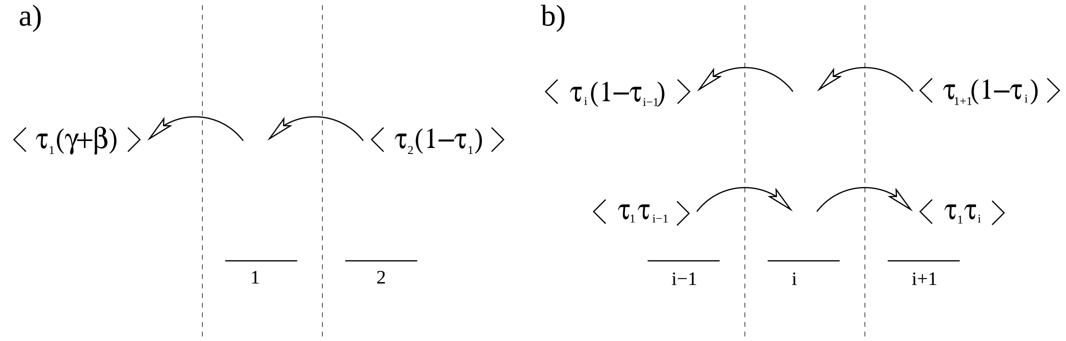

Figure 3.4: One can understand the terms of (3.5–3.7) as currents crossing the boundaries between sites. a) The particle flow into and out of site 1. b) The particle flow into and out of site i, in the bulk. Since the current is a constant, J, everywhere in the steady state, we obtain three unique expressions for J.

thus ignoring *all* correlations between the occupancies at different sites. We define a 'density' ρ_i to denote the uncorrelated average occupancy at site i, so that

$$\langle\tau_i\rangle\langle\tau_j\rangle = \rho_i\rho_j \ . \tag{3.15}$$

Equation 3.12 then gives the recurrence relation:

$$\rho_{i+1} = \frac{J + v\rho_i}{1-\rho_i} \quad i \geq 2 \ . \tag{3.16}$$

We find ρ_1, ρ_2 from (3.10), (3.11) and (3.13):

$$\rho_1 = \frac{J}{\gamma+\beta} \tag{3.17}$$

$$\rho_2 = \frac{J}{1-\rho_1} = \frac{J(\gamma+\beta)}{\gamma+\beta-J} \ . \tag{3.18}$$

The recurrence (3.16) together with the initial condition (3.18) determine all ρ_i in terms of J (or v). It remains to fix J self-consistently to determine the various phases.

3.2.1 Low density phase

The recurrence (3.16) has two fixed points

$$\rho_\pm = \frac{1-v \pm \sqrt{(1-v)^2-4J}}{2} \ . \tag{3.19}$$

The lower of the fixed points is stable, so for ρ_2 within the basin of attraction, the density iterates to this value and the density profile converges rapidly to a constant density in the bulk of the lattice. See Figure 3.5 for a graphical representation of the iterative solutions to (3.16). To meet boundary condition (3.8), we define the lower fixed point:

$$\rho_- = \alpha \ . \tag{3.20}$$

It follows from (3.19) that the upper fixed point is then:

$$\rho_+ = 1 - v - \alpha \ . \tag{3.21}$$

The boundary condition (3.8) fixes v using (3.13) and (3.16):

$$v_{ld} = \frac{\alpha(1-\alpha)}{1 + \alpha + \frac{\beta}{\gamma}} \ , \tag{3.22}$$

and the corresponding current is $J_{ld} = (1 + \beta/\gamma)v_{ld}$.

The condition for this phase is that $\rho_2 < \rho_+$ so that $\rho_i \to \rho_-$ as $i \to \infty$. Using (3.21) and (3.22) this condition reduces to

$$\gamma > \frac{\alpha - \beta}{1 + \alpha} \ . \tag{3.23}$$

This relation defines the phase boundary for the low density phase.

The density in the bulk of the low density phase is limited by a low input rate α. At the tip there is a decay to the boundary condition (3.20) determined by rates β and γ. The low density region is split into two subregions distinguished by whether the tip density is above or below α. For $\rho_2 < \alpha$, the tip density is less than α and for $\alpha < \rho_2 < 1 - v - \alpha$, the tip density is greater than α.

3.2.2 High density phase

Another possible solution to (3.16) and (3.8) is that $\rho_2 = \rho_+$. In this case the recurrence (3.16) yields $\rho_i = \rho_+$ for $i \geq 2$. The phenomenological interpretation is that when $(\gamma + \beta)$, the rate of release of particles at the growing end, is no longer large enough to control the input rate; the particle density near the tip reaches a maximum value ρ_+ that extends back through the lattice. The high density in the bulk ρ_+ is then connected to the density at the input boundary α, with a discontinuous *shock*. Mass conservation (see Section 2.1.3) implies a speed for the shock v_s, given by:

$$v_s = 1 - \rho_+ - \alpha \ . \tag{3.24}$$

The shock solution is illustrated schematically in Figure 3.6.

Defining $\rho_2 = \rho_+$, we obtain from (3.13), (3.18) and (3.19), the tip velocity in this phase:

$$v_{hd} = \frac{\gamma(1 - 2\gamma - \beta)}{1 - \gamma} \ , \tag{3.25}$$

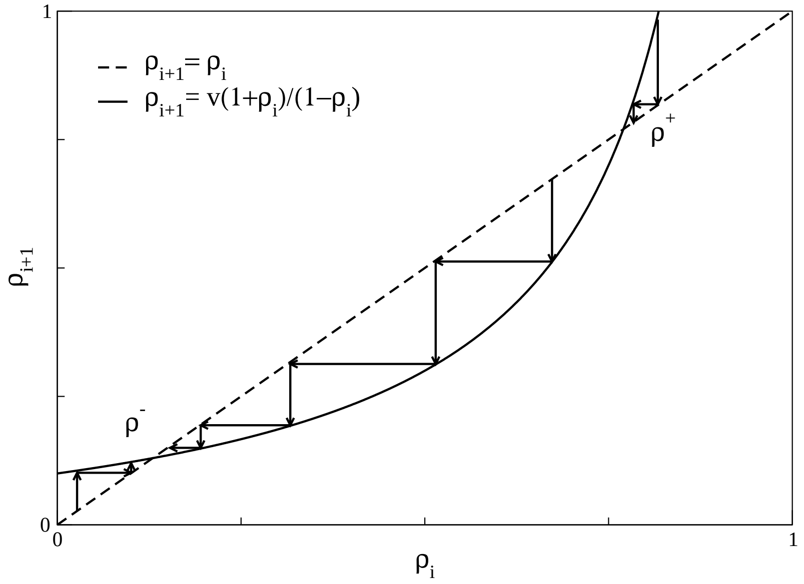

Figure 3.5: A graphical representation of the solutions to the recurrence relation (3.16). Iterations beginning below the unstable upper fixed point, ρ_+, converge to the stable lower fixed point, ρ_-.

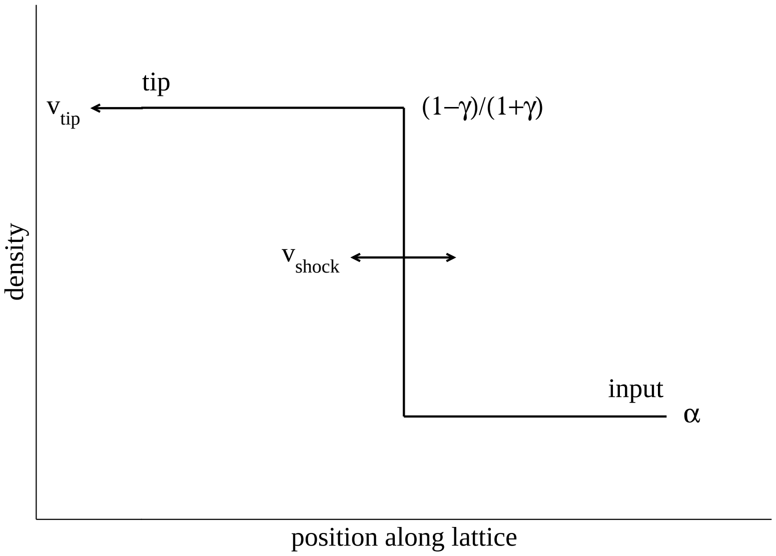

Figure 3.6: A shock is set up between regions in the lattice with a high density (next to the tip) and low density (far from the tip). The shock travels with a velocity fixed through mass conservation, which may be different to the velocity of the lattice tip.

and from this and (3.21), we have an expression for the density at site 2 and throughout the rest of the high density region:

$$\rho_+ = 1 - 2\gamma - \beta \ . \tag{3.26}$$

From (3.23), one can see that this phase is entered when:

$$\gamma = (\alpha - \beta)/(1+\alpha) \ . \tag{3.27}$$

Due to the high density structure in the tip region we refer to the phase as the *'jammed'* or *high density phase.* Note, however, that only on the phase boundary where $v_s = v$, is the shock, and therefore the density profile, stationary in the reference frame of the tip. In the rest of this phase $v_s < v$, and the shock moves away from the tip, resulting in an expanding high density region. Provided $v_s > 0$, the shock will also be moving away from the right boundary and the expanding high density region will never occupy the whole system. Using conditions (3.19) and (3.24), the condition $v_s > 0$ becomes:

$$\frac{\alpha - \beta}{1+\alpha} > \gamma > \frac{\alpha - \beta}{2} \ . \tag{3.28}$$

In order to fulfil our criterion for a steady state (stationary densities in our frame of reference as $t \to \infty$) we should be in the reference frame of the shock. Then the density in front of the shock is given by $1 - 2\gamma - \beta$ and the density behind is given by α.

On the other hand if $v_s < 0$, then the shock moves backwards through the system until it reaches the right boundary. In this region a high density is maintained throughout the length of the lattice except for a boundary region next to the right boundary. The system may be considered to be in a high density steady state with the reference frame being the stationary frame where the right hand boundary is fixed. The condition $v_s < 0$ becomes

$$\gamma < \frac{\alpha - \beta}{2} \ . \tag{3.29}$$

3.2.3 Maximal current phase

Both the high and low density phases are bounded by the condition that the roots $\rho_\pm$ of (3.16) are real. Clearly, the roots (3.19) are real provided $(1-v)^2 > 4J$, which implies using (3.13), that $v < v_{max}$, where the maximum velocity satisfies

$$v_{max} \quad = \quad \frac{2\beta + 3\gamma - 2\sqrt{\beta^2 + 3\gamma\beta + 2\gamma^2}}{\gamma} \ , \tag{3.30}$$

and the corresponding maximum current is $J_{max} = (1 + \beta/\gamma)v_{max}$.

When $J = J_{max}$, we have a single root of (3.16) and from (3.19) we deduce that the bulk density is

$$\rho_{max} = \frac{1 - v_{max}}{2} \; . \tag{3.31}$$

We refer to this phase as the maximal current phase; the flow is no longer controlled by the boundary condition α, rather it has saturated at a maximal flow rate, J_{max}. Note that $\rho_{max} < 1/2$ and $J_{max} < 1/4$.

On a finite system of size N, in order to fix the boundary conditions, one takes $J = J_{max} + O(1/N^2)$ [Derrida 92, Blythe 07]. The iterative solution of (3.16) then yields a density profile decaying smoothly between both boundaries with an algebraic rather than an exponential decay of the density from the boundaries. Note that there is thus no natural reference frame in which we may define a steady state. Rather, the density at each site evolves as the system grows and we characterise this phase as quasi-stationary. We find the phase boundaries by considering the transitions to the maximal current phase from the low density phase, and from the high density phase: $J_{ld} = J_{max}$ when

$$\gamma = \frac{\beta - 2\alpha\beta}{\alpha^2 - 1 + 2\alpha} \; , \tag{3.32}$$

and $J_{hd} = J_{max}$ when

$$\beta = \frac{4\gamma - 2\gamma^2 - 1}{\gamma - 2} \; . \tag{3.33}$$

3D Phase diagram: In order to visualise the phase structure of the DEEP, we may construct a 3-dimensional phase diagram from the results of the simple mean-field theory. Figure 3.7 is a schematic representation of the three phase regions, joined by the phase boundary surfaces described above. On the diagram, one can see that in the limit of no growth ($\gamma = 0$), the phase boundaries reduce to those of the TASEP (see Figure 2.1.1).

3.2.4 Mean-field density profiles

The mean-field density profiles across the lattice during the various phases described above can be computed numerically, using Equations 3.5–3.61. We take the simple mean-field approximation (3.14–3.15), and express (3.5–3.61) as discrete update equations:

$$\rho_1(t+\Delta t) = \rho_1(t) + \Delta t[\rho_2(t)(1-\rho_1) - \rho_1(t)(\gamma+\beta)] \tag{3.34}$$

$$\rho_2(t+\Delta t) = \rho_2(t) + \Delta t[\rho_3(t)(1-\rho_3) - \rho_3(t)(1-\rho_2(t)) - \gamma\rho_1(t)\rho_2(t)] \tag{3.35}$$

$$\rho_i(t+\Delta t) = \rho_i(t) + \Delta t[\rho_{i+1}(t)(1-\rho_i) - \rho_i(t)(1-\rho_{i-1}(t)) - \gamma\rho_1(t)(\rho_{i-1}(t) - \rho_i(t))] \tag{3.36}$$

We may use these equations to update an array of double values representing the particle density at each lattice site. We choose a parallel update scheme whereby a new lattice of values $\rho_i(t + \Delta t)$ is constructed from the ρ_i of the original lattice using Equations 3.34–3.36. Once computed, the original lattice is discarded and the process is repeated. After enough repeats (e.g < 100000 for a system size of 300 and $\Delta t = 0.1$), the ρ_i converge

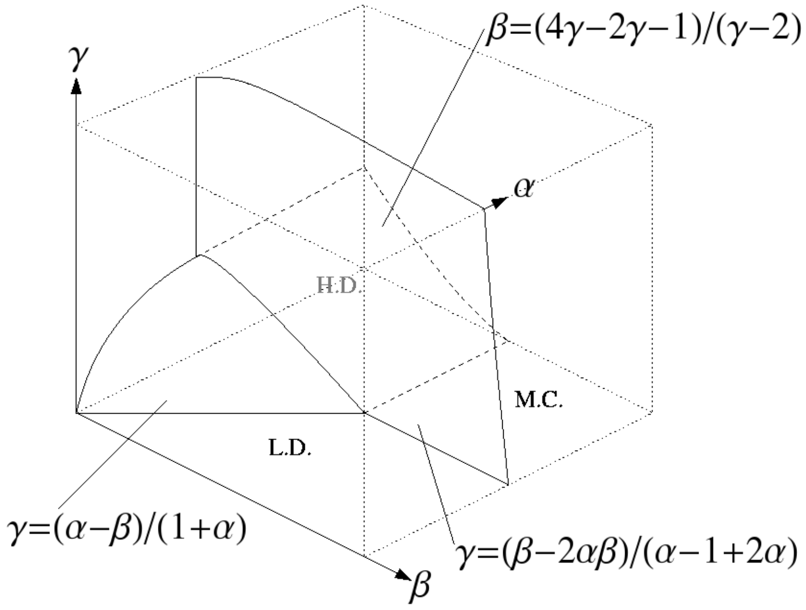

Figure 3.7: A schematic representation of the phase diagram in 3-D α, β, γ parameter space for the simple mean-field approximation. Three phases are shown (without subregions). The $\gamma = 0$ plane corresponds to the well known TASEP phase diagram.

to a stationary state. Note that we are solving (3.5–3.61) for a fixed number of sites, in the stationary frame of the tip. This requires enforcing a boundary condition at site N, which in reality would be receding as the lattice grows. One can verify whether the density profiles are affected by this artificial boundary by comparing profiles generated using lattices of different sizes.

Figures 3.8–3.12 give a representative illustration of the behaviour predicted by the simple mean-field theory. Figure 3.8 shows the 2D phase diagram in α–γ phase space, for $\beta = 0.1$. Marked on the phase diagram are a selection of points sampling the different phases. Density profiles corresponding to these parameter values are shown in Figures 3.9–3.11. The low density profiles converge rapidly to α. The high density profiles are constant after lattice site 2, while in the shock region the high density at the tip is separated from the low density far from the tip by a travelling shock. The maximal current phase is characterised by a decay at both ends of the lattice. As noted in the previous section, this is only a quasi-stationary state and the density profiles are thus dependent on the lattice size.

By plotting the density profile at successive time intervals, one can also visualise the evolution of the densities as they relax to a steady state. Figure 3.12 shows density profiles from each of the phases, evolving from an initial random configuration of densities, towards a steady state at intervals of $2000\Delta t$. One can see the formation of shocks in the system. In the case of the high and low density phases, the shock propagates to the boundary. In the shock phase it localises in the bulk of the system. The Maximal current phase does

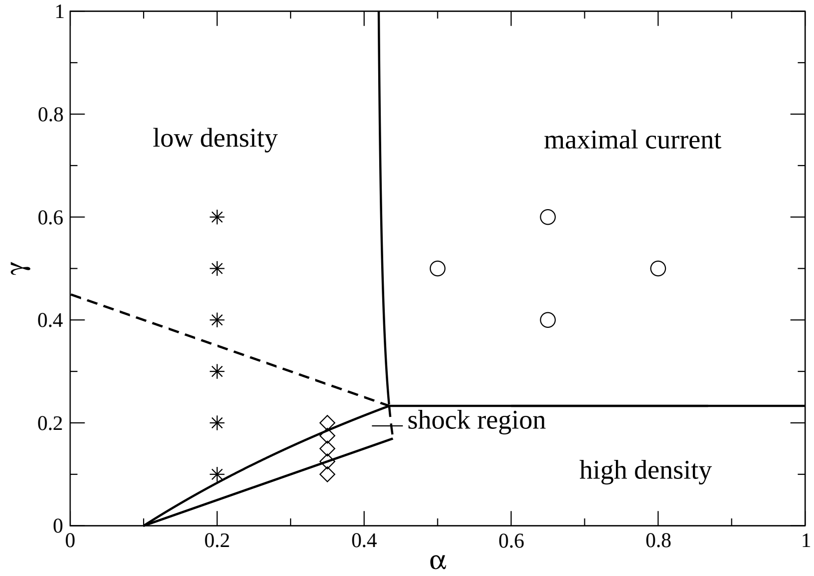

Figure 3.8: The 2D phase diagram for $\beta = 0.1$. The symbols indicate the sets of points for which density profiles are computed in Figures 3.9 (stars), 3.10 (diamonds) and 3.11 (circles).

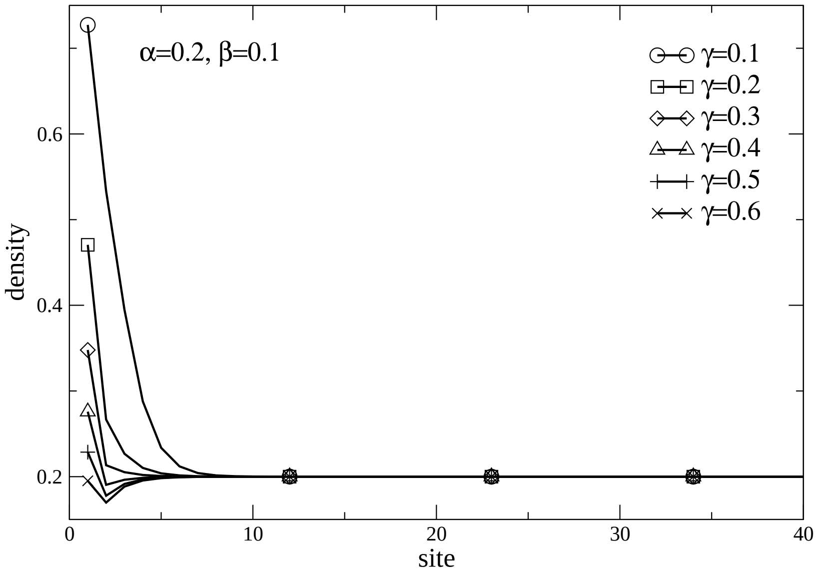

Figure 3.9: Profiles in the low density region of the phase diagram. The density converges rapidly to the input α. For $\gamma < \alpha(1-\alpha-\beta)/2\alpha$ the profiles decay from above α while for $\gamma > \alpha(1-\alpha-\beta)/2\alpha$ they decay from below.

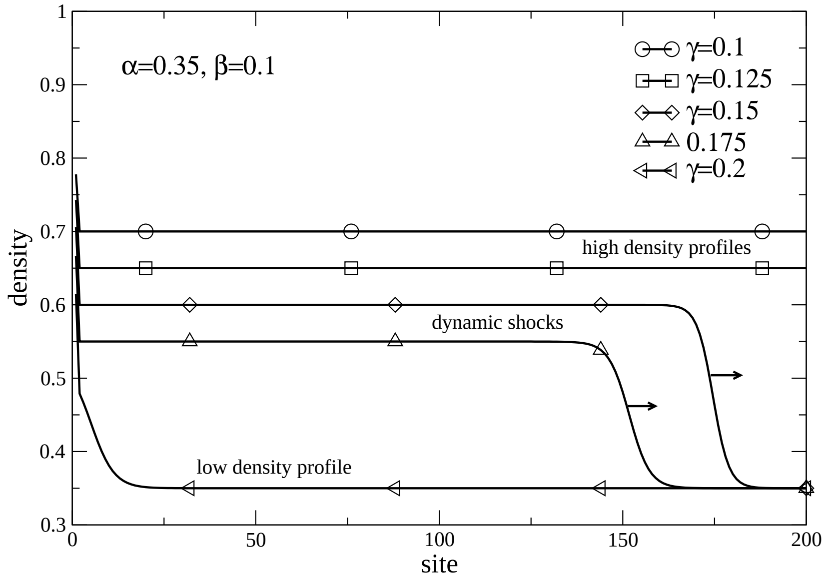

Figure 3.10: A sample of density profiles spanning the shock and high density region of the phase diagram. In the high density region the density profiles are flat with $\rho_{bulk} = 1 - 2\gamma - \beta$. In this reference frame, dynamic shocks in the shock region are travelling to the right. A low density profile immediately beyond the phase boundary is also shown.

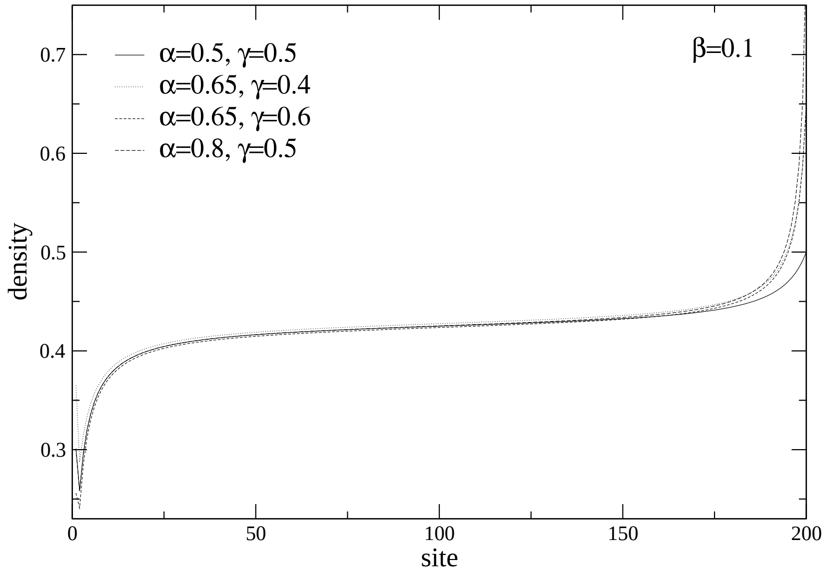

Figure 3.11: The maximal current profiles of four sample parameter points are shown. In this phase the dynamics are limited by the bulk hopping rate, thus profiles overlap except at the boundaries. These are only quasi-stationary states, as the density decays from both boundaries which are recede from each other.

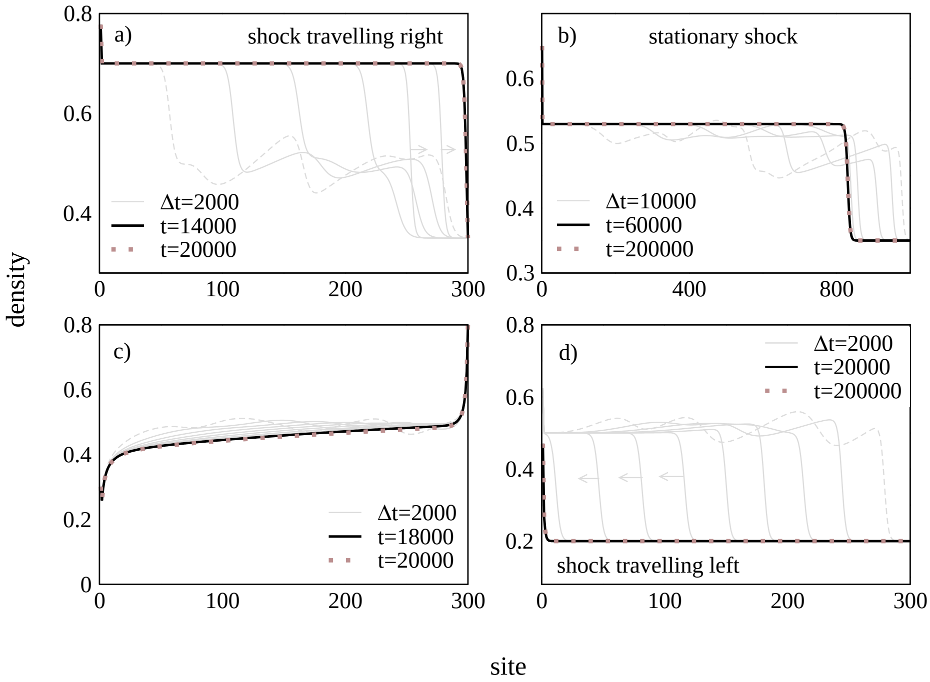

Figure 3.12: The time evolution of densities for representative parameter values from each part of the $\beta = 0.1$ phase diagram. The grey lines indicate initial (dashed) and intermediate (solid) profiles at time intervals given. The black and brown lines indicate the relaxed profiles. (a) $\alpha = 0.35$, $\gamma = 0.1$: A high density profile is formed due to the shock propagating all the way to the right boundary. (b) $\alpha = 0.35$, $\gamma = 0.185$: The phase boundary between high and low density phases. Here the shock localises to a position in the bulk. (c) $\alpha = 0.8$, $\gamma = 0.5$: The maximal current profile with no shock formation. (d) $\alpha = 0.2$, $\gamma = 0.2$: A low density phase formed as the shock propagates all the way to the left boundary.

not form shocks.

It should be noted that the rich phase behaviour of the DEEP arises primarily from the exclusion dynamics of the particles. The property that no more than one particle can occupy a single site causes the particles to ‘jam’ when the density becomes high. The system has a characteristic high (jammed) density, which corresponds to the upper fixed root of the recursion (3.16). If one was to remove the exclusion reaction from the DEEP, then the solution structure becomes somewhat less interesting. By removing all $(1-\rho_i)$ factors from the correlation equations (3.5–3.7), one can deduce that the recursion relation is just a linear function:

$$\rho_{i+1} = v(1+\rho_i) \tag{3.37}$$

For $v < 1$, this relation has only one fixed point, which must correspond to α. One type of steady state solution is permitted, corresponding to a power law convergence of (3.37) from below α, to α.

3.2.5 The case $\beta = 0$

We may greatly simplify the equations of the DEEP, by considering the case $\beta = 0$. This is the limit of no extraction from the tip and every particle reaching site 1 now contributes to the lattice growth. The current and velocity are therefore equal ($J = v$). We now have in the steady state:

$$\rho_1 = v/\gamma \qquad \rho_2 = \gamma v/(\gamma - v) \tag{3.38}$$

$$\rho_{i+1} = \frac{v(1+\rho_i)}{1-\rho_i} \quad i \geq 2\ . \tag{3.39}$$

The condition for the low density phase (3.23) reduces to $\gamma > \alpha/(1+\alpha)$ and the tip velocity is given by

$$v = J = \frac{\alpha(1-\alpha)}{(1+\alpha)}\ . \tag{3.40}$$

Then, the condition that $\rho_\pm$ be real becomes

$$J = v < 3 - 2\sqrt{2}\ , \tag{3.41}$$

which, with (3.40), implies

$$\alpha < \sqrt{2} - 1\ . \tag{3.42}$$

In the high density phase, where $\gamma < \alpha/(1+\alpha)$, the tip velocity (3.25) is

$$v = J = \frac{\gamma(1-2\gamma)}{1-\gamma}\ . \tag{3.43}$$

For $\alpha/2 < \gamma < \alpha/(1+\alpha)$ a dynamic shock exists in the system.

In the high density phase condition (3.41) together with (3.43) imply

$$\gamma < 1 - \frac{1}{\sqrt{2}}\ . \tag{3.44}$$

Therefore for the region bounded by $\alpha > \sqrt{2} - 1$, $\gamma > 1 - 1/\sqrt{2}$, the system is in the maximal current phase, where the bulk density is $\rho_{max} = \sqrt{2} - 1$ and the current is $J_{max} = 3 - 2\sqrt{2}$.

3.2.6 Summary

With the basic mean-field scheme of replacing all correlation functions with uncorrelated densities ($\langle \tau_i \tau_j \rangle = \rho_i \rho_j$), we have characterised the qualitative behaviour of the DEEP, and constructed a preliminary phase diagram in the three-dimensional parameter space of the model. We have identified three distinct phases, which reflect those of the TASEP, namely a high density phase, low density phase and maximal current phase. However, the nature of the moving boundary conditions in this model (Section 3.1.3) means that the steady states must be defined with respect to a particular reference frame. The low density phase is stationary with respect to the tip; the high density phase is stationary with respect to the input; and the maximal current phase is not stationary with respect to any reference frame since the profile decays smoothly between both boundaries. In addition to the three phases, we have also identified a sub-phase which we refer to as the 'shock region'. Here, the extending system size introduces the novel scenario that a shock appearing in the bulk of the system can propagate forward with a velocity less than that of the tip. It thus remains in the system, unable to reach either boundary. In this case the density profile is stationary only in the reference frame of the shock.

The simple mean-field theory is, however, a crude analysis, and we do not expect it to provide us with quantitatively correct predictions. The shortfall of the approximation is that it does not account for correlations in the system, some of which are not insignificant, as we shall see in the following Subsection. In order to accurately predict the details of the phase structure, we now develop a refined mean-field theory which retains some information about the correlations.

3.3 Refined mean-field theory

As we have seen, the simple mean-field theory presented in the Subsection above relies on the assumption that *all* correlations between the occupancies at different sites can be neglected. While this is a safe assumption in the bulk of the system, we might expect that this is not the case close to the boundaries. In particular, the dynamics at the tip of the growing lattice dictate that the correlations here are especially important. In this section we aim to refine the theory by taking account of the correlations close to the tip. We construct a new set of mean-field equations and use these to rederive the phase diagram. We find that the phase boundaries are shifted significantly under this scheme, and we expect that the new phase diagram more accurately represents the exact behaviour of our model.

We begin our refinement of the mean-field theory by considering the two-point correlations in the model, i.e. $\langle \tau_i \tau_j \rangle$. If these correlations are strong, then

$$\langle \tau_i \tau_j \rangle \neq \langle \tau_i \rangle \langle \tau_j \rangle \,, \tag{3.45}$$

and the factorisations made in order to arrive at Equations 3.16–3.18 necessarily introduce some errors. In order to evaluate the error inherent in the simple mean-field approximation, we examine the two-point correlations between the first 100 pairs of sites in the DEEP lattice. The function plotted in Figure 3.13 is the difference between average correlated occupancies at neighbouring sites i and j (i.e. site i and site j are occupied simultaneously), and the product of the uncorrelated average occupancies at the same sites. These quantities were calculated using a Monte Carlo simulation (see Section 3.6) and provide us with a measure of the two-point correlation strength. On this plot one can see an exponential increase in correlation strength close to the tip, however between sites 1 and

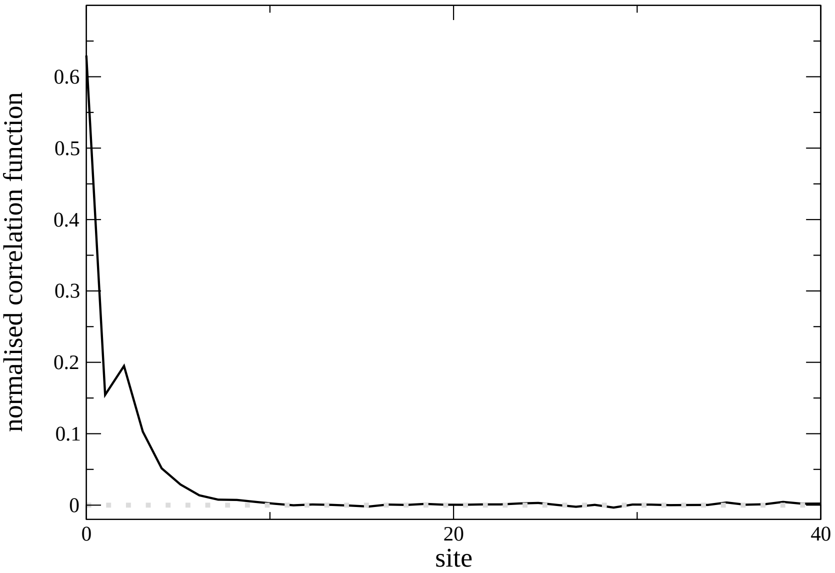

Figure 3.13: Normalised two-point correlation functions between pairs of neighbouring sites $(i, i+1)$ on the lattice of a DEEP, $\frac{\langle\tau_i\tau_{i+1}\rangle - \langle\tau_i\rangle\langle\tau_{i+1}\rangle}{\langle\tau_i\rangle\langle\tau_{i+1}\rangle}$. The large correlation strength between sites 1 and 2 can be attributed to correlated dynamics during a growth event.

2 there is an anomalously large correlation strength. This sharp increase might have been expected due to the correlated dynamics at the tip during a growth event: when the lattice grows, the result is that both site 1 and site 2 are vacated (See growth dynamics (3.3)).

With this consideration, we propose that our mean-field theory can be improved significantly by preserving the strongest two-point correlation, between sites 1 and 2. We introduce a refined mean-field theory which retains this correlation $\langle\tau_1\tau_2\rangle$ in (3.5-3.10). The factorisation scheme of (3.2) is replaced with the factorisation:

$$\langle\tau_1\tau_2\tau_i\rangle = \langle\tau_1\tau_2\rangle\rho_i \quad i \geq 3\ , \tag{3.46}$$

$$\langle\tau_i\tau_j\rangle = \rho_i\rho_j \quad i \textit{ or } j \geq 3 \quad (i \neq j). \tag{3.47}$$

As before, we wish to use the recurrence (3.16) to analyse the phase behaviour. Since (3.16) involves $\langle\tau_1\tau_i\rangle$, we must now begin the iteration at $i = 3$ rather than $i = 2$. We must therefore find a new expression for ρ_3 which does not require factorising $\langle\tau_1\tau_2\rangle$. We have from (3.12),

$$\rho_3 = \frac{J + \gamma\langle\tau_1\tau_2\rangle}{1 - \langle\tau_2\rangle}$$

and from (3.11)

$$\langle\tau_2\rangle = J + \langle\tau_1\tau_2\rangle\ .$$

Combining these two relations gives

$$\langle\tau_1\tau_2\rangle = \frac{\rho_3[1-J]-J}{\gamma+\rho_3}\ . \tag{3.48}$$

We have a new unknown, $\langle\tau_1\tau_2\rangle$, and so must introduce one further relation into the set of simultaneous equations (3.5-3.10). We consider the steady state rates into and out of the configuration in which site 1 is vacant and site 2 is occupied:

$$\frac{d\langle\tau_2[1-\tau_1]\rangle}{dt} = 0 = \langle\tau_3[1-\tau_2][1-\tau_1]\rangle - \langle\tau_2[1-\tau_1]\rangle + \beta\langle\tau_1\tau_2\rangle\ . \tag{3.49}$$

We can identify the second term as the exact current from (3.11). Thus we obtain another exact expression for the steady state current:

$$J = \langle\tau_3[1-\tau_2][1-\tau_1]\rangle + \beta\langle\tau_1\tau_2\rangle\ . \tag{3.50}$$

Under the refined mean-field scheme (3.47), we may factorise this expression beyond site 2. Using (3.11) to simplify, we thus obtain a new expression for ρ_3:

$$\rho_3 = \frac{J-\beta\langle\tau_1\tau_2\rangle}{1-J-\frac{J}{\gamma+\beta}}\ , \tag{3.51}$$

which along with (3.48), gives us a quadratic equation for ρ_3

$$\rho_3^2[1-J-\frac{J}{\gamma+\beta}] + \rho_3[(\gamma+\beta)(1-J) - \frac{\gamma J}{\gamma+\beta} - J] - (\beta+\gamma)J = 0\ . \tag{3.52}$$

This may be solved straightforwardly and the new three-dimensional phase surfaces are determined as in Section 3.2, by solving:

$$\rho_3 < \alpha\ , \tag{3.53}$$

$$\alpha < \rho_3 < 1-v-\alpha\ , \tag{3.54}$$

$$0 < v_{shock} < v_{tip}\ . \tag{3.55}$$

We present here, the detailed results only for the simple case of $\beta = 0$.

3.3.1 The case $\beta = 0$

In the simple case of $\beta = 0$, (3.51) reduces to

$$\rho_3 = \frac{J}{1-J-\frac{J}{\gamma}} \tag{3.56}$$

The condition for a low density phase, $\rho_3 < 1-v-\alpha$, is now

$$\alpha < \gamma \tag{3.57}$$

and the velocity as before is $v = \alpha(1-\alpha)/(1+\alpha)$. In the high density phase, $\gamma < \alpha$ and the velocity is $v = \gamma(1-\gamma)/(1+\gamma)$. For $\alpha/(2-\alpha) < \gamma < \alpha$ a dynamic shock exists between the high density tip region $\rho = \rho_+ = (1-\gamma)/(1+\gamma)$ and low density region $\rho = \alpha$ far from the tip. The maximum current phase is attained when $\alpha > \sqrt{2}-1$ and $\gamma > \sqrt{2}-1$.

3.3.2 Further correlations

One might expect that by taking into account more of the correlations near the tip, we will improve the approximation further; after all, an exact theory is one which takes into account all correlations. It is of interest then to repeat the refinement scheme of the previous section, and introduce a 'further refined' mean-field theory which keeps correlations between the first three sites. This means that now we factorise for example:

$$\langle \tau_1\tau_2\tau_3\tau_i \rangle = \langle \tau_1\tau_2\tau_3 \rangle \rho_i \quad i \geq 4 \,, \tag{3.58}$$

and we do not factorise any of the correlations $\langle \tau_1\tau_2 \rangle$, $\langle \tau_1\tau_3 \rangle$, $\langle \tau_2\tau_3 \rangle$ or $\langle \tau_1\tau_2\tau_3 \rangle$.

To keep the equations manageable, we keep to the limit $\beta = 0$. Under this scheme, we already we have 8 unknowns: τ_1, τ_2, τ_3, τ_4, $\langle \tau_1\tau_2 \rangle$, $\langle \tau_1\tau_3 \rangle$, $\langle \tau_2\tau_3 \rangle$, $\langle \tau_1\tau_2\tau_3 \rangle$. We must therefore solve 8 simultaneous equations in order to find $\rho_4(\alpha\ ,\gamma)$.

We start by identifying a set of exact equations from which to construct the mean-field equations required to find ρ_4. We already have the following exact equations from Section 3.1.2:

$$\frac{d\langle \tau_1 \rangle}{dt} = \langle \tau_2[1-\tau_1] \rangle - \gamma\langle \tau_1 \rangle \,, \tag{3.59}$$

$$\frac{d\langle \tau_2 \rangle}{dt} = \langle \tau_3[1-\tau_2] \rangle - \langle \tau_2[1-\tau_1] \rangle - \gamma\langle \tau_1\tau_2 \rangle \,, \tag{3.60}$$

$$\frac{d\langle \tau_3 \rangle}{dt} = \langle \tau_4[1-\tau_3] \rangle - \langle \tau_3[1-\tau_2] \rangle - \gamma\langle \tau_1[\tau_3-\tau_2] \rangle \,, \tag{3.61}$$

and from Section 3.3, we have

$$\frac{d\langle \tau_2[1-\tau_1] \rangle}{dt} = \frac{d\langle \tau_2 \rangle}{dt} - \frac{d\langle \tau_1\tau_2 \rangle}{dt} = \langle \tau_3[1-\tau_2][1-\tau_1] \rangle - \langle \tau_2[1-\tau_1] \rangle \,. \tag{3.62}$$

We construct a further three exact expressions, by considering correlation equations at the first three sites:

$$\frac{d\langle \tau_1\tau_2\tau_3 \rangle}{dt} = \langle \tau_4[1-\tau_3]\tau_2\tau_1 \rangle - \gamma\langle \tau_1\tau_2\tau_3 \rangle \,, \tag{3.63}$$

$$\frac{d\langle \tau_3[1-\tau_2][1-\tau_1] \rangle}{dt} = \langle \tau_4[1-\tau_3][1-\tau_2][1-\tau_1] \rangle - \langle \tau_3[1-\tau_2][1-\tau_1] \rangle + \gamma\langle \tau_1\tau_2 \rangle \,, \tag{3.64}$$

$$\frac{d\langle \tau_3[1-\tau_2] \rangle}{dt} = \langle \tau_4[1-\tau_3][1-\tau_2] \rangle - \langle \tau_3[1-\tau_2] \rangle + \gamma\langle \tau_1\tau_2 \rangle - \gamma\langle \tau_1[1-\tau_2]\tau_3 \rangle \,. \tag{3.65}$$

Equation 3.63 gives the rate change of the configuration in which the first three lattice sites are occupied. Equation 3.64 gives the rate change of the configuration in which site

3 is occupied and sites 2 and 1 are unoccupied. Equation 3.65 gives the rate change of the configuration in which site 3 is occupied and site 2 is unoccupied. In the steady state, all of the above (3.59–3.65) are equal to zero. We saw in Section 3.1.5, that one may identify terms in the correlation equations with the particle current J, which in the steady state is constant everywhere. From (3.59–3.62), we have four independent exact expressions for the current:

$$J = \gamma\langle\tau_1\rangle; , \tag{3.66}$$

$$J = \langle\tau_2[1-\tau_1]\rangle , \tag{3.67}$$

$$J = \langle\tau_3[1-\tau_2]\rangle - \gamma\langle\tau_1\tau_2\rangle , \tag{3.68}$$

$$J = \langle\tau_3[1-\tau_2][1-\tau_1]\rangle . \tag{3.69}$$

By setting the left hand side of (3.63–3.65) equal to zero, we obtain four more independent equations:

$$\langle\tau_4[1-\tau_3]\rangle = \langle\tau_3[1-\tau_2]\rangle + \gamma\langle\tau_1[\tau_3-\tau_2]\rangle , \tag{3.70}$$

$$\langle\tau_4[1-\tau_3][1-\tau_2]\rangle - \langle\tau_3[1-\tau_2]\rangle + \gamma\langle\tau_1\tau_2\rangle = \gamma\langle\tau_1[1-\tau_2]\tau_3\rangle , \tag{3.71}$$

$$\langle\tau_4[1-\tau_3][1-\tau_2][1-\tau_1]\rangle = \langle\tau_3[1-\tau_2][1-\tau_1]\rangle - \gamma\langle\tau_1\tau_2\rangle , \tag{3.72}$$

$$\langle\tau_4[1-\tau_3]\tau_2\tau_1\rangle = \gamma\langle\tau_1\tau_2\tau_3\rangle . \tag{3.73}$$

We now have 8 exact equations, forming a closed system of equations for our 8 unknowns. We factorise according to (3.58), and using Equations (3.66–3.69), we can eliminate τ_1, τ_2, $\langle\tau_2\tau_3\rangle$ and $\langle\tau_1\tau_2\tau_3\rangle$ respectively. We are left with four equations for ρ_4:

$$\rho_4 = \frac{\gamma\langle\tau_1\tau_3\rangle + J}{1-\tau_3} , \tag{3.74}$$

$$\rho_4 = \frac{J + \gamma^2\langle\tau_1\tau_2\rangle}{1 - 2J - (1+\gamma)\langle\tau_1\tau_2\rangle} , \tag{3.75}$$

$$\rho_4 = \frac{J - \gamma\langle\tau_1\tau_2\rangle}{1 - 2J - J/\gamma} , \tag{3.76}$$

$$\rho_4 = \frac{(1+\gamma)\gamma\langle\tau_3\rangle - \gamma^2\langle\tau_1\tau_2\rangle}{\langle\tau_1\tau_2\rangle - \langle\tau_1\tau_3\rangle} . \tag{3.77}$$

Note that now we have two equations, 3.75 and 3.76, containing only two variables. We rewrite 3.75:

$$\langle\tau_1\tau_2\rangle = \frac{\rho_4[1-2J] - J}{\gamma^2 + \rho_4[1+\gamma]} \tag{3.78}$$

which with 3.76 finally gives a quadratic for ρ_4, with positive solution

$$\begin{aligned}\rho_4 = &\frac{\gamma[4J-1]+\gamma^2[2J-1]}{2[\gamma - J - 3\gamma J - \gamma^2 + 2J\gamma^2]}\\ &- \frac{\gamma\sqrt{4\gamma^4 J[J-1] + 2\gamma^3[1-4J+4J^2] + \gamma^2[1-2J] + 2\gamma[J-4J^2] - 3J^2}}{2[\gamma - J - 3\gamma J - \gamma^2 + 2J\gamma^2]} \; .\end{aligned} \tag{3.79}$$

We now compare this result with ρ_4 calculated under the refined mean-field approximation scheme of Section 3.3. In the event of these theories being exact, the ρ_4 from both approximation schemes should be the same. Under the refined mean-field theory, ρ_4 can be calculated by setting $\beta = 0$ in Equation 3.51, we then have for ρ_3:

$$\rho_3 = \frac{J}{1 - \frac{J}{\gamma} - J} \; .$$

We have from Equation 3.12

$$J = \langle \tau_4[1-\tau_3] \rangle - \gamma \langle \tau_1 \tau_3 \rangle \; ,$$

which factorises according to (3.47) to become:

$$J = \rho_4(1-\rho_3) - \gamma \rho_1 \rho_3 \; .$$

We thus arrive at an expression for ρ_4:

$$\rho_4 = \frac{J(1-\frac{J}{\gamma})}{1 - \frac{J}{\gamma} - 2J} \tag{3.80}$$

One can see that 3.79 and 3.80 are not identical, however plotting the functions side by side reveals that they are rather similar. Figure 3.14 shows the two functions plotted for comparison. The plot is calculated in 3D α and γ parameter space, with $J = \alpha(1-\alpha)/(1+\alpha)$. This corresponds to the low density current (3.40) which holds irrespective of which mean-field approximation is used (since it can be calculated in the bulk where all correlations are small). That the two functions are not identical tells us that the theories have not converged to a common solution.

The phase boundaries can be calculated by solving e.g. $\rho_4 < 1 - J - \alpha$, $\rho_4 < \alpha$, $J_{l.d} = J_{max}$ and $J_{h.d.} = J_{max}$.

3.4 The phase diagrams and a comparison of theories

For comparison of the mean-field theories, the basic 2-D phase diagrams for $\beta = 0$, showing transitions between the high and low density phases; the high and maximal current phases; and the subregions of the low density phase; for the simple, refined and further refined mean-field theories are plotted in Figure 3.15.

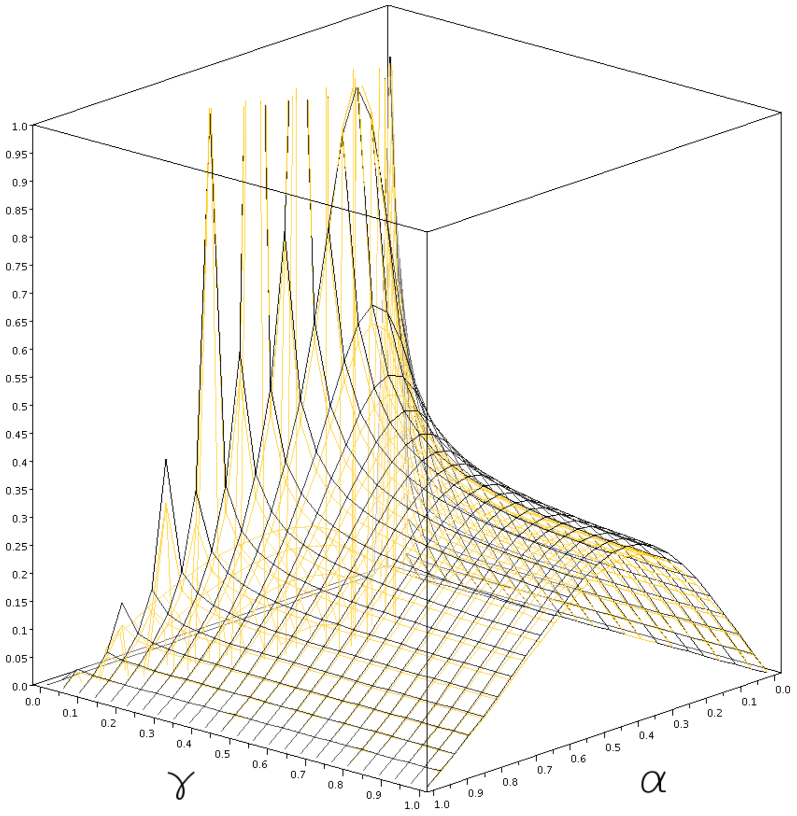

Figure 3.14: Comparison of ρ_4 calculated from the refined mean-field and the further refined mean-field theories. The vertical axis is ρ_4. The functions plotted are Equation 3.80 (yellow) and Equation 3.79 (black). Both functions are evaluated using the low density current relation (3.40) and are thus valid for ρ_4 only in the region $\alpha < \gamma$ (low density phase).

The theories of Sections 3.2–3.3.2 concur on the qualitative phases of the DEEP, but the phase boundaries predicted by each theory differ. The transition between the low density and the maximal current phases (3.32) is the only transition that is the found to be the same in each theory. This is because it comes from the condition that the roots of the recursion (3.16) are real, which reduces to a condition relating the tip velocity to the steady state current. In the low density phase, both of these quantities can be calculated in the bulk, where the density quickly converges to a constant value (α) and we can safely assume in any of the approximation schemes that $\rho_i = \rho_{i+1} = \alpha$.

The other transitions vary significantly. In particular, a large difference is seen between all three mean-field theories in the line separating subregions in the low density phase where decay to the bulk value (α) starts from above or below α. This line warrants some comment. We note that on the phase diagram of the TASEP (Figure 2.1.1), there is an equivalent line in α–β space, ($\alpha = 1-\beta$) on which the left boundary and the right boundary are equal, and the whole density profile is flat. On this line, the mean-field theory is exact. In the DEEP, however, due to the growth dynamics at the tip, there is always some density structure across the first few sites. We thus do not expect an equivalent line to exist in the α–γ space of the DEEP phase diagram, where density profile is flat and the mean-field approximations are exact. One can see, for example, by substituting $\tau_i = \alpha\ \forall\alpha$ into the exact correlation equation for site 2 (3.6) that a flat density profile is not a steady state solution for the DEEP.

In the refined and further refined mean-field theories, the transition line between high and low density phases is not identical, but it is rather close, especially for small α and γ. This transition line is, however, predicted to lie significantly lower in the simple mean-field theory. The position of this line is again dependent on the starting value for the recursion. The simple mean-field theory has a smaller high density region than the other theories, telling us that ρ_2 calculated in this theory is lower than ρ_3 and ρ_4 calculated in the refined and further refined theories respectively.

The transition out of the high density, into the maximal current phase is dependent on the form of the current and velocity in the high density phase. In turn, these quantities can be determined from their low density counterparts at the phase transition between high and low density phases. Thus the difference in the high density to maximal current phases.

3.5 Heuristic argument: a discussion of symmetry

Given the differing conclusions of each of the three mean-field theories presented above, we now stop to consolidate the model with a heuristic argument. Rather than examining the details of the correlation functions, we ask; does our model have any symmetries which can help us understand its behaviour? And how might we expect the phase structure of the DEEP to reflect that of other exclusion processes?

An important feature which allows us to understand the phase behaviour of the TASEP

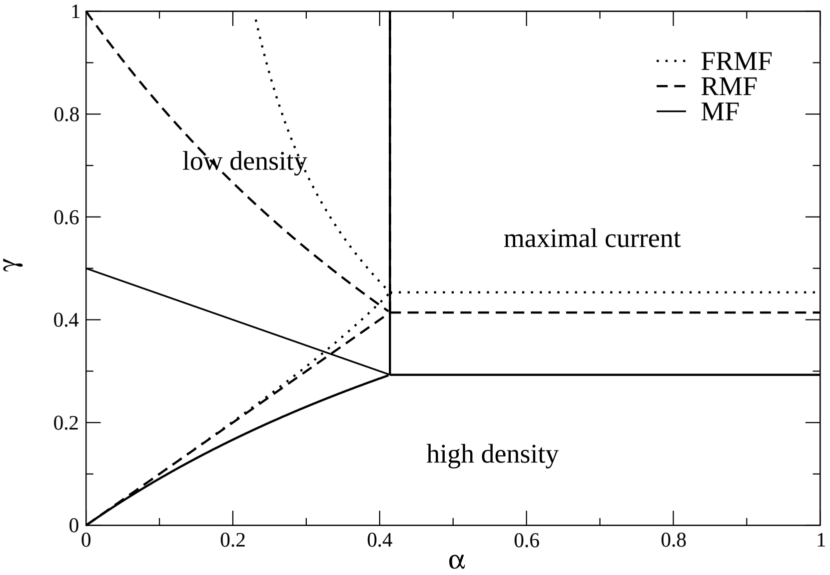

Figure 3.15: Comparison of three mean-field approximations in the case $\beta = 0$. The transition from the low density phase to the maximal current phase occurs at $\alpha = \sqrt{2} - 1$ for all three theories. The other transition lines vary for the different theories.

(see Figure 2.1.1) is the presence of a symmetry between particles hopping in one direction and 'holes' hopping in the opposite direction. The high density particle phase can therefore be understood as a low density hole phase and vice versa. Due to the moving boundary condition and the transition during growth (3.3), there is no exact microscopic symmetry between particles and holes in the DEEP dynamics. However, it is true that particles leave and holes enter at the tip whereas particles enter and holes leave at the right end. It is plausible then that there exists some symmetry between the high density phase (low density of holes) and the low density phase (high density of holes). Indeed, the phase boundaries between the high, low and maximal current phases predicted by the refined mean-field theory in the limit of $\beta = 0$ display a symmetry under the interchange $\alpha \leftrightarrow \gamma$. But while the velocities in the two phases, $\alpha(1-\alpha)/(1+\alpha)$ and $\gamma(1-\gamma)/(1+\gamma)$, are also symmetric under the interchange $\alpha \leftrightarrow \gamma$, the bulk densities in these phases, α and $(1-\gamma)/(1+\gamma)$, are not symmetric.

In the case of $\beta \neq 0$, the refined mean-field approximation no longer displays a particle hole symmetry. However, the heuristic argument which we now describe leads to a 3D phase transition between the high and low density phases which does maintain a symmetry between input rate α and output rate $\beta + \gamma$.

If we ignore the density structure near the tip and assume that in the high density phase there exists a single high density value associated with the tip: $\rho_1 = \rho_{bulk}$, in the same way that in the low density phase, we have a single density α associated with the input end of the lattice, then from (3.12-3.13) we have the following:

$$v = \gamma \rho_1 = \frac{\rho_1(1-\rho_1)}{1+\rho_1+\frac{\beta}{\gamma}} \; . \tag{3.81}$$

This is solved to give the bulk density:

$$\rho_1 = \rho_{bulk} = \frac{1-\gamma-\beta}{1+\gamma} \; , \tag{3.82}$$

and associated high density velocity:

$$v = \frac{\gamma(1-\gamma-\beta)}{1+\gamma} \; . \tag{3.83}$$

As before we appeal to the concept of a shock discontinuity in the system. The low density phase is reached when the shock velocity $(1-\rho_+ - \alpha)$ is greater than the tip velocity (3.83), which corresponds to a phase transition at:

$$\alpha = \beta + \gamma \; , \tag{3.84}$$

suggesting an exact correspondence between the balancing of input and output rates and the transition between high and low density phases. In the limit $\beta = 0$, this boundary is the same as that derived by the refined mean-field theory, and is in fact very close to that derived in the case $\beta \neq 0$ (see Figure 3.20 in the next Section). The remaining phase boundaries are derived as in Section 3.2.

When considering the DEEP in terms of holes entering the lattice from the left, we note with interest an apparent similarity between the DEEP, and the model of [Lakatos 03]. In this work (see Section 2.1.5), the TASEP is generalised to admit particles of arbitrary size. The expressions derived in [Lakatos 03] for the current as a function of particle size d are:

$$J = \frac{\alpha(1-\alpha)}{1+(d-1)\alpha} \; , \tag{3.85}$$

in the low density phase, and:

$$J = \frac{\beta(1-\beta)}{1+(d-1)\beta} \; , \tag{3.86}$$

in the high density phase. One can see immediately that there is an exact symmetry between input rate α and output rate β. Appealing to this symmetry, the second expression (3.86) can be understood as the current of holes in a low hole density phase, where holes of length d are inserted into the lattice with rate β.

Now notice that if we set $d = 2$, and swap $\beta \to \gamma$, then (3.85 and 3.86) are exactly the expressions found in Section 3.3 for the low and high density currents in the limit of $\beta = 0$. Indeed, if we consider a growth event of the DEEP (3.3) in terms of holes, we see that the growth of the lattice by one site is equivalent to admitting *two* holes at the left boundary, i.e. a hole of length $d = 2$, with rate γ. With this reasoning one can envisage

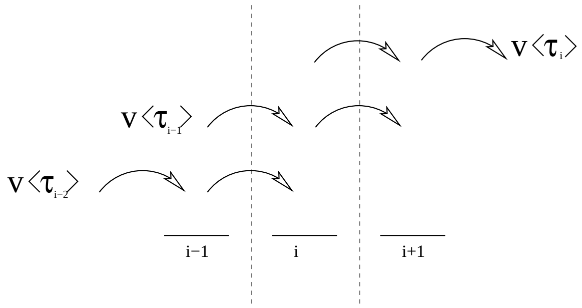

Figure 3.16: The current generated in the bulk of a DEEP lattice due to the updating of indices during a growth event in which the lattice extends by *two* lattice sites. A particle from site $i-1$ passes through site i completely.

some correspondence between the two models.

The analogy between the DEEP and the model of [Lakatos 03] can be taken further by considering a DEEP in which the lattice extends by an arbitrary number of sites. Consider for example that one particle at site 1 can transform into 2 new lattice sites, i.e.

$$1 \to 000\ . \tag{3.87}$$

We now have a new site 1 and site 2; and in order to keep the left-most site labelled as site 1, the transformation (3.87) requires updating all sites $i \to i+2$. The effect on the current is best understood by considering what happens at site a i in the bulk during a growth event. The particle at site $i-1$ is shifted into site i with the first added lattice site, then with the second added lattice site this particle leaves site i and is shifted into site $i+1$. Thus, in addition to gaining the particle from site $i-2$, site i experiences the current due to the particle from site $i-1$ passing completely through it. This process is illustrated diagrammatically in Figure 3.16. We can construct the expression for the current between sites $i+1$ and i by considering, as before, the flow of particles into site i from site $i+1$, due to hopping events, and the flow out of site i and into site $i+1$ due to the update of indices described above;

$$J = \langle \tau_{i+1}[1-\tau_i] \rangle - v\langle \tau_i + \tau_{i-1} \rangle\ . \tag{3.88}$$

If we assume that a low density steady state exists as before, where the bulk density is uncorrelated and equal to α, then with $J = v$ (since we're in the $\beta = 0$ limit), we have:

$$J = \frac{\alpha(1-\alpha)}{1+2\alpha} \tag{3.89}$$

which is in agreement with (3.85), with $d = 3$. The implications of this analogy are rather interesting. Clearly in the DEEP, once the holes move away from the boundary they progress as single holes, whereas in [Lakatos 03] the particles continue to occupy d lattice sites, yet the above argument suggests that the bulk current is unaffected by this difference.

Perhaps one can gain some insight into the model of [Lakatos 03], by considering the effect of particles of large spatial extent on the current to be analogous to a shift in reference frame.

We now have several theories for predicting the behaviour of the DEEP, but it remains to verify their accuracy. Quantities such as the precise positions of the phase transitions and the functional forms of the current and velocity in the different phases are all verifiable, by simulating the stochastic dynamics of the DEEP. Using results calculated from simulations, we can compare the various mean-field approaches with exact results and determine the merits and shortfalls of each approximation scheme. To this end, we now determine the true colours of the DEEP, with a numerical Monte Carlo approach.

3.6 Monte Carlo simulation

Whereas the approaches of Sections 3.2–3.3.2 all require solving for the DEEP dynamics in a particular reference frame, and making assumptions about the correlations and boundary effects; a Monte Carlo method (see Section 2.1.4) provides the opportunity to realise the full dynamics of the DEEP, across the entire lattice, without these limitations. In this Section we shall introduce the Monte Carlo algorithm, and compare the results generated from simulation with those of the analyses above. For simplicity, we work primarily in the $\beta = 0$ limit. Note that in this limit the refined mean-field theory of Section 3.3 and the heuristic argument of Section 3.5 are in agreement.

3.6.1 The algorithm

Simulations were carried out using discrete time random sequential updates on an array of binary values representing τ_i. For an array of size N, the update algorithm was as follows:

- select a site at random $[1..N]$
- attempt a transition with the prescribed probability
- update time $t \to t + dt/N$

Thus one ‘time step’ dt consists of N updates and on average each site has one update attempt per time step. Note that during a single time step the system may increase in length. In principle, this would affect our unit of time, however, such an increase, typically of one lattice unit, will be insignificant in the large N limit.

The probabilities, P, for the stochastic dynamics are calculated such that the efficiency of the algorithm is maximised while the rates (3.1-3.4) are preserved, i.e.

$$P_\alpha = \alpha dt$$

To account for rates which are greater than 1, they are normalised to the greatest escape rate for any particle, for example, if $\alpha > (\beta + \gamma) > 1$,

$$P_\alpha = 1 \ , \tag{3.90}$$

$$P_\gamma = \frac{\gamma}{\alpha} \ , \tag{3.91}$$

$$P_\beta = \frac{\beta}{\alpha} \ , \tag{3.92}$$

$$P_{hop} = \frac{1}{\alpha} \ , \tag{3.93}$$

$$dt = \frac{1}{\alpha} \ . \tag{3.94}$$

Our aim is to allow the system to reach a steady state, and calculate quantities such as site densities, particle flux and rate of change in lattice length.

Note that this algorithm has the inherent problem that as $N \to \infty$, the computational cost for each time-step increases. If we wish to reduce computational time, we may get around this problem by considering a fixed length portion of the lattice in a particular frame of reference. For example, in the low density phase we expect that the density tends exponentially to α, so we may truncate the lattice at site $M < N$ and set $\langle \tau_M \rangle = \alpha$, thus simulating only the M sites nearest the tip. This method will only work for the steady state phases which are clearly defined in some reference frame, which we may wish to determine first on a simulation of the entire lattice. For the maximal current phase and shock region, which do not have clearly defined reference frames, we must still in general consider the whole system.

3.6.2 Density profiles

The density at a given site can be calculated in one of two ways: a time averaged occupancy calculated during the simulation of a single lattice; or an ensemble averaged occupancy calculated over an ensemble of many lattices at a fixed length and thus fixed time. To find density profiles which are stationary in time, the former method can be used, while for profiles which are dynamic, the latter is more appropriate.

An example of each type of density profile is plotted in Figure 3.17. We see the four phases described by the mean-field theories. In the low density phase, the steady state densities are calculated in the reference frame of the tip. In the high density phase, they are calculated in the reference frame of the input. For profiles in the dynamic shock region and the maximal current phase, ensemble averages are used since the system is never in a truly stationary state.

3.6.3 Tip velocity and location of phase transitions

We can locate the exact positions of the phase transitions by considering the lattice tip velocity, which is given by a simple function of the parameters and changes form across

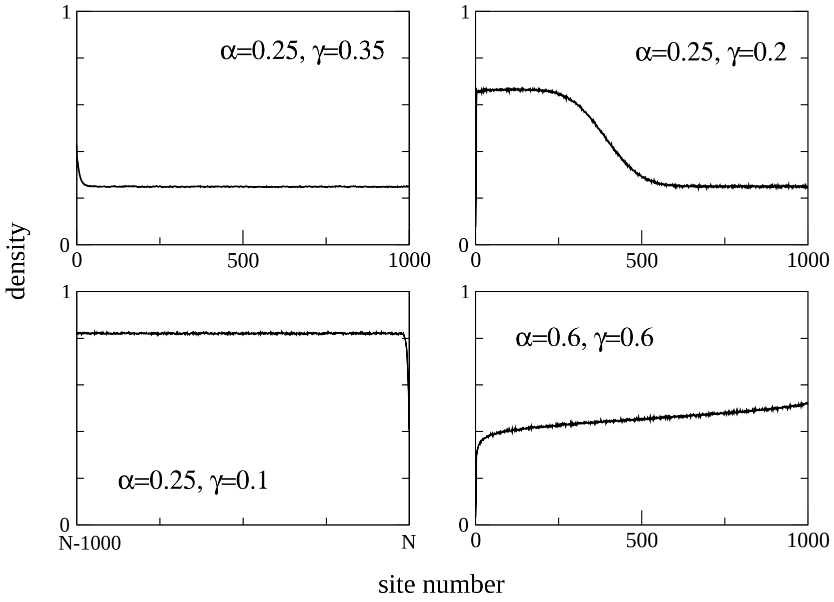

Figure 3.17: Density profiles from the different phases of the dynamically extending exclusion process. From top left: low density, shock profile, high density and maximal current phase. Note that since the high density profile is calculated in the reference frame of the input, the sites are labelled from $N - 1000..N$. The particles are injected at site N and the tip is progressing forward with a constant high density.

the phase boundaries. (See Equations 3.22, 3.25, 3.30). We find from the velocity of the simulated lattices, that the refined mean-field theory appears to predict the correct form for the tip velocity and the correct phase transitions. Figure 3.18 shows the velocity of a simulated lattice plotted for different values of γ, against the refined mean-field expression for the velocity. The velocities closely follow the predicted curve (3.40) and as expected, a phase transition takes place at $\alpha = \gamma$, where the velocity becomes independent of α. The maximum velocity is reached when $\alpha = \sqrt{2} - 1$ and $\gamma \geq \sqrt{2} - 1$.

Further evidence in support of the refined mean-field theory can be found by exploring the density profiles of the low density region, where the three theories predict different transitions between profiles which decay at the tip from below and above α. In Figure 3.19, we see that the transition appears to agree with that predicted by the first refined theory, while being at odds with both the further refined and the simple approximations.

For completeness, we consider now the case of non zero β. In Figure 3.20 the simulated growth velocities are compared to the refined mean-field theory velocity functions for the high and low density phases for $\beta \neq 0$. The high density velocity obtained from the heuristic argument is also shown and one may see that this coincides rather closely with the refined mean-field result. In this case it is simpler to work with the velocity as a function of γ (due to the nature of Equation 3.52 and inequality $\rho_3 < 1 - v - \alpha$, which must be solved simultaneously). Therefore, simulations were carried out with fixed values

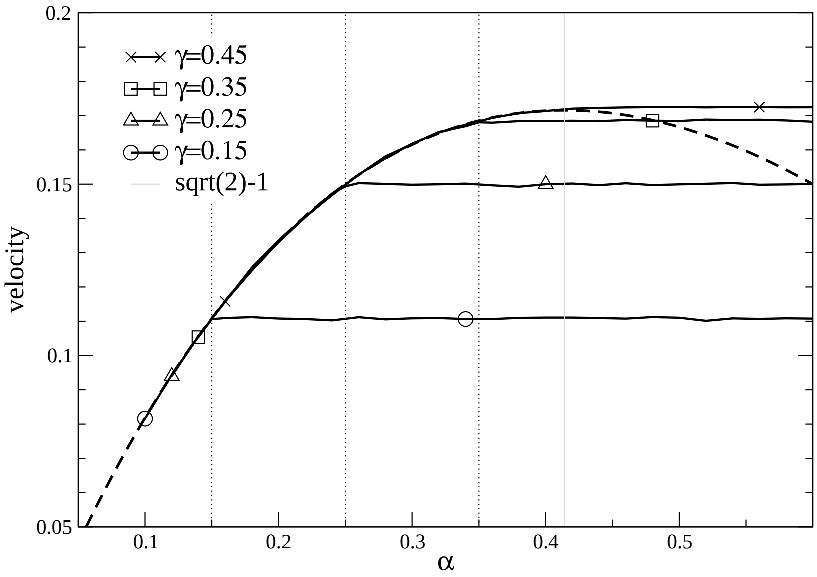

Figure 3.18: The tip velocity plotted against α for $\gamma = 0.15..0.45$ and $\beta = 0$. For $\gamma < \sqrt{2}-1$, a clear phase transition occurs when $\alpha \approx \gamma$. This transition is from the *low density* phase where $v = \frac{\alpha(1-\alpha)}{1+\alpha}$ (dashed line) to the *high density phase*, where the velocity is α independent. For clarity, dotted lines are used to indicate $\alpha = \gamma$. When $\gamma = 0.45 > \sqrt{2}-1$, the maximum velocity occurs as predicted at $\alpha = \sqrt{2}-1$.

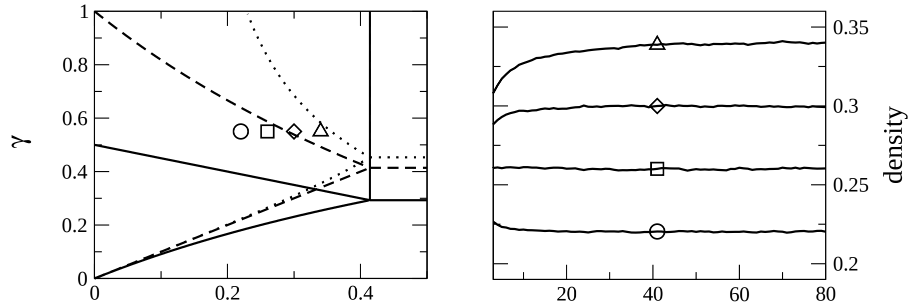

Figure 3.19: In the left-hand plot, the simple (solid line), refined (dashed line) and further refined (dotted line) phase boundaries are shown. Simulations were carried out in the low density phase, across the predicted boundary between profiles with a decay from above and below α (parameter values indicated with symbols). The resulting profiles, shown in the right-hand plot, display a transition that is in best agreement with the refined mean-field transition line.

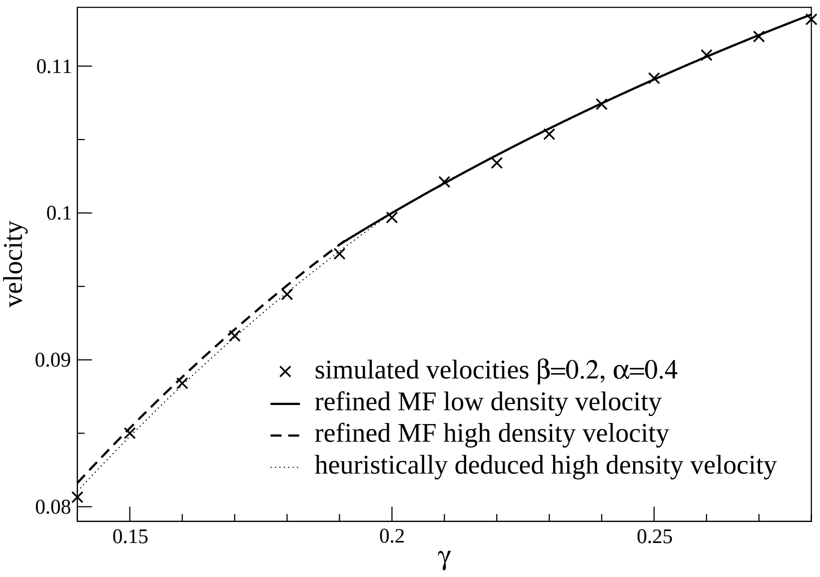

Figure 3.20: Theoretical and simulation results for the tip velocity as a function of γ, given for fixed values of α and $\beta > 0$. The data points show simulation results, fitted to the heuristic and refined mean-field functions for the tip velocity in the high and low density phases. The low density velocity is the same for heuristic and mean-field approaches and is given by (3.22). The high density velocity function is found in the refined mean-field theory by solving Equation 3.52 and inequality $\rho_3 < 1 - v - \alpha$ (explicit expression for the high density velocity is not presented here). The heuristic high density velocity is given by (3.83). The phase transition occurs at approximately $v_{ld} = v_{hd}$

$\alpha = 0.4$ and $\beta = 0.2$, in the range close to the phase transition $\gamma = 0.14..0.28$. We see a good agreement of the simulation data points with the high density and the low density velocity functions predicted by the refined mean-field theory. Note however, that in the high density phase the simulation results appear after all to be in best agreement with the *heuristic* result for the velocity (3.83). The phase transition occurs at the point where the high and low velocity functions meet.

3.7 Summary of results and conclusion

The DEEP model defined in Subsection 3.1.1 is a generalisation of the TASEP to a system with a dynamic system size. The particles themselves provide the mechanism by which the lattice extends: as particles reach the end of the lattice, they are able to transform into a new site which is added onto the end of the lattice. In the analyses of this chapter we have shown that the well known phases of the open boundary TASEP (see Subsection 2.1.1 and figure therein) are reflected in the phase diagram of this model (Figure 3.15). There is a low density phase which is limited by a slow input rate far from the tip (Figure 3.9), and a high density phase where the limitation is a slow growth rate (see Figure 3.10). Intermediate between these phases is a *dynamic shock region* (Figure 3.10), which arises as a result of the unique boundary conditions of this model. In the dynamic shock region a shock exists in the system between a high density plateau at the tip and a low density plateau matching the input rate far from the tip. The velocity of the shock can be derived from the conservation of mass (Subsection 2.1.3). In the case of the low and high density phases, a shock forming in the bulk of the system travels with a velocity that is adequate to drive it completely to one of the boundaries (see Figure 3.12). In the shock region however, the shock moves with a velocity between zero and v_{tip} and thus moves away from both boundaries. The result is that in this region of the phase diagram, a shock persists in the system. In the DEEP an analogue of the maximal current phase of the TASEP also exists, though in this system it does not constitute a steady state, since the density decays from both boundaries (Figure 3.11) and thus evolves continuously as the system increases in size.

Our analysis of the DEEP consists of several mean-field approaches (Sections 3.2–3.3.2) to solving the correlation functions for this system (Equations 3.5–3.7), and the use of Monte Carlo simulations to verify them (Section 3.6). We have found that while the simplest mean-field approach (which assumes that all correlations can be ignored) successfully predicts the qualitative behaviour of the phases, the phase boundaries are not accurately predicted. Our refined mean-field approximation which preserves the correlation between the first two sites (Section 3.3) predicts a phase diagram which appears to coincide very closely with simulation results. A heuristic argument leads us to a phase diagram which agrees exactly with that of the refined mean-field theory for the case $\beta = 0$, and also remains close for the case $\beta \neq 0$. We find that a further refined mean-field theory (Section 3.3.2) which preserves the correlations between the first three sites predicts a phase diagram which, although closer to the simulation results than the simple mean-field theory, does not improve upon the predictions of the first refined mean-field theory. One might expect that with further refinements, made by taking more correlations into account, the theories would converge to the correct phase diagram. Our findings appear to indicate, however, that the correlations of singular importance in the DEEP are those between sites 1 and 2. This is likely a direct result of the growth dynamics, which entail the simultaneous vacation of both of these sites.

The results of the most successful of our mean-field theories, the refined mean-field theory in the limit $\beta = 0$, are summarised in the detailed 2-D phase diagram shown in Figure 3.21. The diagram is split into the three distinct phases: high, low and maximal current. The low density phase is split into two subregions I and II, where the tip decays to the bulk density from above and below respectively. The shock region, where the shock recedes from both boundaries, is indicated within the high density phase. We believe this to be, at least, an accurate approximation to the exact phase structure of the DEEP.

This model was introduced initially to describe the growth process of fungal hyphae. The presence of a steady state where the density remains constant with respect to the tip and the tip advances with a constant velocity is the first requirement for this model to be applicable in the context for which it was intended. We thus take particular interest in the

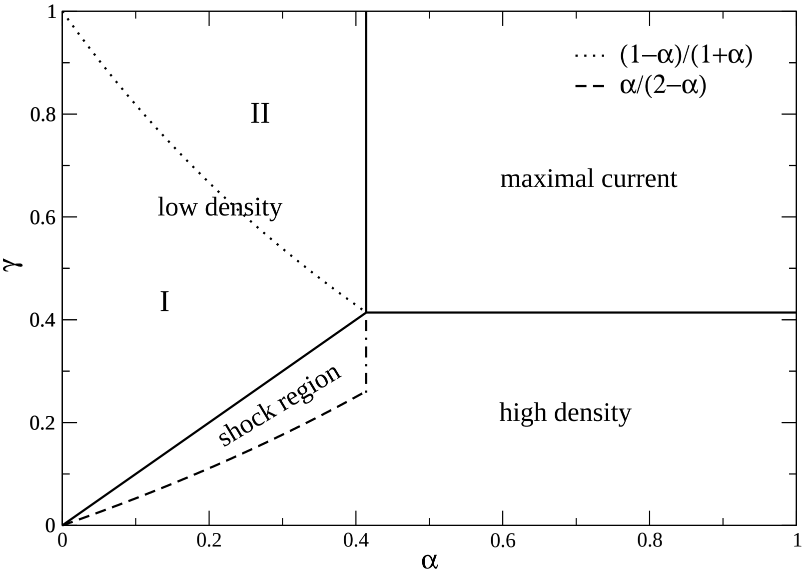

Figure 3.21: The phase diagram obtained from the refined mean-field approximation in the limit $\beta = 0$. Three phases are shown. The low density phase is split into subregions I and II, indicating regions where the density profile decays from above and below the bulk density respectively. The shock region is indicated within the high density phase.

low density phase, which is a steady state defined in the reference frame of the tip. Here, within the mean-field approximations, the tip velocity is given by a simple function of the input rate, α, far from the tip, and the efficiency with which particles contribute to the growth (β/γ). This relation is one that could be tested experimentally, for example by live-cell imaging the dynamics of the motor proteins or vesicles fused with the green florescent protein [Schuchardt 05]. It is also interesting to note that, due to the exclusion dynamics, particles can undergo 'jamming' as they exit the lattice and that density profiles in the low density phase can therefore have a peak in the density close to the tip (Figures 3.9 and 3.17). We speculate that this peak could be associated with the formation of the high density region of the Spitzenkörper (Section 2.2.1, Figure 2.5) at the tip of a real growing hypha. It would be of interest to investigate the relationship between our model parameters and Spitzenkörper formation experimentally. For example, one could alter the rate at which vesicles fuse with the tip with chemical inhibitors or temperature variations, and the vesicle supply could be disrupted by inhibiting microtubule formation far from the tip. The effect of these disruptions on the Spitzenkörper could then be observed using live-cell imaging techniques [Hickey 05].

In terms of describing the actual internal dynamics of a growing fungal hypha, however, the dynamics of the DEEP are, of course, very crude. While our model's lack of complexity allows us a transparent analysis and intuitive understanding of the system, we note that it may be of interest to study extensions to this model which capture more of the details of the growth mechanism. One possible extension would be to model more explicitly the complex distribution of microtubules inside the hypha. The discontinuity of the microtubule segments could be taken into account, for example, by introducing ‘defective’ sites, where the hopping rates differ from the rest of the lattice, to mimic gaps between adjacent microtubules. In studies of the TASEP, the introduction of defective sites, has been found to cause discontinuities in the density profiles and to affect the particle current [Dong 07, Chou 97].

Another clear extension to the model is to continue using a mean-field description of the microtubules, but to introduce a mechanism by which particles can detach from the microtubule track and diffuse freely for some time. This serves to mimic the real situation whereby vesicles only process along a microtubule for a limited amount of time before disassociating, and then reassociating some time later. A vesicle may undergo many such transitions on and off the microtubule during their progression toward the site of growth, and it is of interest to study the effect that this extra degree of freedom has on the possible density profiles of our model. We shall explore this question in the following chapter.

Chapter 4

The DEEP coupled to a SSEP

4.1 Introduction

In Chapter 3, we saw the analysis of a dynamically extending exclusion process, introduced in Chapter 2 to provide a coarse-grained model for the transport of materials through a fungal hypha and its subsequent growth. The key assumption of this model is that the presence of molecular motors coupled to microtubule tracks generates a net directed motion of mass inside the hypha; and that the materials delivered to the hyphal tip contribute to its extension. This assumption, however, omits a rather marked feature of molecular motor transport dynamics. As discussed in Section 2.1.5, we know from studies which image the dynamics of individual molecular motors, that in reality the motion of a motor does not consist simply of a continuous progression from one end of a microtubule to the other. The journey of a molecular motor involves, rather, short intervals of progression along a microtubule interspersed with periods of disassociation from the microtubule and diffusion in the surrounding cytoplasm. In this way, a motor may interact with several different microtubules before it reaches its destination.

In the following chapter we shall explore an extended version of the DEEP model for fungal hyphal growth, which accounts for the additional dynamics of motor exchange between the microtubules and the cytoplasm.

The chapter is organised as follows: we begin by constructing the new extended model, which incorporates a second lattice representing the cytoplasm surrounding the microtubule. The motors on this second lattice are referred to as ‘unbound particles’ and the lattice is referred to as the ‘unbound lattice’. We define the full dynamics of the model, which now includes three new parameters. We then show, through a simple mean-field continuum approximation, that some qualitative changes in the behaviour of the DEEP are implied. The behaviour includes new possibilities for the formation of stationary shock solutions. Our findings are illustrated with numerical iteration of the mean-field equations, and then the full dynamics are investigated with the application of Monte Carlo simulations. We show, through simulation results, some of the novel behaviour that emerges from the DEEP with attachment and detachment dynamics. The chapter is concluded with a summary of the results and some suggestions for further work in this area.

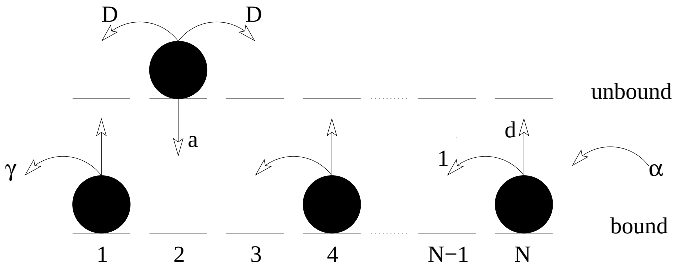

Figure 4.1: The dynamics of the DEEP coupled to a symmetric simple exclusion process. Particles on the 'unbound' lattice (top) can hop in either direction, with rate D. Particles on the 'bound' lattice (bottom) hop to the left with rate 1. The exchange of particles between bound and unbound lattices occurs with rates a and d, as indicated. Growth is controlled only by particles on the bound lattice and occurs from site 1 with rate γ. Injection is only into the bound lattice and occurs with rate α.

4.2 The DEEP with attachment and detachment

The on-off dynamics of motors is incorporated into the DEEP, by coupling it to a second lattice which contains the unbound particles. On the unbound lattice, particles may hop in either direction. This is essentially a symmetric simple exclusion process (SSEP) [Derrida 02], and represents the free diffusion of the motors in the cytoplasm. The two lattices interact with each other through the exchange of particles. In addition to the three parameters of the DEEP (α, β and γ), we include three new parameters in the model: the rate of attachment from unbound to bound lattices, a, the rate of detachment from bound to unbound lattices, d, and the rate of diffusion on the unbound lattice, D. Since we now have three new degrees of freedom, we choose to reduce the complexity of our problem somewhat, by working in the limit of $\beta = 0$. This construction is similar to that used in [Lipowsky 01], where motor dynamics were studied in open tubes of fixed length.

The model now has the following dynamics: Particles on the bound lattice are injected at the right with rate α; hop to the left with rate 1, extend the lattice with rate γ, and detach with rate d (entering the corresponding site of the unbound lattice). Particles on the unbound lattice hop to the right and to the left with rate D and attach to the bound lattice with rate a. As before, exclusion applies, meaning e.g. that a particle can only exchange lattices if there is a vacancy in the reciprocal site. The model dynamics are illustrated schematically in Figure 4.1.

4.3 Qualitative analysis

We can largely determine the qualitative behaviour of this system from the two correlation equations which describe the particle dynamics in the bulk of the bound and the unbound lattices. By simply examining the structure of these equations, we are able to determine some of the basic features of the stationary states, such as the bulk densities and the particle current.

4.3.1 Exact correlation equations

We begin then, by constructing the exact correlation equations for the bound and unbound lattices in the bulk. Again, our lattices are defined so that site 1 corresponds to the site furthest to the left, which is where the growth events are occurring (see Figure 4.1). The equations are constructed in the same way as in Subsection 3.1.2, by considering the change in the statistical average of the occupancy at lattice site i, due to the flow of particles into and out of that site.

Denoting the occupancy at site i on the unbound lattice σ_i, we have for the bound lattice:

$$\frac{d\langle\tau_i\rangle}{dt} = \langle\tau_{i+1}[1-\tau_i]\rangle - \langle\tau_i[1-\tau_{i-1}]\rangle + \gamma\langle\tau_1[\tau_{i-1}-\tau_i]\rangle + a\langle\sigma_i[1-\tau_i]\rangle - d\langle\tau_i[1-\sigma_i]\rangle \ . \quad (4.1)$$

The dynamics of the particles confined to this lattice are the same as those of the DEEP. The first three terms in the correlation equation for the bound lattice are thus identical to Equation 3.7. The last two terms describe the additional dynamics of loss and gain of particles due to the exchange occurring between bound and unbound lattices.

For the unbound lattice, we have:

$$\frac{d\langle\sigma_i\rangle}{dt} = D\langle\sigma_{i+1}+\sigma_{i-1}-2\sigma_i\rangle + \gamma\langle\tau_1[\sigma_{i-1}-\sigma_i]\rangle - a\langle\sigma_i[1-\tau_i]\rangle + d\langle\tau_i[1-\sigma_i]\rangle \ . \quad (4.2)$$

The first term describes the symmetric hopping dynamics. With rate D, particles enter from site $i-1$ and from site $i+1$. A factor 2 is present in the first loss term because particles depart site i to both sides. The final two terms are the same as the final two terms of Equation 4.1, but of opposite sign, describing the particle exchange between lattices.

4.3.2 Coupled mean-field equations

We found in Section 5.9 of the previous chapter, that a simple mean-field analysis provided an adequate framework for deriving the qualitative phase structure of the DEEP. Here again we shall appeal to this simple approximation in order to determine the effects arising from the additional motor attachment and detachment dynamics.

According to the simple mean-field approximation (3.14), we ignore all correlations, and factorise every term. Denoting $\langle\tau_i\rangle = \rho_i$ and $\langle\sigma_i\rangle = \sigma_i$, the dynamics of the bound and unbound lattices are given in this approximation by the following mean-field equations:

$$\frac{d\rho_i}{dt} = \rho_{i+1}[1-\rho_i] - \rho_i[1-\rho_{i-1}] + \gamma\rho_1[\rho_{i-1}-\rho_i] + a\sigma_i[1-\rho_i] - d\rho_i[1-\sigma_i] \ , \quad (4.3)$$

$$\frac{d\sigma_i}{dt} = D[\sigma_{i+1}-2\sigma_i+\sigma_{i-1}] + \gamma\rho_1[\sigma_{i-1}-\sigma_i] - a\sigma_i[1-\rho_i] + d\rho_i[1-\sigma_i] \ . \quad (4.4)$$

4.3.3 First order continuum approximation

We deal with the coupled mean-field equations (4.3–4.4) by considering a continuum approximation. In the continuum, the densities at the discrete sites i, become functions of a continuous variable, x, which denotes their position in the lattice. Taylor expanding about x, we can thus make the replacement,

$$\begin{aligned} \rho_i &= \rho(x) = \rho \ , \qquad (4.5) \\ \rho_{i+1} &= \rho(x+h) = \rho + h\rho' + \frac{h^2}{2}\rho'' + \ldots \ , \qquad (4.6) \\ \rho_{i-1} &= \rho(x-h) = \rho - h\rho' + \frac{h^2}{2}\rho'' + \ldots \ . \qquad (4.7) \end{aligned}$$

We begin with the simple first-order approximation, which ignores those terms of order h^2 and higher in the expansions above. In this scheme, Equations 4.3 and 4.4 become:

$$\frac{d\rho}{dt} = \frac{d\rho}{dx}[1-2\rho-v] + a\sigma(1-\rho) - d\rho(1-\sigma) \ , \qquad (4.8)$$

$$\frac{d\sigma}{dt} = -v\frac{d\sigma}{dx} - a\sigma(1-\rho) + d\rho(1-\sigma) \ , \qquad (4.9)$$

where we have arbitrarily set $h = 1$ and used $\gamma\rho_1 = v$. Note that in this approximation the diffusion coefficient drops out.

We are interested in the properties of a steady state, i.e. when the particle densities on both the bound and unbound lattices are stationary in time:

$$\frac{d\rho}{dt} = 0 \ , \quad \frac{d\sigma}{dt} = 0 \ . \qquad (4.10)$$

We may thus add Equations 4.3 and 4.4 in the steady state, to obtain:

$$\frac{d}{dx}[\rho(1-\rho) - v(\rho+\sigma)] = 0 \ . \qquad (4.11)$$

This expression is a continuity equation, describing the conservation of mass in the system. The expression in the square brackets is thus the total current, J, of particles flowing from right to left, through both bound and unbound lattices:

$$J_{\rho+\sigma} = \rho(1-\rho) - v(\rho+\sigma) \ . \qquad (4.12)$$

Note the similarity between this expression and the current–density relation of the DEEP (Equation 3.16). The contribution to the total current due to particles on the unbound lattice arises solely from the displacement of the reference frame, which gives a backwards current proportional to the velocity of the lattice growth v. The current due to the hopping dynamics on the unbound lattice equates to zero due to the symmetry of the hops.

4.3.4 Steady state current and tip velocity

Now assume that a steady state for (4.8) and (4.9) exists, where the total current everywhere is equal. Since the current of particles across the boundary of site 1 is equal to the velocity of the tip v, we have from (4.12):

$$J = \frac{\rho(1-\rho)}{1+\rho+\sigma} \ . \tag{4.13}$$

If we assume that in this steady state, there exists a local equilibrium between the bound and unbound lattices,

$$a\sigma(1-\rho) = d\rho(1-\sigma) \ , \tag{4.14}$$

then we have the following constraint on the unbound density:

$$\sigma = \frac{\epsilon\rho}{1-(1-\epsilon)\rho} \ , \tag{4.15}$$

where $\epsilon = \frac{d}{a}$. Substituting this into (4.13), we find J in terms of only ρ and ϵ:

$$J = \frac{\rho(1-\rho)}{1+\rho+\frac{\epsilon\rho}{1-(1-\epsilon)\rho}} \ . \tag{4.16}$$

One can rearrange (4.16), to find a cubic in ρ:

$$\rho^3 + \rho^2[J - 1 - \frac{1}{1-\epsilon}] + \rho\frac{1-2\epsilon J}{1-\epsilon} - \frac{J}{1-\epsilon} = 0 \ . \tag{4.17}$$

That the current, J, is cubic in ρ, tells us that for any J and ϵ, there are three solutions for ρ while local equilibrium between bound and unbound lattices holds.

Far from the tip, particles enter the bound lattice with rate α. One might expect that a steady state will exist that is limited by a low rate of input, as it did in the case of the DEEP with no attachment and detachment dynamics. In this case, one of the roots of 4.17 is

$$\rho = \alpha \ , \tag{4.18}$$

with the other two given by:

$$\rho = \frac{1-\alpha-J+\frac{1}{1-\epsilon}}{2} + \frac{\sqrt{(1-\alpha-J+\frac{1}{1-\epsilon})^2 - \frac{4J(1-\epsilon)}{\alpha}}}{2} \ , \tag{4.19}$$

$$\rho = 1-\alpha-J+\frac{1}{1-\epsilon} - \rho_1 \ . \tag{4.20}$$

4.3.5 The solution structure

To determine the solution structure of the steady states, we consider again Equation 4.8. Assuming the conditions for a steady state, where the current is equal everywhere and equal to the tip velocity, we may rearrange (4.13) to find an expression for σ in terms of

ρ and v:

$$\sigma = \frac{\rho(1-\rho) - v(1+\rho)}{v} \ . \tag{4.21}$$

Using this, we can eliminate σ from Equation 4.8, giving finally:

$$\frac{d\rho}{dx} 2[\rho - \frac{(1-v)}{2}] = \frac{1}{v}[(a-d)\rho^3 - (2a - va - d(1-v))\rho^2 + (a - 2dv)\rho - v] \ , \tag{4.22}$$

which is satisfied everywhere in the bulk. Finding the exact solution to Equation 4.22 is not our aim here. We are able, however, to make some progress by analysing the solution structure qualitatively. We first rewrite (4.22) as follows:

$$\frac{d\rho}{dx} = \frac{a(1-\epsilon)}{v(2\rho - 1 + v)}[\rho^3 - (1 - v + \frac{1}{1-\epsilon})\rho^2 + \frac{1-2\epsilon v}{1-\epsilon}\rho - \frac{v}{1-\epsilon}] \ , \tag{4.23}$$

where again $\epsilon = \frac{d}{a}$. Note that this approach has led us to the same cubic on the right-hand side of (4.23) as was obtained in the previous subsection (Equation 4.17), so that at the roots, we know that local equilibrium holds and that J_ρ and J_σ are both constant.

It is convenient at this point, to define the asymptote of (4.23):

$$\rho_a = \frac{1-v}{2} \ . \tag{4.24}$$

We define the three roots to the cubic on the right-hand side of (4.23); ρ_1, ρ_2 and ρ_3, and we can now express (4.23) in a clearer form, as follows:

$$\frac{d\rho}{dx} = \frac{a(1-\epsilon)}{2v}\frac{1}{[\rho - \rho_a]}[\rho - \rho_1][\rho - \rho_2][\rho - \rho_3] \ . \tag{4.25}$$

One can see from (4.25) that the value of ρ relative to these roots and ρ_a determines the gradient of the local change in density, allowing us to construct the density profile solution structure. What remains is to find expressions for the roots and the asymptote in terms of the model parameters, and to determine their ordering. The sign of the gradient also clearly depends on the value of ϵ.

We begin by finding the general expressions for the roots. We expand (4.25):

$$\frac{d\rho}{dx} = \frac{a(1-\epsilon)}{2v}\frac{1}{[\rho - \rho_a]}[\rho^3 - (\rho_1 + \rho_2 + \rho_3)\rho^2 + (\rho_1\rho_2 + \rho_2\rho_3 + \rho_3\rho_1)\rho - \rho_1\rho_2\rho_3] \ , \tag{4.26}$$

and equate the above coefficients with those in Equation 4.23, to obtain the following:

$$v = (1-\epsilon)\rho_1\rho_2\rho_3 \ , \tag{4.27}$$

$$1 - v + \frac{1}{1-\epsilon} = (\rho_1 + \rho_2 + \rho_3) \ , \tag{4.28}$$

$$\frac{1-2\epsilon v}{1-\epsilon} = (\rho_1\rho_2 + \rho_2\rho_3 + \rho_3\rho_1) \ . \tag{4.29}$$

Equations 4.27–4.29 are symmetric under the interchange of the three roots. We may therefore arbitrarily choose,

$$\rho_1 > \rho_2 > \rho_3 \; . \tag{4.30}$$

4.3.6 The limit $\epsilon \to 0$

As an illustrative example, let us start in the simplest limit, of $\epsilon = \frac{d}{a} \to 0$. This corresponds to the case of no attachment or detachment, i.e. $d = 0, a = 0$, though we argue that the basic solution structure implied by (4.25) in this limit will remain for arbitrary $\epsilon < 1$. In the limit of no detachment, the unbound density $\sigma \to 0$ and we have from (4.13),

$$v = \frac{\rho(1-\rho)}{1+\rho} \; . \tag{4.31}$$

Now let us assume that one of the roots of (4.25) corresponds to the far boundary condition, where particles are injected with rate α:

$$\rho_3 = \rho_N = \alpha \; . \tag{4.32}$$

It follows that the tip velocity (4.31) is given by:

$$v = \frac{\alpha(1-\alpha)}{1+\alpha} \tag{4.33}$$

We thus obtain from (4.33), (4.27) and (4.28):

$$\frac{\alpha(1-\alpha)}{1+\alpha} = \alpha\rho_1\rho_2 = 2 - \alpha - \rho_1 - \rho_2 \; . \tag{4.34}$$

This can be solved to give us roots ρ_1 and ρ_2:

$$\rho_1 = 1 \; , \tag{4.35}$$

$$\rho_2 = \frac{1-\alpha}{1+\alpha} \; . \tag{4.36}$$

The asymptote, ρ_a, follows from its definition (4.24) with (4.33):

$$\rho_a = \frac{1+\alpha^2}{2(1+\alpha)} \; . \tag{4.37}$$

The roots α and ρ_2 and asymptote ρ_a are plotted against α in Figure 4.2. One can see that in this range they are all between zero and 1, and that they collapse to a single value for $\alpha = \sqrt{2} - 1$. This value for α corresponds to the point at which, given (4.33), the solution for ρ of (4.31) becomes imaginary, i.e. $(1-v)^2 = 4v$.

In Figure 4.3 we deduce from (4.25), the solution curves for $\alpha < \sqrt{2} - 1$, with

$$\rho_1 > \rho_2 > \rho_a > \alpha > 0 \; . \tag{4.38}$$

This simple approximation provides a preliminary guide to the sorts of behaviour one

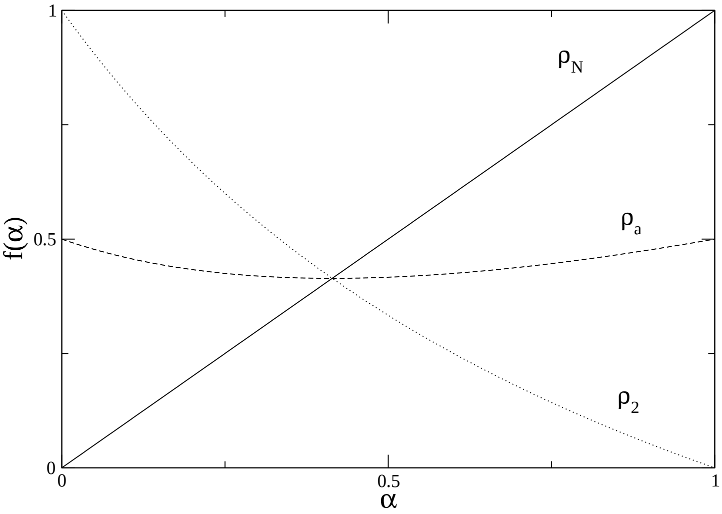

Figure 4.2: Roots ρ_N and ρ_2, and asymptote of Equation 4.25 in the limit $\epsilon = 0$, plotted against α. All three converge at $\alpha = \sqrt{2} - 1$. For $\alpha < \sqrt{2} - 1$, the order, in magnitude, of the functions are $\rho_1 > \rho_2 > \rho_a > \alpha$.

might expect to observe in our system. We already see the emergence of a solution space with a more interesting structure than the case where we include no attachment and detachment terms in the equations. Now there are two attractors, $\rho_2 = \frac{1-\alpha}{1+\alpha}$ and $\rho_\alpha = \alpha$. This second attractor in principle can give rise to stationary shocks in any region of the parameter space where the solution converges to ρ_2, since from here the current on both the bound lattice (and the unbound lattice) is continuous across a discontinuous shift in density to the other stable solution, where it meets the boundary condition $\rho_N = \alpha$. Such shock solutions are illustrated schematically in Figure 4.4. Previously this type of solution was only possible if the density at the tip was exactly equal to the upper fixed point of the recursion relation (3.16). The extra degrees of freedom introduced by the exchange of particles between lattices allows the stationary shock region of the DEEP phase diagram to be expanded from a single line in the α–γ phase space to a larger region in which stationary shocks are in possible.

4.3.7 The case $\epsilon > 1$

For a general picture of the behaviour of this coupled system, we also consider the case when the detachment rate exceeds the attachment rate, i.e. $\epsilon > 1$. From (4.27), we see that now at least one of the roots must be negative. There are two possibilities; either

$$\rho_3 < 0 \ , \quad \rho_2 \ , \rho_1 > 0 \ ,$$

or

$$\rho_3 \ , \rho_2 \ , \rho_1 \ < 0 \ .$$

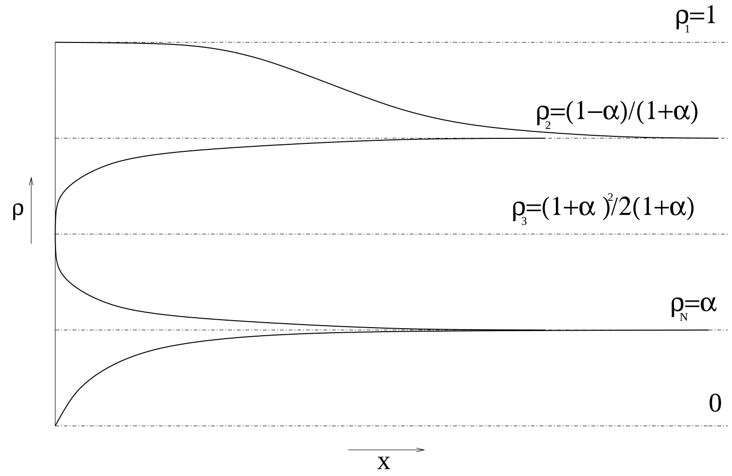

Figure 4.3: Schematic solution curves for the density. The density gradient converges to zero as $\rho \to \rho_1$, ρ_2 and ρ_N. As $\rho \to \rho_3$, the gradient tends to ∞. The density gradient is positive in regions $\rho_3 < \rho < \rho_2$ and $0 < \rho < \alpha$, and negative in regions $\alpha < \rho < \rho_3$ and $\rho_2 < \rho < 1$, resulting in two stable fixed points: ρ_2 and α.

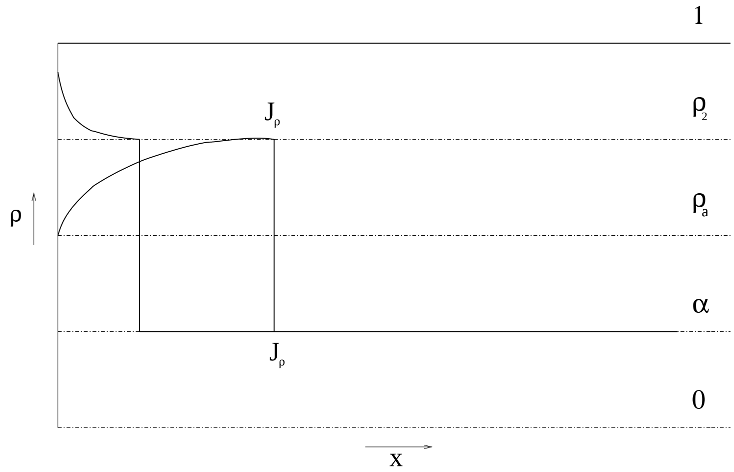

Figure 4.4: Schematic shock solutions of the bound density, for the case $\epsilon < 1$. The density converges on the upper stable fixed point, then jumps discontinuously to the lower fixed point, meeting the far boundary condition. The shock is stable since the current J_ρ is equal either side of it.

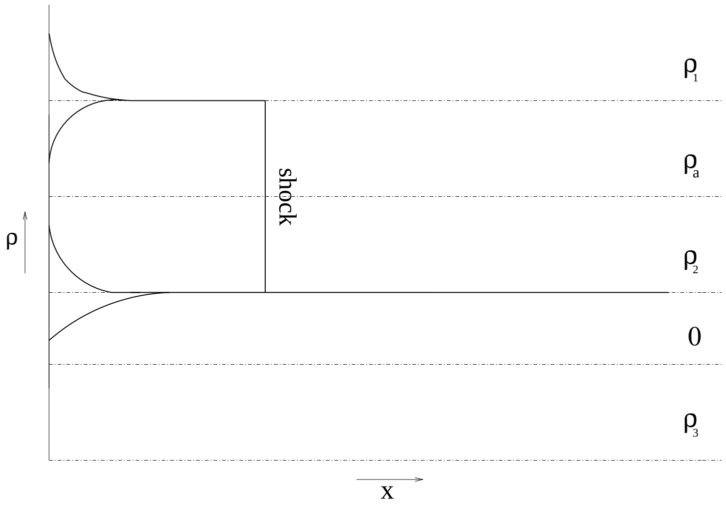

Figure 4.5: Schematic solutions for the case $\epsilon > 1$. Low density solutions are present, where the density converges to α, meeting the boundary condition at the input. Shock solutions are also possible, where the density converges on the upper stable fixed point, then jumps discontinuously to α.

For a physically relevant solution, we choose the former condition. Now since the maximum velocity (from 4.13) is less than 1, we know from (4.24), that the asymptote of (4.25) (ρ_a) must be greater than zero. We choose

$$\rho_1 > \rho_a > \rho_2 > 0 > \rho_3 \ .$$

This results in an unstable asymptote, which is physical. The schematic solution curves are illustrated for this case, in Figure 4.5.

4.3.8 Numerical mean-field solutions

The mean-field solutions can be illustrated by numerically iterating the mean-field equations (4.3) and (4.4). We iterate two arrays of double precision real numbers between zero and one, which represent ρ_i and σ_i. The iterations are carried out according to the update equations:

$$\begin{aligned}\rho_i(t+\Delta t) &= \rho_i(t) \\ &+ \Delta t(\rho_{i+1}[1-\rho_i] - \rho_i[1-\rho_{i-1}] + \gamma\rho_1[\rho_{i-1}-\rho_i] + a\sigma_i[1-\rho_i] - d\rho_i[1-\sigma_i]) \ ,\end{aligned}$$

$$\begin{aligned}\sigma_i(t+\Delta t) &= \sigma_i(t) \\ &+ \Delta t(D[\sigma_{i+1} - 2\sigma_i + \sigma_{i-1}] + \gamma\rho_1[\sigma_{i-1}-\sigma_i] - a\sigma_i[1-\rho_i] + d\rho_i[1-\sigma_i]) \ ,\end{aligned}$$

where with each update two new arrays are created from, and then replace, the previous two. The system is initialised as an array of random densities, and then allowed to evolve towards a steady state.

As in the numerical computation of the mean-field theory in Subsection 3.2.4, this approach does not respect the moving boundary condition of our system, as it is carried out on an array of fixed length. This imposes an artificial boundary at site N, and some of the results may exhibit artifacts of the restricted system size.

A representative set of density profiles obtained numerically are illustrated in Figure 4.6. One can identify some of the solutions which were predicted above. In the first panel, we see that for low α, the system is in a low density phase, similar to the low density phase of the DEEP. The bound density is equal to α in the bulk, with a small decay at the tip, caused by the boundary condition there. In the next two panels we see behaviour distinct from that seen in the DEEP with no attachment and detachment. The second panel shows a stationary shock, where the density appears to converge from the tip, toward a high density plateau, before discontinuously jumping to meet the boundary condition α. This is in contrast to the mean-field results of the simple DEEP, which only exhibit shock solutions when the density at the tip is exactly equal to the upper root of the recursion relation (Equation 3.16), and the high density region is therefore completely flat from the tip to the shock. The third panel also illustrates a convergence toward a high density plateau, though in this case the shock has been driven to the right boundary and the density profile thus appears to be in a high density phase. The final panel is in the regime of high α and high γ. The resulting density profile is similar to the maximal current profiles of the previous chapter. The density decays from both boundaries, and the growing system does not reach a steady state.

The parameter space of this model is rather large. A broad understanding of the effect of the parameters on the macroscopic model behaviour can be achieved by varying each parameter individually from a set of 'control' values, and observing the changes in the resulting density profiles. The control parameter values were chosen to lie in a region where shocks were observed, namely: $\alpha = 0.15$, $\gamma = 0.1$, $a = 0.0001$, $d = 0.0005$, $D = 0.5$, $N = 200$. The effects of the variation of individual parameters can be seen in Figure 4.7, and are outlined below:

Input rate α An increase in α results in the shock on the bound lattice moving to the right. The bound density to the right of the shock increases to meet the new boundary condition far from the tip (α). The unbound density increases correspondingly. The tip densities on both lattices remain unchanged.

Growth rate γ Increasing γ results in the shock position moving towards the tip. Far from the boundary the densities are unaffected. The height of the density plateaus next to the tip is reduced on both lattices.

Attachment rate a As attachment rate increases, the shock moves to the right. The density on the unbound lattice to the left and right of the shock is decreased. The density

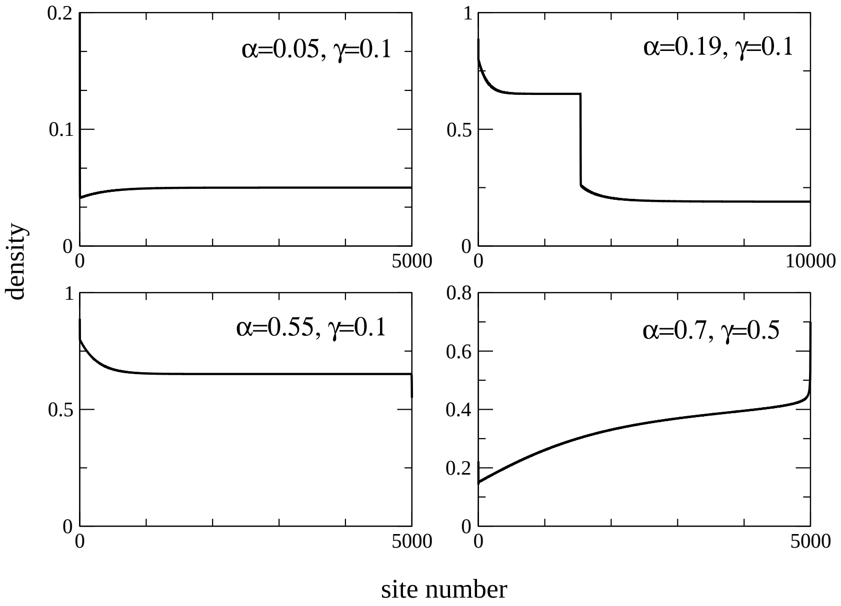

Figure 4.6: Density profiles on the bound lattice, generated by iterating the mean-field equation (4.3). Four distinct behaviours can be seen (discussed in the text), as the parameters α and γ are varied.

on the bound lattice is still fixed at α to the right of the shock, but is increased to the left.

Detachment rate d Converse to increased attachment rate, as detachment rate increases, the shock moves towards the tip. Unbound density is increased and bound density is decreased to the left of the shock.

Diffusion rate D The diffusion constant controls the efficiency with which changes in density are propagated through the unbound lattice. A high diffusion constant results in a smoother variation of the density on both lattices, though the effect is slight.

Note that in general, away from the boundary and the shock regions, the density profiles are flat. It is clear from Equations 4.3 and 4.4 that in these regions the local equilibrium condition (4.14) is satisfied.

4.4 Monte Carlo simulation

Using Monte Carlo simulations[1], we now explore the exact dynamics of the model, to determine whether the new behaviour predicted by the simple mean-field continuum approximation of Section 4.3 manifests itself in a fully simulated system.

The algorithm we employ is similar to that described in Subsection 3.6.1, only now

---

[1] This work made use of the resources provided by the Edinburgh Compute and Data Facility (ECDF). (http://www.ecdf.ed.ac.uk/). The ECDF is partially supported by the eDIKT initiative (http://www.edikt.org.uk)

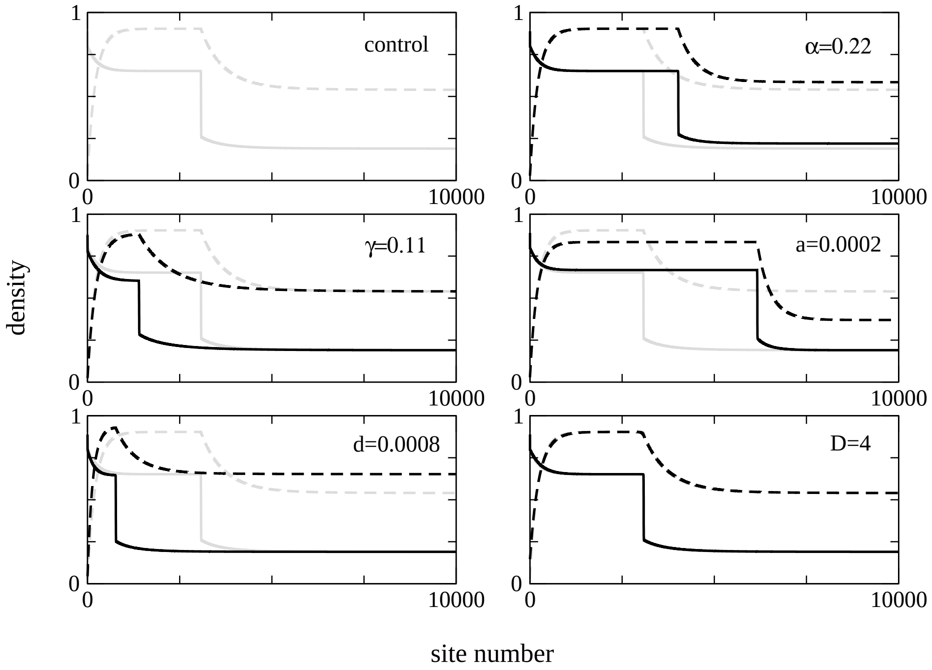

Figure 4.7: The effect of varying different parameters on the macroscopic behaviour of the mean-field equations. The first panel shows the 'control' profiles, with parameters: $\alpha = 0.19$, $\gamma = 0.1$, $\beta = 0.0$, $a = 0.0001$, $d = 0.0005$, $D = 0.5$. In the panels that follow, the parameter being varied is indicated. The bound lattice densities (solid lines) and the unbound densities (dashed lines) are shown in grey for the control profiles, and black for the varied profiles.

extended to include a second Boolean array, which represents the unbound particles[2]. Each Monte Carlo time step now consists of $2N$ stochastic update attempts, carried out at sites chosen at random from either one of the two lattices. Again, the probabilities for the updates of this algorithm are normalised to the greatest escape rate from any given configuration, for example an unbound particle with no neighbours and no particle on the reciprocal bound lattice may carry out one of three possible updates: a forward hop (rate D), a backward hop (rate D), or an attachment to the bound lattice (rate a). If the sum of these rates exceeds the sum of the rates out of any other configuration then all rates for the simulation are normalised by $2D + a$. See e.g. Equations 3.90–3.94.

The boundary conditions, which were not explicitly defined in the analysis above, are chosen such that attachment and detachment occurs at any site, including the tip and the site at the far boundary, while injection and growth events occur on the bound lattice only.

4.4.1 Tip velocity

We begin by looking at the growth velocity. In Subsection 3.6.3, we saw that a change in the functional form of the growth velocity was an indication of a phase transition. In Section 4.3, it was predicted that for small values of α, a low density phase will exist, as illustrated in the first panel of Figure 4.6. In the case of a low density phase, we can find the tip velocity as simple relation depending only on α and ϵ, from Equation 4.16:

$$v = \frac{\alpha(1-\alpha)}{1+\alpha+\frac{\epsilon\alpha}{1-(1-\epsilon)\alpha}} \,. \tag{4.39}$$

Figure 4.8 compares the predicted velocity to Monte Carlo results. The velocity of the simulated lattice agrees very closely with the theory, and it is clear that a phase change takes place at $\alpha \approx 0.16$. Beyond this point, the velocity is no longer dependent on α and stays constant (aside from statistical fluctuations), with a value that appears to coincide closely to the high density velocity in the case of no attachment and detachment,

$$v_{hd} = \frac{\gamma(1-\gamma)}{1+\gamma} \,. \tag{4.40}$$

In Figure 4.9, we look more closely at the effect of attachment and detachment rates and their ratio, on the position of the phase transition, and on the value of the high density velocity. One can see that despite the high density velocity appearing to be very close in value to (4.40) for low values of a and d, there is nonetheless a weak dependence of the velocity on attachment and detachment rates. For high rates of attachment and detachment the high density velocity is reduced from the case of zero attachment and detachment, while for rates of attachment and detachment approximately one order of magnitude smaller, the effect on the high density velocity appears negligible. Before the

---

[2] A continuous time algorithm (Subsection 2.1.4) was also implemented, however, it was found to have a longer running time than its discrete time counterpart.

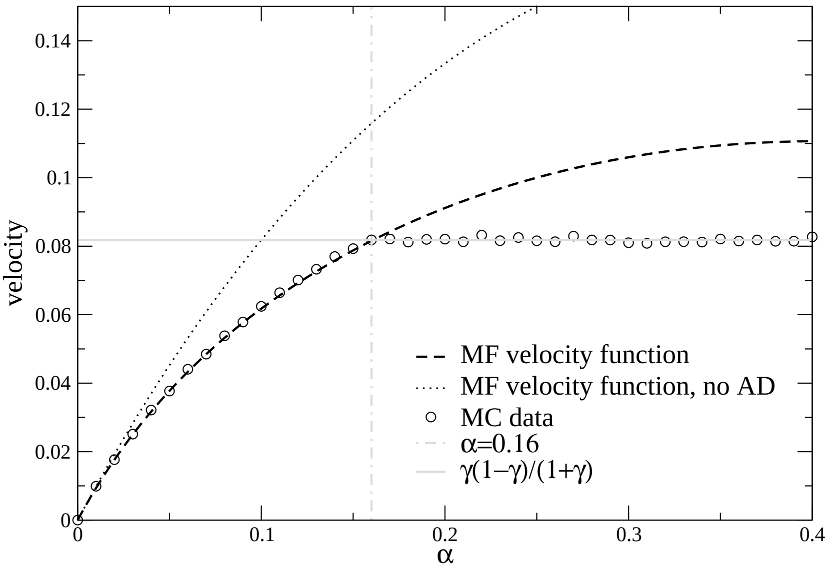

Figure 4.8: A plot of the tip velocity measured from Monte Carlo simulations, for varying α. The plot clearly illustrates the phase transition at $\alpha \approx 0.16$, where the functional form of the velocity becomes independent of α. The parameter values for the simulation are a=0.0001, d=0.0005, gamma=0.1. Mean-field theoretical velocities are also shown for these parameters and for the case of no attachment or detachment, for comparison. One can see that the velocity after the phase transition agrees closely with the high density velocity predicted by the refined mean-field theory, with no attachment and attachment.

phase transition, there is an evident dependence on ϵ, with large ϵ resulting in a reduced velocity. After the phase transition, the dependence on ϵ is less apparent. For $\epsilon < 1$, the effect on the low density velocity is rather small.

4.4.2 Monte Carlo density profiles

Density profiles generated from Monte Carlo simulation, with various values of α are shown in Figure 4.10, illustrating some of the phases present in this system. The first panel shows a low density phase where the density is equal to α in the bulk. The second panel shows what appears to be a shock close to the left boundary. As α is increased, we see in the third panel, a clear shock which coincides with the theoretical shock solutions illustrated in Figure 4.3. The fourth panel also exhibits a shock, however the non-localised position of the discontinuity suggests that in this case the shock is not stationary with respect to the tip. This profile is probably in a phase analogous to the *dynamic shock phase* discussed in the previous Chapter, where the shock is travelling forward, but with a velocity less than the tip velocity. The penultimate panel shows profiles in the high density phase, when α is large. Here the bulk bound density converges from the tip, to a constant high density which extends to the far boundary (not shown in the Figure). In the final panel, both α and γ are high, and the density profiles appear analogous to the maximal current phase

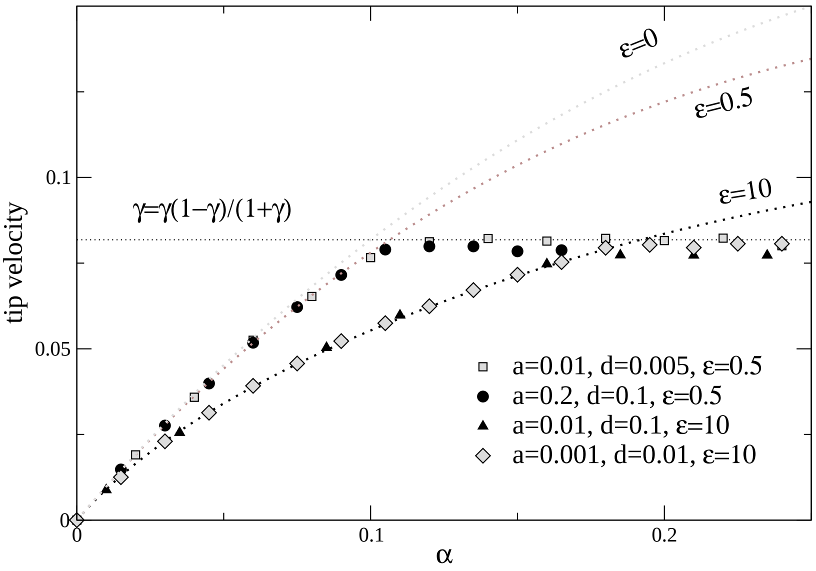

Figure 4.9: An illustration of the dependence of velocity on rates of attachment and detachment, and on their ratio, ϵ. The mean-field low density velocity function (4.39) is shown for different ϵ (bold dotted lines). Solid lines show the results from Monte Carlo simulation. It is evident that while the low density velocity is dependent on the ratio of a and d (ϵ), the high density velocity is more strongly dependent on the magnitudes of a and d. Low a and d result in a high density velocity close to that for zero attachment and detachment ($\gamma(1-\gamma)/(1+\gamma)$), irrespective of ϵ.

of the previous Chapter.

The Monte Carlo results are presented again in Figure 4.12, alongside the mean-field results for the same parameters. The comparison between theory and simulation is illustrated over the first 500 sites. This means that although the Monte Carlo results are gathered from a simulation of the whole system, the mean-field results are calculated on a system of fixed size 500 (1000 for the final panel). The effects of the finite system size can be seen in the position of the shock in panels two, three and four. However, the general trends in behaviour of the profiles appear to be fairly well predicted by the mean-field theory. The profiles in the penultimate panel in particular are in rather close agreement with the mean-field results.

In Figure 4.11, we examine in some detail one of the shock profiles. This density profile was obtained by running a full simulation, using the parameters $\alpha = 0.175$, $\gamma = 0.1$, $d = 0.005$, $a = 0.001$, $D = 0.5$. The system was first allowed to relax for 500000 time steps. Over the next 100000 time steps, the occupancy at sites near the tip were counted and averaged. The result is the exact particle density distribution in the region close to the tip. This choice of parameters puts our realisation into the regime of $\epsilon > 1$. We thus compare it with the theoretical predictions of Subsection 4.3.7. One can see that on the right, the density matches the input boundary condition α. A clear shock appears between this density and high density plateau. The high density plateau at the left of the shock corresponds to the upper stable root ρ_1. The upper stable root can be calculated for these parameters using Equations 4.39 and 4.19. The theoretical upper root and the lower root α are indicated with dotted lines in Figure 4.11. One can see that the high density plateau to the left of the shock is rather close to the theoretical result, though slightly below. The discrepancy may be an artifact of the approximation scheme (4.3–4.9), or it could indicate that the shock in the particular case illustrated is not in fact truly stationary with respect to the tip. In the latter scenario, the current in the region to the left of the shock is not equal to the current in the region to the right of the shock, and the difference in current is balanced with a moving shock (the velocity of the shock given, as before, by Equation 2.6). The velocity relation (4.39) therefore does not hold, and cannot be used to calculate the correct roots. Note that if one inserts the velocity measured from simulation into Equation 4.23, and solve for $\frac{d\rho}{dx} = 0$, the correct upper root is obtained, while it is apparent that the lower root lies beneath α. These results are indicated on Figure 4.11 with dashed lines.

4.5 Summary, discussion and open questions

To summarise; in this chapter, we have seen the introduction of a more involved model for fungal hyphal tip growth, developed from the DEEP model of Chapter 3. In addition to the dynamics of the DEEP, this new model accounts for the stochastic exchange of particles between a confining microtubule track, and the surrounding cytoplasm. The extended model more closely resembles the true dynamics of particles involved in the

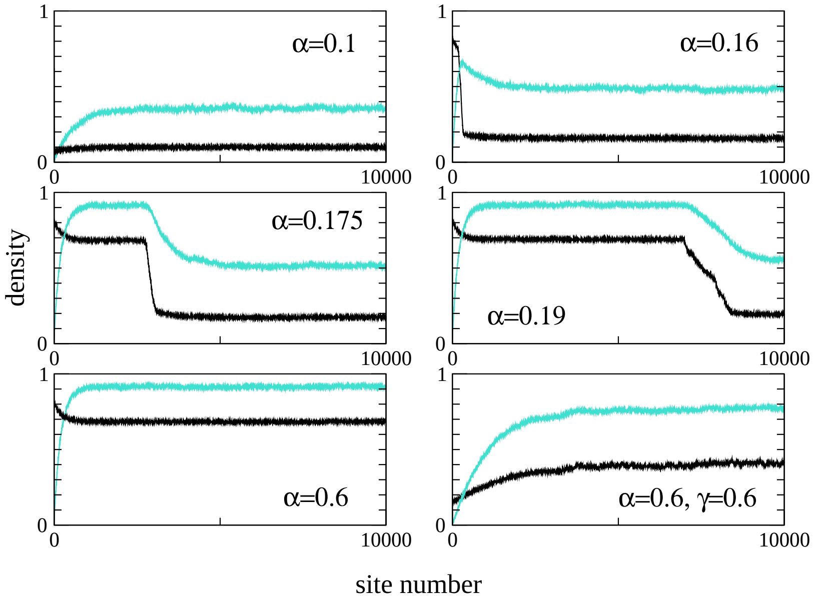

Figure 4.10: Density profiles generated from Monte Carlo simulations, showing the different phase behaviours. The parameters used were $\gamma = 0.1$, $a = 0.0001$, $d = 0.0005$, ($\epsilon = 5$). The first panel shows a low density phase. In the second panel, a shock has appeared, close to the tip boundary. The third panel shows what appears to be shock which is stationary and removed from the tip. In the fourth panel, the shock is no longer localised and is instead smeared out over several hundred sites. This is an indication that the shock is no longer stationary in the reference frame of the tip. The smearing of the shock is an artifact of our averaging procedure. The bottom left panel shows a high density phase, and the final panel shows a maximal current phase.

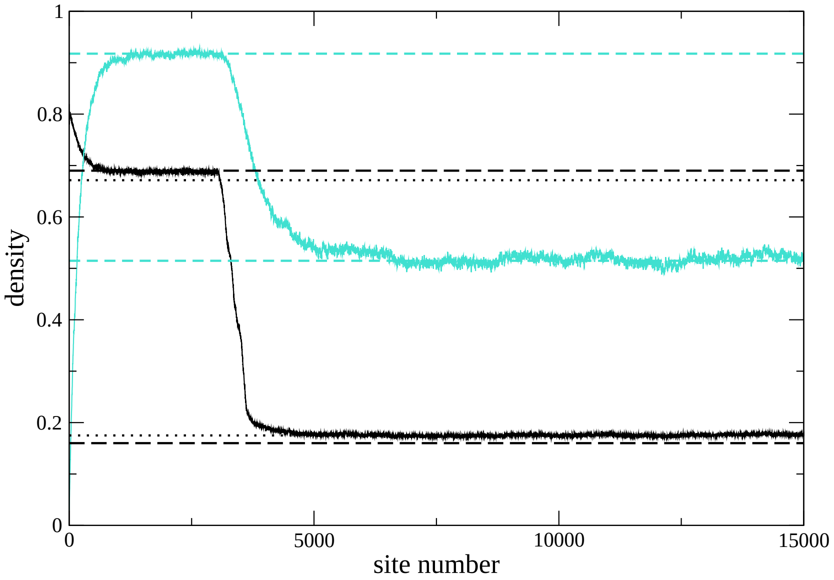

Figure 4.11: Density profiles exhibiting an approximately stationary shock, between a high density plateau at the tip, and a low density bulk which meets the boundary condition α. The solid lines show bound (black) and unbound (turquoise) densities obtained from Monte Carlo simulation. Various theoretical results are also indicated. The black dotted lines indicate the roots calculated from (4.19), with the velocity given by Equation 4.39. The black dashed lines show the roots calculated directly from (4.23), using the high density velocity from simulation (given to an accurate approximation by Equation 4.40). Turquoise dashed lines indicate the equilibrium unbound density calculated from the Monte Carlo results and Equation 4.15.

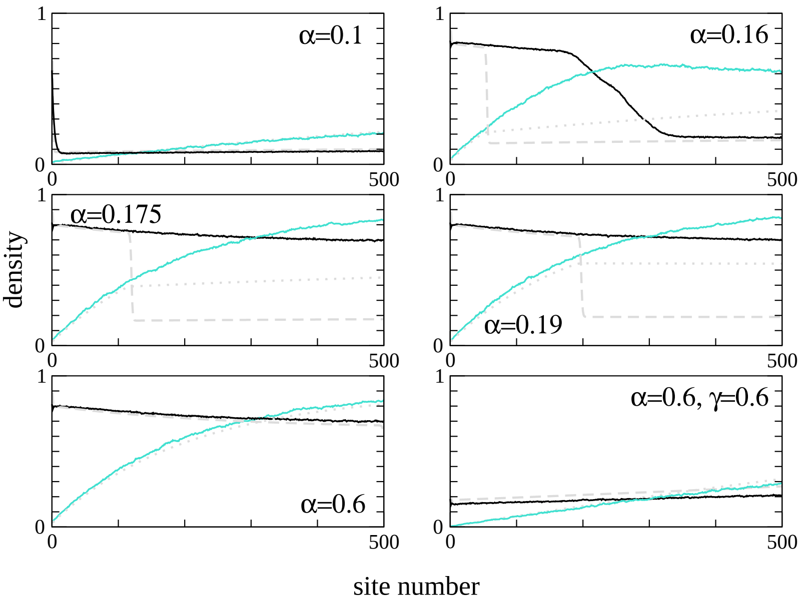

Figure 4.12: A comparison of the Monte Carlo results of Figure 4.10 (solid lines) with mean-field density profiles (dashed lines) for the first 500 sites of the lattice. The general trend of the profiles are predicted with some accuracy, however artifacts of the confined system size of the mean-field results, such as the position of the discontinuity, can be seen.

molecular motor transport processes within a fungal hypha, where motors only spend finite periods bound to the microtubule and the rest of the time diffusing, unbound, in their surroundings.

The unbound motors are incorporated into the model by coupling the DEEP to a second one-dimensional lattice, which represents the cytoplasm. On the 'unbound' lattice, particles hop in either direction, since in the cytoplasm motors undergo unbiased diffusion. We assume this to be a mean-field description of the unbound motors. That is to say that although in reality the motors diffuse through a 3-dimensional space, we can model the motors using a one dimensional lattice, where the density at each site on the lattice represents the average density across the breadth of the cytoplasm, at that longitudinal point along the hypha.

One might argue that a more biologically relevant picture is one which assumes a reservoir of unbound particles, such as was done by [Parmeggiani 03] in their study inspired by cellular transport phenomena. Indeed, since the cytoplasm is large compared to the microtubules, and the unbound motors out-number the bound motors, one might expect that traffic phenomena is not important off the microtubule, and that the unbound motors in the cytoplasm can be adequately represented by a reservoir. Interestingly however, we find that both our approach and that of [Parmeggiani 03] result in a similar phenomenon; that of shocks arising in the density profiles. This suggests that the significant dynamics of these coupled models are those of the motor *exchange* between lattices, rather than the distribution and dynamics of the unbound particles. Indeed, if one increases the diffusion constant of the unbound particles of our model (Figure 4.7), we do not see a qualitative change in the density profile on the bound lattice.

The steady state behaviour of our extended model is studied in continuous space, with a first order mean-field approximation. Despite the simplicity of the approximation, we are able to identify the qualitative steady state behaviours, including some behaviour which is distinct from the simple DEEP with no attachment or detachment. The theoretical results are confirmed by Monte Carlo simulation in Section 4.4. The phases present are not dissimilar to those of the simple DEEP. One sees phases resembling the high density, low density, maximal current, and shock solutions of the DEEP. There are however differences in the details of the profiles. Previously, high density and shock solutions existed only when the density at the tip was exactly equal to the upper root of Equation 3.16. Profiles were thus flat from the tip to the shock, and the shock was stationary only on the transition line between the low density and dynamic shock phases. With the introduction of attachment and detachment dynamics, the high density phase exhibits a smooth convergence of the bound density from the tip to a high plateau (the height of which is controlled by γ). The significance result is a widening of the region where stationary shocks may occur. For whole ranges of α and γ, a convergence to a high plateau is now apparently possible, with the position and dynamics of the shock controlled by the attachment and detachment rates.

The particulars of the phase diagram for this model are not discussed in this chapter, though it should be a straight-forward matter to apply the same principles of Section 3.2 here, in order to arrive at the mean-field phase boundaries. Our analysis has been, rather, to focus on the qualitative changes brought about with the additional dynamics of attachment and detachment. A number of open questions remain. For example, the particular dynamics of the shock with respect to the large parameter space of this model are yet to be characterised. It would be of interest to deduce in which regions the shock becomes localised and how the parameters control the size, position and dynamics of the shock. Another open question is whether the shock remains localised in the large time limit. In [Parmeggiani 03] and [Evans 03] it is found that the stationary shocks only exist in the system when the rates of attachment and detachment scale appropriately with system size. For fixed values of attachment and detachment, the shock phenomenon thus disappears as the size of the system is increased. The pertinent question here is: does the shock behaviour we have observed in our growing system have a dependence on the system size?

The presence of a range of shock solutions clearly has some interesting consequences biologically. This phenomenon, for example, provides a mechanism by which an arbitrarily large area of high density could form directly behind the growing tip of a fungal hypha. Whereas in the DEEP with no attachment and detachment, the stationary shock solution could only exist for finely tuned parameters (i.e. on the transition between the low density and dynamic shock phase); the extra degrees of freedom afforded by the presence of an exchange between the cytoplasm and microtubule provides a shock stabilisation mechanism, allowing a stable shock to form across a range of values of α and γ. It would be of interest to determine, e.g. through further Monte Carlo simulation, the robustness of the shock solutions to variations in the parameters and in the large time limit, and thus to ultimately address the applicability of this model in the petri dish.

Chapter 5

Microtubule Instabilities

The final topic to be addressed in this thesis, is the phenomenon of microtubule instabilities, as introduced and discussed in some detail in Chapter 2. As with the problem of fungal hyphal tip growth, we are again considering a system which is changing in size as a result of some internal dynamics of the constituent parts. Rather than processive motors, the dynamic parts in this problem are the building blocks of the microtubule itself.

In this Chapter we illustrate the progress that can be made with a simple mean-field approach based on that which we have developed in earlier chapters. We study the idealised GTP-cap model of [Antal 07a] (Subsection 2.3.4), with the aim of deducing information about the phase transition within the general parameter space of the model.

5.1 A mean field approach

Let us first reformulate the GTP-cap model of [Antal 07a] in a manner similar to the particle–lattice based models of the previous two Chapters. To recap, the model describes the growth and decay of a single microtubule as the result of the interplay of its constituent parts: the GTP and GDP dimers (2.9–2.12). For our analysis, we represent the microtubule with a one dimensional lattice, and the GTP dimers by particles. The GDP dimers are then simply the empty lattice sites. Rather than hopping along the lattice, the particles in this model can only carry out a hydrolysis transition, i.e. particles can be lost from any site of the lattice with rate 1. The rest of the model dynamics occurs exclusively at the lattice end. Here, a new occupied site can be added with rate λ (if the site next to the end is occupied), or with rate $p\lambda$ (if the site next to the end is unoccupied); and an empty site can be lost with rate μ.

Again, we identify the dynamic end of the microtubule with site 1 of the lattice, and we make our analysis in the reference frame of this site. Within this framework, the model transitions are illustrated schematically in Figure 5.1.

5.1.1 Exact steady-state equations

We now consider the GTP 'density' at site i on the lattice, given by the statistically averaged occupancy at that site, which we denote $\langle\tau_i\rangle$. By considering the change with time of the occupancy at a given site, we may construct the exact steady-state equations

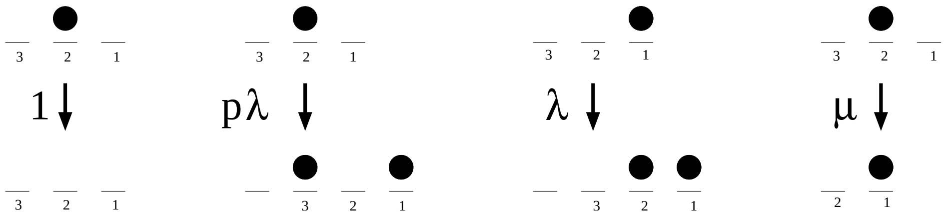

Figure 5.1: Schematic of the microtubule dynamics mapped onto a one dimensional lattice. Particles (filled circles) represent GTP and empty lattice sites represent GDP.

in the reference frame of site 1. For any site i, in the bulk of the lattice, we have:

$$\frac{d\langle\tau_i\rangle}{dt} = \lambda\langle\tau_1[\tau_{i-1}-\tau_i]\rangle + \langle[1-\tau_1]p\lambda[\tau_{i-1}-\tau_i]\rangle + \langle[1-\tau_1]\mu[\tau_{i+1}-\tau_i]\rangle - \langle\tau_i\rangle = 0\ . \quad (5.1)$$

The first two terms describe growth events. When the lattice increases in size, all site labels are updated $i \to i+1$ in order to have the new site labelled as site 1. As a result, a particle previously in site $i-1$ is now found in site i and a particle from site i is now in site $i+1$. The third term describes the inverse of the above site relabelling, i.e. $i \to i-1$, which occurs whenever there is a decay event. The final term is the loss of a particle from site i with rate 1.

At sites 1 and 2, the dynamics at the lattice end result in different steady state equations. Here, we have:

$$\frac{d\langle\tau_1\rangle}{dt} = \langle[1-\tau_1]\mu\tau_2\rangle + \langle[1-\tau_1]p\lambda\rangle - \langle\tau_1\rangle = 0\ , \quad (5.2)$$

and

$$\frac{d\langle\tau_2\rangle}{dt} = \lambda\langle\tau_1[1-\tau_2]\rangle - \langle[1-\tau_1]p\lambda[\tau_2]\rangle + \langle[1-\tau_1]\mu[\tau_3-\tau_2]\rangle - \langle\tau_2\rangle = 0\ . \quad (5.3)$$

Equation 5.3 is identical to the Equation for a general site i (5.1), except that here the values of τ_1 in the first and second terms are predetermined by the conditions for growth.

In the reference frame of the lab, the tip of the lattice (site 1) advances and recedes as units are added and subtracted. One can derive an expression for the average velocity at which the lattice tip progresses, from the combined rates of lattice growth and decay. The rate at which units are added to the lattice is dependent on the occupancy at site 1, $\langle\tau_1\rangle$ and the rates p and λ. It is given by:

$$v_g = \lambda\langle\tau_1\rangle + p\lambda\langle 1-\tau_1\rangle\ . \quad (5.4)$$

The condition for units to be subtracted from the lattice is that site 1 is unoccupied. The rate of decay of an unoccupied site 1 is μ. The total rate at which units are subtracted from the lattice is thus given by:

$$v_d = \mu\langle 1-\tau_1\rangle \ . \tag{5.5}$$

The total tip velocity may therefore be expressed:

$$v_T = v_g - v_d = \lambda\langle\tau_1\rangle + p\lambda\langle 1-\tau_1\rangle - \mu\langle 1-\tau_1\rangle \ . \tag{5.6}$$

For a positive overall velocity, we have from (5.6), the requirement that:

$$\langle\tau_1\rangle > \frac{\mu - p\lambda}{\lambda + \mu - p\lambda} \ . \tag{5.7}$$

To find the constraints that this requirement imposes on the model parameters μ, λ, and p, we must first find an expression for $\langle\tau_1\rangle$ in terms of these parameters.

5.1.2 Simple mean-field approximation

As we did in previous Chapters, we take a simple mean-field approximation $\langle\tau_i\tau_j\rangle = \rho_i\rho_j$. We have from (5.1):

$$\lambda\rho_1(\rho_{i-1}-\rho_i) + \mu(1-\rho_1)(\rho_{i+1}-\rho_i) + p\lambda(1-\rho_1)(\rho_{i-1}-\rho_i) - \rho_i = 0 \ , \tag{5.8}$$

which, using definitions (5.4) and (5.5), we may write as:

$$v_g(\rho_{i-1}-\rho_i) + v_d(\rho_{i+1}-\rho_i) - \rho_i = 0 \quad i \geq 3 \ . \tag{5.9}$$

Likewise, Equations 5.3 and 5.2 become:

$$\lambda\rho_1 - v_g\rho_2 + v_d[\rho_3 - \rho_2] - \rho_2 = 0 \ , \tag{5.10}$$

and

$$v_d\rho_2 + (1-\rho_1)p\lambda - \rho_1 = 0 \ . \tag{5.11}$$

5.1.3 Second order recursion relation

We can assume that the second order recursion relation (5.9) has solution:

$$\rho_i = Az^{i-2} \tag{5.12}$$

Substituting this into (5.9) with $i = 3$, we have then a quadratic in z:

$$v_g(1-z) + v_d(z^2 - z) - z = 0 \tag{5.13}$$

This has solutions:

$$z^{\pm} = \frac{1 + v_g + v_d \pm \sqrt{(1 + v_g + v_d)^2 - 4v_g v_d}}{2v_d} \tag{5.14}$$

For a physical solution, we require that $z < 1$. Therefore the lower root is the physical solution.

5.1.4 A theoretical phase transition

We are interested in using the formulation above to identify the point at which a transition occurs between a microtubule that is growing with a positive average velocity and one which remains a finite size. From (5.7), we see that this transition occurs at

$$\rho_1 = \frac{\mu - p\lambda}{\lambda + \mu - p\lambda} \; . \tag{5.15}$$

Let us consider the simple case of $p = 1$. This is equivalent to assuming that the occupancy at site 1 does not affect the rate at which new units are added. Although this is not in general true for real microtubules, it is of theoretical interest to first solve in this limit as it allows us to greatly simplify the equations of the previous sections. At the phase transition, the growth rate and decay rate are equal, and we have from (5.4) and (5.5):

$$v_g = v_d = \lambda \; . \tag{5.16}$$

The *critical* ρ_1 is given from Equation 5.15:

$$\rho_1^c = \frac{\mu - \lambda}{\mu} \; , \tag{5.17}$$

and using (5.16), we obtain the critical values for ρ_2 and ρ_3 from (5.11) and (5.10):

$$\begin{aligned} \lambda\rho_2 + (1 - \rho_1)\lambda - \rho_1 &= 0 \\ \Rightarrow \lambda\rho_2 + \frac{\lambda^2}{\mu} - \frac{\mu - \lambda}{\mu} &= 0 \\ \Rightarrow \mu\lambda\rho_2 + \lambda^2 - \mu + \lambda &= 0 \\ \Rightarrow \rho_2^c &= \frac{\mu - \lambda^2 - \lambda}{\mu\lambda} \end{aligned} \tag{5.18}$$

$$\begin{aligned} \lambda\rho_1 - \lambda\rho_2 + \lambda(\rho_3 - \rho_2) - \rho_2 &= 0 \\ \Rightarrow \quad - 2\lambda\rho_2 + \lambda\rho_3 - \rho_2 &= 0 \end{aligned}$$

$$\Rightarrow \rho_3^c = \frac{1}{\mu\lambda^2}[\lambda^3 - (3 - \mu)\lambda^2 + (2\mu - 1)\lambda + \mu] \tag{5.19}$$

Now from (5.12) we may solve the second order recursion relation using $\rho_2 = A$, $\rho_3 = Az$

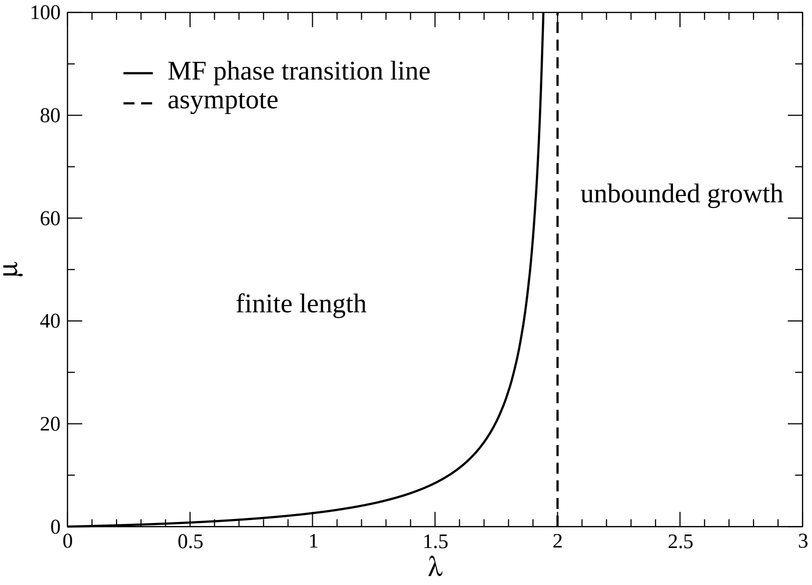

Figure 5.2: The solution for μ as a function of λ on the transition line between growing and finite length regimes (5.21). Note the singularity at $\lambda = 2$

and with the critical z from the lower (physical) root in Equation 5.14:

$$z^c = \frac{1 + 2\lambda - \sqrt{1 + 4\lambda}}{2\lambda} \,. \tag{5.20}$$

From (5.12), we have

$$\rho_2 = \frac{\rho_3}{z} \,,$$

and thus, from (5.18) and (5.19), we obtain an expression for μ on the phase boundary:

$$\mu = \frac{2\lambda}{3 - \sqrt{(1 + 4\lambda)}}. \tag{5.21}$$

This curve is presented in Figure 5.2. Note that a singularity occurs at $\lambda = 2$. For $\lambda > 2$ the theory predicts that the microtubule will grow regardless of the detachment rate.

This crude analysis has led us rather rapidly to an apparent result, namely a line in μ–λ space which marks the transition where a microtubule should switch between a state of finite length fluctuations, and an indefinitely growing state. The presence of an asymptote in this function at $\lambda = 2$, however, is quite counterintuitive and deserves some careful scrutiny.

5.2 Monte Carlo simulation

A simulation of the full model dynamics is implemented with a straightforward Monte Carlo algorithm. We use a Boolean array to represent the microtubule, with 1 representing

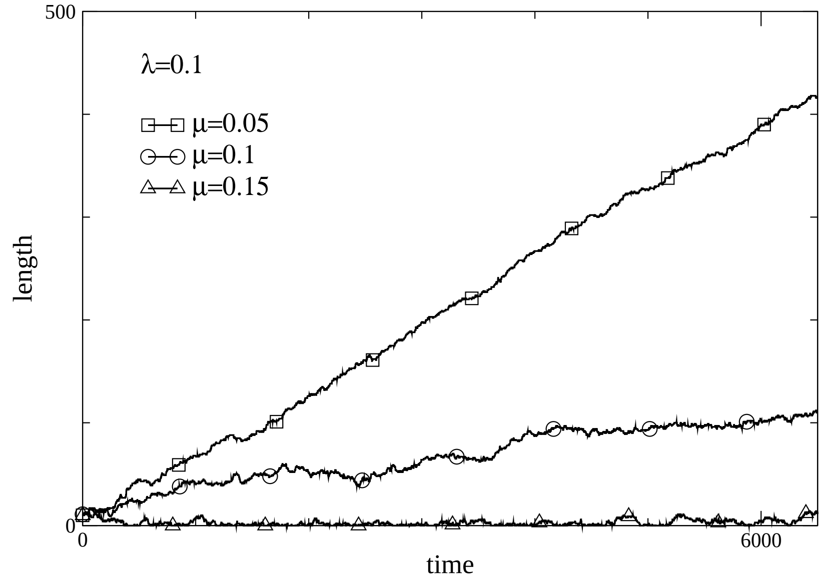

Figure 5.3: Microtubule length plotted for different decay rates, illustrating unbounded growth (squares and circles) for low μ, and bounded fluctuations (triangles) for higher μ.

GTP and 0 representing GDP. The array is extended and reduced stochastically, according to the GTP–GDP dynamics prescribed above.

The algorithm allows us to investigate the exact particle dynamics of this system. In particular, we are able to determine the microtubule's state of growth across the λ–μ phase space, and make an analysis of the validity of the mean-field prediction of a phase transition between growing and finite length regimes, presented above.

Figure 5.3 shows three trajectories of a microtubule's length plotted against time. The growth is rate low ($\lambda = 0.1$), and is the same in each case, while the decay rate is varied between 0.05–0.15. One can see that for a low decay rate, although there are fluctuations due to the stochastic nature of the model, the microtubule grows in an approximately linear fashion. In this parameter regime, the decay of the microtubule is slow when the GTP-cap is lost, and before any significant decrease in size occurs, the GTP-cap is reformed and growth resumes. The intermediate microtubule is also in a growing state, although the growth velocity has reduced due to the higher decay rate. The decay rate is still not high enough in this case to reduce the length of the microtubule back to zero. The trajectory for the microtubule with highest μ is in a finite length state. The fluctuations frequently reduce the microtubule to a length of zero and it never grows beyond a length of approximately 15 units.

As the rates of growth and decay increase, so too does the scale of the length fluctuations. For a very high rate of decay, we see in Figure 5.4, a more dramatic structure to the microtubule dynamics. The microtubule's length trajectory is now characterised by distinct periods of growth, interspersed with periods of sudden drastic decay. This bears

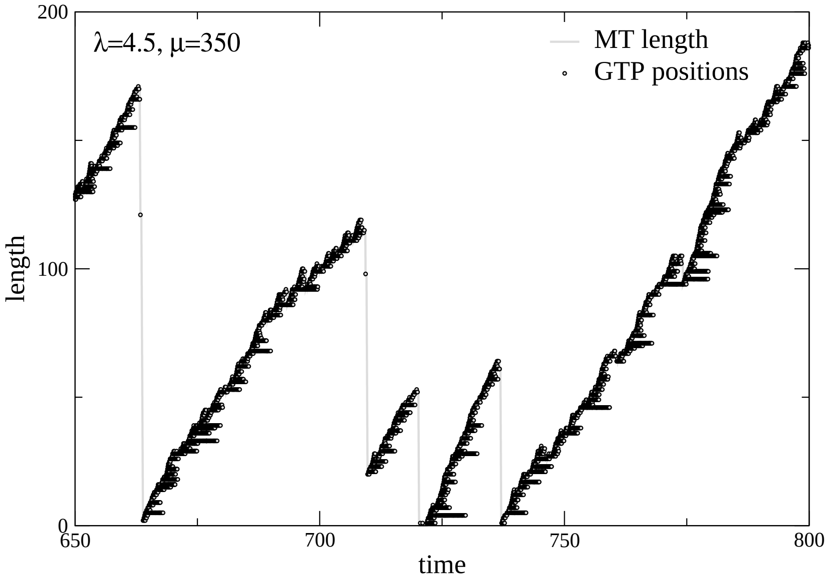

Figure 5.4: The length with time plot of a microtubule for the parameter values within the unlimited growth regime of the mean-field theory (indicated with a star on Figure 5.7). The position of GTPs are also shown. One can see that although the conversion rate is slow compared to the growth and decay, the effect when the GTP cap disappears is drastic and results in a catastrophe where the microtubule is reduced to a length of zero.

some resemblance to the growth and catastrophe dynamics of experimental observations (See Figure 2.8 in Chapter 2), although note that in general the growth of a microtubule will resume before its length has shrunk all the way to zero.

5.2.1 Phase behaviour

Small λ and μ

We first consider simulations of the microtubule dynamics, run over the parameter range $0 < \mu < 1$, $0 < \lambda < 1$. To identify the transition, we must be able to distinguish between growing and finite length microtubules. Clearly, a growing microtubule will have increased in length after a large time interval. However, a finite microtubule fluctuates in length wildly, so depending on its original length, a measurement after a large time interval may return a growing or a shrinking verdict. To clarify the distinction then, we start our simulations with a very large microtubule length (larger than the maximum length that can be reached from zero within this time interval, for this parameter range). By effectively removing the lower bound for the microtubule length (zero), we allow for a downward trend in the length of any microtubule which is not growing.

The results are illustrated in Figure 5.5. Those microtubules which grew on average during the simulation run are indicated with pluses, while those which did not grow are indicated with filled circles. One can see that the transition between the growing and finite

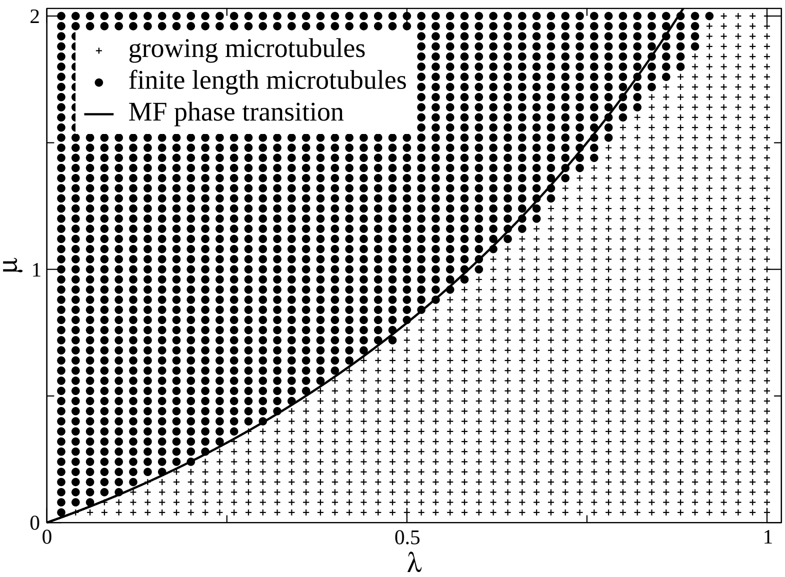

Figure 5.5: Comparison of simulation results with theory. Growing microtubules are indicated with pluses, while shrinking microtubules are indicated with crosses. The theoretical transition between these phases (5.21) is also plotted.

length microtubules follows a smooth curve. The mean-field transition (5.21) is shown on the plot for comparison and appears to be quite close to the simulation data in this range, particularly for small λ and μ.

Large λ and μ

For $\lambda > 1$ however, the simulation results diverge from the predicted mean-field phase transition and in particular they do not show any singularity at $\lambda = 2$. The results for $0 < \lambda < 4$ are shown in Figure 5.6, where we see that the transition line follows an exponential curve, rather than the asymptotic curve predicted by the mean-field theory. This means that in the region where the mean-field theory predicted growth regardless of decay rate ($\lambda > 2$), the microtubule length is in fact still able to remain finite, provided that the decay rate μ is high enough.

A fit to the data of Figure 5.6 indicates a transition line of:

$$\mu \approx e^{\frac{2\pi\lambda}{7.85}} \, . \tag{5.22}$$

In Figure 5.6, for comparison, we plot the mean-field transition line alongside (5.22), and the phase transition line for $\mu \to \infty$ found in [Antal 07b]. The star in Figure 5.7 indicates the parameter values for which the trajectory of Figure 5.4 was calculated. One can see that this data point is well inside the region of unbounded growth predicted by our mean-field theory. The phase transition predicted in the limit $\mu \to \infty$ in [Antal 07b] also suggests this point is within the growing region of the phase diagram. However, looking

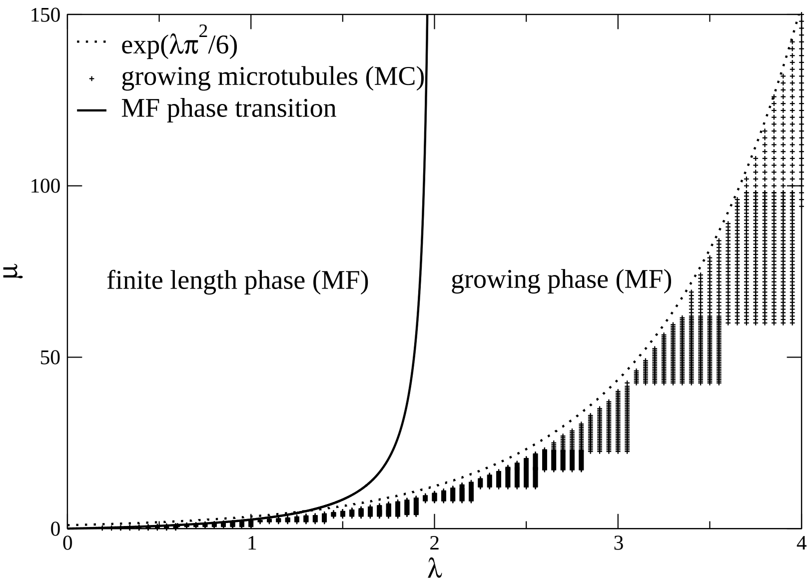

Figure 5.6: Data points for microtubules in the growing phase are indicated with crosses. The phase transition appears to follow an exponential curve, shallower than that of the mean-field prediction. No singularity occurs at $\lambda = 2$.

back at Figure 5.4, it is clear that in this region the microtubule remains of finite length. This is due to the high decay rate (μ), which results in frequent catastrophes that rapidly return the microtubule length to zero.

5.3 Conclusion

We have extended the analysis of [Antal 07b] to find a general expression for a phase transition between a growing and a finite length microtubule. Whereas the approximate phase transition in [Antal 07b] is found by considering the limits $\mu \to \infty$ and $\mu \to 0$, our mean-field approach provides a phase transition line for general values of the parameters μ and γ.

Our approach is similar to that of the previous two chapters, i.e. we use a lattice based model, and solve correlation equations constructed in the reference frame of the dynamic end of the lattice. The equations are then treated with a mean-field approximation. By comparing to Monte Carlo simulation, it is found that the phase transition found in this manner appears to be accurate for small λ and μ, but it is not good at describing the 'catastrophes' which occur at high μ.

The problem in the regime of high μ is slightly subtle, and we believe it lies with the underlying principle of the mean-field approximation. This type of approximation naturally describes an average over many instances of the quantity of interest; in this case the density of GTP on a microtubule. In this way, any occurrence of GTP at the tip, no matter how infrequent, will result in a non-zero density, and thus the *effect* of a GTP cap.

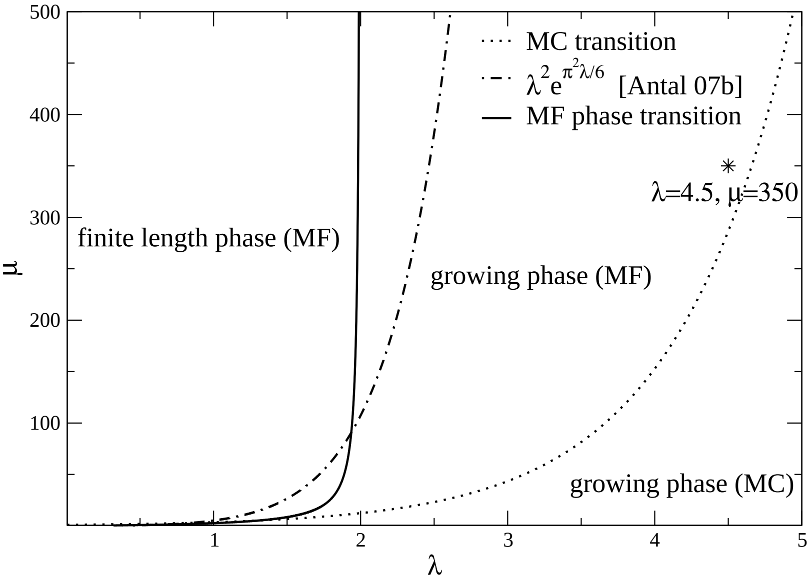

Figure 5.7: The point indicated corresponds to the parameters for a microtubule trajectory (see Figure 5.4) which was clearly in the 'finite length' phase. The mean-field phase transition is plotted, alongside the result for the limit $\mu \to \infty$ of [Antal 07b]. One can see that both theories predict the point to be well within the growing phase. The mean-field theory predicts growth because λ is greater than the conversion rate of GTP→GDP, but it fails to capture the nature of the *catastrophes* which are the mechanism by which the microtubules remain at finite length in the regime of high μ. The catastrophes can be seen for high μ in Figure 5.4.

At high μ this *effective* GTP-cap protects the microtubule from the catastrophic decay that would occur should the tip lose its cap entirely.

The inaccuracy of the mean-field approximation at high μ limits the practical use of our result, since the reality of microtubule dynamic instability (see, e.g., Figure 2.8) appears to coincide with the high μ regime of the model. In the regime of high μ it is necessary to employ a theory which is better suited to describing the rare events which shape the long term behaviour of the microtubule (i.e. the catastrophes, which keep it at a finite length). Indeed, the approach taken in [Antal 07b], where an analysis is made in the limit of $\mu \to \infty$ of the statistical 'waiting time' between catastrophes provides a result which is at least qualitatively closer to the actual behaviour than that predicted by our mean-field theory. Finding an accurate phase transition for general parameter values however remains an analytical challenge.

Although the success of our result is limited to a small parameter range, this work on the GTP-cap model serves to illustrate how one can use the techniques developed in Chapter 3 to probe a quite different problem.

Chapter 6

Summary and Conclusion

Let us first summarise what has been studied in this thesis. The primary theme was a study of how the microscopic constituents inside a fungal hypha contribute to and control the growth dynamics of the hypha. This study was made with a one-dimensional lattice model, of the type typically used to study transport phenomena in nonequilibrium statistical physics. The mass being transported through a hypha by the action of molecular motors was represented by particles, which performed stochastic hops along a lattice in a single direction, subject to mutual exclusion: a so-called totally asymmetric simple exclusion process. The novel feature of this model, that was introduced especially to deal with this particular problem, was the action of the particles when they reach the end of the lattice. Here, the particles cause the extension of the lattice, with one particle able to create a single lattice site. Thus we make an explicit connection between the arrival of mass to the end of the hypha, and the resulting growth of the hypha.

Our first objective was to characterise the steady state behaviour of this system, which was done with a mean-field approximation approach. Four qualitative phases were identified, including three phases observed previously in TASEP based models, and one phase: a *dynamic shock phase*, which is unique to this model. The theoretical study then progressed to a more detailed mean-field analysis, which we call the *refined mean-field theory*. This theory recognises that the correlations between the two sites closest to the lattice tip are significant and therefore the treatment of the exact correlation equations for the system under this approximation scheme does not require a factorisation of the correlations between these two sites. The result of the refined mean-field theory is a new phase diagram with slightly modified phase boundaries. A further refined theory is explored, which respects the correlations between the first three sites behind the lattice tip, again resulting in a phase diagram with modified boundaries. The mean-field theories are compared and discussed with respect to an heuristic argument, which appeals to the symmetry of the problem and makes a connection between our model and another TASEP-based model in the literature [Lakatos 03], that has similar macroscopic properties.

The merit of the theoretical approach is put to the test with a numerical analysis of the model, using Monte Carlo simulations. We are able to confirm the existence of all four of the predicted phases and, in particular, we find that the phase diagram predicted by the refined mean-field theory is strikingly close to the results from simulation.

We followed this in Chapter 5, with an extension to the model of Chapter 3, intended to more accurately describe the nature of the dynamics occurring within a growing fungal hypha as mass makes its way toward the tip. The extended model includes a description of the mass diffusion in the cytoplasm which surrounds the microtubule tracks, as well as the active transport processes on the microtubules which were already incorporated into the model. We treat the model as before, with a mean-field analysis, followed by a Monte Carlo assisted assessment of the theoretical results. In this case, we observe new structure to the steady state density profiles, including the formation of a stationary shock and phase coexistence for a range of parameters.

Chapter 6 saw the study of a second problem inspired by biology, also concerning with microtubules, though this time it is the dynamic growth and decay of the microtubules themselves that is the focus. Microtubules are highly dynamic structures and a great deal of attention has been given to the characterisation of the processes which lead to their observed dramatic changes in length. We do not propose a new model here, but rather present a brief study of an existing model, drawing from the techniques employed in the previous chapter. We thus suppose a lattice type representation of the model and again appeal to a mean-field approximation. We derive a transition line in the phase space of the model which bounds regions where a microtubule grows indefinitely, and where a microtubule remains of a finite length in the large time limit. Our result is concise, but does not succeed in describing the rare but catastrophic decay events that can take place at high γ and μ. The mean-field theory predicts an asymptotic phase boundary, resulting in a value for γ above which no finite length microtubules are possible. The asymptote is not present in simulation results, indicating that accuracy of the mean-field approximation for this system is limited to cases where the parameters γ and μ are small.

In conclusion, the progress made here has been primarily theoretical in nature. We have shown that the well-known TASEP can be generalised to a system that is increasing in length. We have illustrated a technique of solving for the steady state in a reference frame other than that in which the dynamics are defined and we have developed a refined mean-field method for dealing with strong correlations between particular sites in the lattice. Our study of the DEEP also provided us with a new perspective with which to tackle a second problem: the GTP-cap model for dynamic instability of microtubules, and here we were able to derive a general and novel result. We have thus provided through this work, a simple framework which may find application in a broader context. Indeed, there are many more systems that can be found in nature, where the boundaries are not spatially fixed, and where an analysis of the type seen in this thesis could be applied. One example attracting interest recently, is the extraction (by molecular motors) of membrane nanotubes [Derenyi 07, Campás 08, Tailleur 08].

The present models can also be developed to incorporate more biological detail of the system they are describing. For example, it could prove fruitful to study the effects of allowing larger sizes of vesicle in the DEEP dynamics, like was done for the TASEP in [Lakatos 03] and [Pierobon 06]. One may also find new and interesting effects by introducing heterogeneity and disorder on the lattice [Evans 04]. Another approach might be to incorporate ‘hyphal branching’ into the model for fungal hyphal growth, whereby new hyphal tips can be initiated from the parent hypha [Prosser 94].

It is important to note however, that for the models studied in this work to be considered seriously within their respective biological contexts, close cooperation with experimentalists is required. For example, we may have shown with the DEEP and its more detailed DEEP-SSEP extension, that the nonequilibrium physics of mass transport, coupled to system growth, can lead to steady states with an accumulation of mass near the dynamic end of the system; but to understand whether the observed Spitzenkörper in a fungal hypha could be the result of such a process, we must be able to obtain measured quantities corresponding to the parameters of our models. This would allow us to test the model hypotheses of, e.g., different density and velocity steady state phases controlled by the vesicle input and fusion rates.

As the methods of physics have great potential for contributing to our biological understanding, so too can biology contribute to our understanding of physics, by providing an endless source of fascinating problems that can be brought down on some level to simple physical interactions. Through the study of simple models for these systems, we gain both novel perspectives for understanding the biological phenomena, and a broader understanding of the subtleties of nonequilibrium processes generally. The apparent key to progress in this interdisciplinary area, is the construction and maintenance of genuine and tangible links between the biology and the theoretical approaches.

Bibliography

[Antal 07a] T. Antal, PL Krapivsky & S. Redner. *Dynamics of microtubule instabilities.* J. Stat. Mech, vol. 5004, 2007.

[Antal 07b] T. Antal, PL Krapivsky, S. Redner, M. Mailman & B. Chakraborty. *Dynamics of an idealized model of microtubule growth and catastrophe.* Physical Review E, vol. 76, no. 4, page 41907, 2007.

[Bartnicki-Garcia 89] S. Bartnicki-Garcia, F. Hergert & G. Gierz. *Computer simulation of fungal morphogenesis and the mathematical basis for hyphal (tip) growth.* Protoplasma, vol. 153, no. 1, pages 46–57, 1989.

[Bartnicki-Garcia 95] S. Bartnicki-Garcia, D.D. Bartnicki, G. Gierz, R. López-Franco & C.E. Bracker. *Evidence That Spitzenkörper Behavior Determines the Shape of a Fungal Hypha: A Test of the Hyphoid Model.* Experimental Mycology, vol. 19, no. 2, pages 153–159, 1995.

[Bartnicki-García 02] S. Bartnicki-García. *Hyphal tip growth: outstanding questions.* Molecular Biology of Fungal Development, pages 29–58, 2002.

[Bezzi 03] M. Bezzi & A. Ciliberto. *Mathematical modeling of filamentous microorganisms.* Comments on Theoretical Biology, vol. 8, pages 563–585, 2003.

[Blythe 01] R.A. Blythe. *A 2001 Nonequilibrium phase transitions and dynamical scaling regimes.* PhD thesis, University of Edinburgh, 2001.

[Blythe 07] RA Blythe & MR Evans. *Nonequilibrium steady states of matrix product form: a solver's guide.* J. Phys. A: Math. Theor, vol. 40, page 333, 2007.

[Bracker 97] C.E. Bracker, D.J. Murphy & R. Lopez-Franco. *Laser microbeam manipulation of cell morphogenesis growing in fungal hyphae.* In Proceedings of SPIE, volume 2983, page 67. SPIE, 1997.

[Bray 01] D. Bray. Cell Movements: From Molecules to Motility. Garland Publishing, 2001.

[Bundschuh 05] R. Bundschuh & U. Gerland. *Coupled dynamics of RNA folding and nanopore translocation.* Physical review letters, vol. 95, no. 20, pages 208104–208104, 2005.

[Burbank 06] Kendra S. Burbank & Timothy J. Mitchison. *Microtubule dynamic instability.* Current Biology, vol. 16, no. 14, pages R516 – R517, 2006.

[Campás 06] O. Campás, Y. Kafri, KB Zeldovich, J. Casademunt & J.F. Joanny. *Collective Dynamics of Interacting Molecular Motors.* Physical Review Letters, vol. 97, no. 3, page 38101, 2006.

[Campás 08] O. Campás, C. Leduc, P. Bassereau, J. Casademunt, J.F. Joanny & J. Prost. *Coordination of Kinesin Motors Pulling on Fluid Membranes.* Biophysical Journal, vol. 94, no. 12, page 5009, 2008.

[Cassimeris 88] L. Cassimeris. *Real-time observations of microtubule dynamic instability in living cells.* The Journal of Cell Biology, vol. 107, no. 6, pages 2223–2231, 1988.

[Chou 97]	T. Chou & G. Lakatos. *Clustered bottlenecks in mRNA translation and protein synthesis.* Proc. Natl. Acad. Sci. USA Phys Rev Lett, vol. 93, page 198101, 1997.
[Chowdhury 05]	D. Chowdhury, A. Schadschneider & K. Nishinari. *Physics of transport and traffic phenomena in biology: from molecular motors and cells to organisms.* Physics of Life Reviews, vol. 2, no. 4, pages 318–352, 2005.
[Chowdhury 08]	D. Chowdhury, A. Basu, A. Garai, P. Greulich, K. Nishinari, A. Schadschneider & T. Tripathi. *Intra-cellular traffic: bio-molecular motors on filamentary tracks.* The European Physical Journal B-Condensed Matter and Complex Systems, vol. 64, no. 3, pages 593–600, 2008.
[Collinge 74]	A.J. Collinge & APJ Trinci. *Hyphal tips of wild-type and spreading colonial mutants ofNeurospora crassa.* Archives of Microbiology, vol. 99, no. 1, pages 353–368, 1974.
[Crooks 99]	G.E. Crooks. *Entropy production fluctuation theorem and the nonequilibrium work relation for free energy differences.* Physical Review E, vol. 60, no. 3, pages 2721–2726, 1999.
[Davidson 07]	F.A. Davidson. *Mathematical modelling of mycelia: a question of scale.* Fungal Biology Reviews, vol. 21, no. 1, pages 30–41, 2007.
[Deacon 06]	J. Deacon. Fungal Biology. Blackwell Publishers, 2006.
[Derenyi 07]	I. Derenyi, G. Koster, MM van Duijn, A. Czovek, M. Dogterom & J. Prost. *Membrane nanotubes.* Lecture notes in physics -New York then Berlin-, vol. 711, page 141, 2007.
[Derrida 92]	B. Derrida, E. Domany & D. Mukamel. *An exact solution of a one-dimensional asymmetric exclusion model with open boundaries.* Journal of Statistical Physics, vol. 69, no. 3, pages 667–687, 1992.
[Derrida 93]	B. Derrida, MR Evans, V. Hakim & V. Pasquier. *Exact solution of a 1D asymmetric exclusion model using a matrix formulation.* J. Phys. A: Math. Gen, vol. 26, no. 1493-1517, page 21, 1993.
[Derrida 01]	B. Derrida, JL Lebowitz & ER Speer. *Free Energy Functional for Nonequilibrium Systems: An Exactly Solvable Case.* Physical Review Letters, vol. 87, no. 15, page 150601, 2001.
[Derrida 02]	B. Derrida, JL Lebowitz & ER Speer. *Large Deviation of the Density Profile in the Steady State of the Open Symmetric Simple Exclusion Process.* Journal of Statistical Physics, vol. 107, no. 3, pages 599–634, 2002.
[Desai 97]	A. Desai & T.J. Mitchison. *Microtubule polymerization dynamics.* Annual review of cell and developmental biology, vol. 13, no. 1, pages 83–117, 1997.
[Deutsch 05]	A. Deutsch & S. Dormann. Cellular automaton modeling of biological pattern formation: characterization, applications, and analysis. Birkhauser, 2005.
[Dogterom 05]	M. Dogterom, J.W.J. Kerssemakers, G. Romet-Lemonne & M.E. Janson. *Force generation by dynamic microtubules.* Current Opinion in Cell Biology, vol. 17, no. 1, pages 67–74, 2005.
[Dong 07]	J.J. Dong, B. Schmittmann & R.K.P. Zia. *Towards a model for protein production rates.* Journal of Statistical Physics, vol. 128, no. 1, pages 21–34, 2007.
[Egelman 07]	E.H. Egelman. *Prolegomena to Any Future Biophysics (with apologies to I. Kant).* Biophysical Journal, 2007.

[Evans 00] MR Evans. *Phase transitions in one-dimensional nonequilibrium systems.* Brazilian Journal of Physics, vol. 30, pages 42–57, 2000.

[Evans 02] MR Evans & RA Blythe. *Nonequilibrium dynamics in low-dimensional systems.* Physica A: Statistical Mechanics and its Applications, vol. 313, no. 1-2, pages 110–152, 2002.

[Evans 03] MR Evans, R. Juhász & L. Santen. *Shock formation in an exclusion process with creation and annihilation.* Physical Review E, vol. 68, no. 2, page 26117, 2003.

[Evans 04] ME Evans, T. Hanney & Y. Kafri. *Disorder and non-conservation in a driven diffusive system.* Physical Review E, vol. 70, no. 6, 2004.

[Ferguson 03] BA Ferguson, TA Dreisbach, CG Parks, GM Filip & CL Schmitt. *Coarse-scale population structure of pathogenic Armillaria species in a mixed-conifer forest in the Blue Mountains of northeast Oregon.* Canadian Journal of Forest Research/Revue Canadienne de Recherche Forestiere, vol. 33, no. 4, pages 612–623, 2003.

[Feynman 98] R.P. Feynman. Statistical Mechanics: A Set of Lectures. Perseus Books, 1998.

[Fischer 08] R. Fischer, N. Zekert & N. Takeshita. *Polarized growth in fungi-interplay between the cytoskeleton, positional markers and membrane domains.* Molecular Microbiology, vol. 68, no. 4, pages 813–826, 2008.

[Galagan 03] J.E. Galagan, S.E. Calvo, K.A. Borkovich, E.U. Selker, N.D. Read, D. Jaffe, W. FitzHugh, L.J. Ma, S. Smirnov, S. Purcell*et al. The genome sequence of the filamentous fungus Neurospora crassa.* Nature, vol. 422, pages 859–868, 2003.

[Gierz 01] G. Gierz & S. Bartnicki-Garcia. *A Three-Dimensional Model of Fungal Morphogenesis Based on the Vesicle Supply Center Concept.* Journal of Theoretical Biology, vol. 208, no. 2, pages 151–164, 2001.

[Gillespie 77] D.T. Gillespie*et al. Exact stochastic simulation of coupled chemical reactions.* The Journal of Physical Chemistry, vol. 81, no. 25, pages 2340–2361, 1977.

[Girbardt 57] M. Girbardt. *Der Spitzenkörper von Polystictus versicolor (L.).* Planta, vol. 50, no. 1, pages 47–59, 1957.

[Gow 95] N.A.R. Gow, G.M. Gadd & I. NetLibrary. Growing Fungus. Netlibrary, 1995.

[Greulich 07] P. Greulich, A. Garai, K. Nishinari, A. Schadschneider & D. Chowdhury. *Intracellular transport by single-headed kinesin KIF1A: Effects of single-motor mechanochemistry and steric interactions.* Physical Review E, vol. 75, no. 4, page 41905, 2007.

[Grove 70] S.N. Grove & C.E. Bracker. *Protoplasmic Organization of Hyphal Tips Among Fungi: Vesicles and Spitzenkorper.* Journal of Bacteriology, vol. 104, no. 2, pages 989–1009, 1970.

[Harris 99] S.D. Harris, A.F. Hofmann, H.W. Tedford & M.P. Lee. *Identification and Characterization of Genes Required for Hyphal Morphogenesis in the Filamentous Fungus Aspergillus nidulans.* Genetics, vol. 151, no. 3, pages 1015–1025, 1999.

[Harris 05] S.D. Harris, N.D. Read, R.W. Roberson, B. Shaw, S. Seiler, M. Plamann & M. Momany. *Polarisome Meets Spitzenkorper: Microscopy, Genetics, and Genomics Converge*, 2005.

[Heath 99] I.B. Heath & G. Steinberg. *Mechanisms of Hyphal Tip Growth: Tube Dwelling Amebae Revisited.* Fungal Genetics and Biology, vol. 28, no. 2, pages 79–93, 1999.

[Helbing 01] D. Helbing. *Traffic and related self-driven many-particle systems.* Reviews of Modern Physics, vol. 73, no. 4, pages 1067–1141, 2001.

[Hickey 05] P.C. Hickey, S.R. Swift, M.G. Roca & N.D. Read. *Live-cell imaging of filamentous fungi using vital fluorescent dyes and confocal microscopy.* Methods in microbiology, page 63, 2005.

[Hinsch 05] H. Hinsch, R. Kouyos & E. Frey. *From intracellular traffic to a novel class of driven lattice gas models.* In Traffic and Granular Flow, volume 5. Springer, 2005.

[Horio 05] T. Horio & B.R. Oakley. *The Role of Microtubules in Rapid Hyphal Tip Growth of Aspergillus nidulans.* Molecular Biology of the Cell, vol. 16, no. 2, pages 918–926, 2005.

[Howard 81] R.J. Howard. *Ultrastructural analysis of hyphal tip cell growth in fungi: Spitzenkorper, cytoskeleton and endomembranes after freeze-substitution.* Journal of Cell Science, vol. 48, no. 1, pages 89–103, 1981.

[Howard 02] J. Howard & RL Clark. *Mechanics of Motor Proteins and the Cytoskeleton.* Applied Mechanics Reviews, vol. 55, page B39, 2002.

[Howard 09] M. Howard. *Cell Division: Experiments and Modelling Unite to Resolve the Middle* . Current Biology, vol. 19, no. 2, pages R67–R69, 2009.

[Huang 87] K. Huang. Statistical mechanics. New York: Wiley, 2nd ed., 1987.

[Kavanagh 05] K. Kavanagh. Fungi: Biology and Applications. Wiley, 2005.

[Klein 05] G.A. Klein, K. Kruse, G. Cuniberti & F. Jülicher. *Filament Depolymerization by Motor Molecules.* Physical Review Letters, vol. 94, no. 10, page 108102, 2005.

[Klumpp 03] S. Klumpp & R. Lipowsky. *Traffic of Molecular Motors Through Tube-Like Compartments.* Journal of Statistical Physics, vol. 113, no. 1, pages 233–268, 2003.

[Koch 82] AL Koch, ML Higgins & RJ Doyle. *The role of surface stress in the morphology of microbes.* J Gen Microbiol, vol. 128, no. 5, pages 927–45, 1982.

[Kruse 05] K. Kruse, JF Joanny, F. Jülicher, J. Prost & K. Sekimoto. *Generic theory of active polar gels: a paradigm for cytoskeletal dynamics.* The European Physical Journal E-Soft Matter, vol. 16, no. 1, pages 5–16, 2005.

[Kurchan 07] J. Kurchan. *Non-equilibrium work relations.* Journal of Statistical Mechanics: Theory and Experiment, no. 07, page 07005, 2007.

[Lakatos 03] G. Lakatos & T. Chou. *Totally asymmetric exclusion processes with particles of arbitrary size.* Journal of Physics A Mathematical and General, vol. 36, no. 8, pages 2027–2041, 2003.

[Lässig 07] M. Lässig. *From biophysics to evolutionary genetics: statistical aspects of gene regulation.* BMC Bioinformatics, vol. 8, no. Suppl 6, page S7, 2007.

[Lighthill 55] MJ Lighthill & GB Whitham. *On Kinematic Waves. II. A Theory of Traffic Flow on Long Crowded Roads.* Proceedings of the Royal Society of London. Series A, Mathematical and Physical Sciences (1934-1990), vol. 229, no. 1178, pages 317–345, 1955.

[Lipowsky 01] R. Lipowsky, S. Klumpp & T.M. Nieuwenhuizen. *Random Walks of Cytoskeletal Motors in Open and Closed Compartments.* Physical Review Letters, vol. 87, no. 10, page 108101, 2001.

[Löpez-Franco 96] R. Löpez-Franco & C.E. Bracker. *Diversity and dynamics of the Spitzenkörper in growing hyphal tips of higher fungi.* Protoplasma, vol. 195, no. 1, pages 90–111, 1996.

[MacDonald 68] CT MacDonald, JH Gibbs & AC Pipkin. *Kinetics of biopolymerization on nucleic acid templates.* Biopolymers, vol. 6, no. 1, pages 1–5, 1968.

[Mitchison 84] T. Mitchison & M. Kirschner. *Dynamic instability of microtubule growth.* Nature, vol. 312, no. 5991, pages 237–242, 1984.

[Mouriño-Pérez 06] R.R. Mouriño-Pérez, R.W. Roberson & S. Bartnicki-García. *Microtubule dynamics and organization during hyphal growth and branching in Neurospora crassa.* Fungal Genetics and Biology, vol. 43, no. 6, pages 389–400, 2006.

[Mukamel 00] D. Mukamel. *Soft and Fragile Matter: Nonequilibrium Dynamics.* Metastability and Flow, pages 237–58, 2000.

[Newman 99] M.E.J. Newman & GT Barkema. Monte Carlo Methods in Statistical Physics. Oxford University Press, USA, 1999.

[Nishinari 05] Katsuhiro Nishinari, Yasushi Okada, Andreas Schadschneider & Debashish Chowdhury. *Intracellular Transport of Single-Headed Molecular Motors KIF1A.* Physical Review Letters, vol. 95, no. 11, page 118101, 2005.

[Palla 05] G. Palla, I. Derenyi, I. Farkas & T. Vicsek. *Uncovering the overlapping community structure of complex networks in nature and society.* Nature, vol. 435, pages 814–818, 2005.

[Parmeggiani 03] A. Parmeggiani, T. Franosch & E. Frey. *Phase Coexistence in Driven One-Dimensional Transport.* Physical Review Letters, vol. 90, no. 8, page 86601, 2003.

[Parmeggiani 04] A. Parmeggiani, T. Franosch & E. Frey. *Totally asymmetric simple exclusion process with Langmuir kinetics.* Physical Review E (Statistical, Nonlinear, and Soft Matter Physics), vol. 70, no. 4, page 046101, 2004.

[Physbio 07] Physbio. PHYSBIO summer school: "Non-equilibrium in Physics and in Biology". August 2007.

[Pierobon 06] P. Pierobon, E. Frey & T. Franosch. *Driven lattice gas of dimers coupled to a bulk reservoir.* Physical review. E, Statistical, nonlinear, and soft matter physics, vol. 74, no. 3, 2006.

[Privman 97] V. Privman. Nonequilibrium Statistical Mechanics in One Dimension. Cambridge University Press, 1997.

[Prosser 94] JI Prosser. *Kinetics of filamentous growth and branching.* The growing fungus, pages 301–18, 1994.

[Regalado 97] C.M. Regalado. *Aggregation and collapse of fungal wall vesicles in hyphal tips: a model for the origin of the Spitzenkörper.* Philosophical Transactions of the Royal Society B: Biological Sciences, vol. 352, no. 1364, pages 1963–1974, 1997.

[Reichenbach 06] T. Reichenbach, T. Franosch & E. Frey. *Exclusion Processes with Internal States.* Physical Review Letters, vol. 97, no. 5, page 50603, 2006.

[Riquelme 98] M. Riquelme, C.G. Reynaga-Peña, G. Gierz & S. Bartnicki-Garcia. *What Determines Growth Direction in Fungal Hyphae?* Fungal Genetics and Biology, vol. 24, no. 1-2, pages 101–109, 1998.

[Riquelme 00] M. Riquelme, G. Gierz & S. Bartnicki-Garcia. *Dynein and dynactin deficiencies affect the formation and function of the Spitzenkorper and distort hyphal morphogenesis of Neurospora crassa*, 2000.

[Riquelme 07] M. Riquelme, S. Bartnicki-García, J.M. González-Prieto, E. Sánchez-León, J.A. Verdín-Ramos, A. Beltrán-Aguilar & M. Freitag. *Spitzenkörper Localization and Intracellular Traffic of Green Fluorescent Protein-Labeled CHS-3 and CHS-6 Chitin Synthases in Living Hyphae of Neurospora crassa?* Eukaryotic Cell, vol. 6, no. 10, pages 1853–1864, 2007.

[Ruelle 03] D. Ruelle. *Is there a unified theory of nonequilibrium statistical mechanics?* In Annales Henri Poincaré, volume 4, pages 489–495. Birkhäuser, 2003.

[Schuchardt 05] I. Schuchardt, D. Assmann, E. Thines, C. Schuberth & G. Steinberg. *Myosin-V, Kinesin-1, and Kinesin-3 Cooperate in Hyphal Growth of the Fungus Ustilago maydis.* Molecular Biology of the Cell, vol. 16, no. 11, pages 5191–5201, 2005.

[Schütz 93] G. Schütz & E. Domany. *Phase transitions in an exactly soluble one-dimensional exclusion process.* Journal of Statistical Physics, vol. 72, no. 1, pages 277–296, 1993.

[Seiler 97] S. Seiler, F.E. Nargang, G. Steinberg & M. Schliwa. *Kinesin is essential for cell morphogenesis and polarized secretion in Neurospora crassa.* The EMBO Journal, vol. 16, pages 3025–3034, 1997.

[Seiler 99] S. Seiler, M. Plamann & M. Schliwa. *Kinesin and dynein mutants provide novel insights into the roles of vesicle traffic during cell morphogenesis in Neurospora.* Current Biology, vol. 9, pages 779–785, 1999.

[Shaw 03] L.B. Shaw, RKP Zia & K.H. Lee. *Totally asymmetric exclusion process with extended objects: A model for protein synthesis.* Physical Review E, vol. 68, no. 2, page 21910, 2003.

[Stark 06] H. Stark & M. Reichert. *Synchronization of rotating flagella by hydrodynamic interactions.* In American Physical Society, APS March Meeting, March 13-17, 2006, abstract# A7. 002, 2006.

[Steinberg 93] G. Steinberg & M. Schliwa. *Organelle movements in the wild type and wall-less fzg3-1 mutants of Neurospora crassa are mediated by cytoplasmic microtubules.* J. Cell Sci, vol. 106, pages 555–564, 1993.

[Steinberg 07a] G. Steinberg. *Hyphal Growth: a Tale of Motors, Lipids, and the Spitzenkörper?* Eukaryotic Cell, vol. 6, no. 3, pages 351–360, 2007.

[Steinberg 07b] G. Steinberg. *Tracks for traffic: microtubules in the plant pathogen Ustilago maydis.* New Phytologist, vol. 174, no. 4, pages 721–733, 2007.

[Stinchcombe 01] R. Stinchcombe. *Stochastic non-equilibrium systems.* Advances in Physics, vol. 50, no. 5, pages 431–496, 2001.

[Szavits-Nossan 06] J. Szavits-Nossan & K. Uzelac. *Totally asymmetric exclusion process with long-range hopping.* Physical Review E, vol. 74, no. 5, page 51104, 2006.

[Tailleur 08] J. Tailleur, MR Evans & Y. Kafri. *Non-equilibrium phase transitions in tubulation by molecular motors.* Arxiv preprint arXiv:0812.0805, 2008.

[Tindemans 06] S.H. Tindemans, N. Kern & B.M. Mulder. *The diffusive vesicle supply center model for tip growth in fungal hyphae.* Journal of Theoretical Biology, vol. 238, no. 4, pages 937–948, 2006.

[ToL] *The tree of life project.* `www.tolweb.org/tree/`.

[Torralba 98] S. Torralba, M. Raudaskoski, AM Pedregosa & F. Laborda. *Effect of cytochalasin A on apical growth, actin cytoskeleton organization and enzyme secretion in Aspergillus nidulans.* Microbiology, vol. 144, no. 1, pages 45–53, 1998.

[Tsekouras 08] K. Tsekouras & AB Kolomeisky. *Parallel coupling of symmetric and asymmetric exclusion processes.* Journal of Physics A: Mathematical and Theoretical, vol. 41, no. 46, page 465001, 2008.

[Vargas 93] MM Vargas, JM Aronson & RW Roberson. *The cytoplasmic organization of hyphal tip cells in the fungus Allomyces macrogynus.* Protoplasma, vol. 176, no. 1-2, pages 43–52, 1993.

[Wessels 86] JGH Wessels. *Cell wall synthesis in apical hyphal growth.* International review of cytology, vol. 104, pages 37–79, 1986.

[Wessels 94] JGH Wessels. *Developmental Regulation of Fungal Cell Wall Formation.* Annual Reviews in Phytopathology, vol. 32, no. 1, pages 413–437, 1994.

[Wright 07] G.D. Wright, J. Arlt, W.C.K. Poon & N.D. Read. *Optical tweezer micromanipulation of filamentous fungi.* Fungal Genetics and Biology, vol. 44, no. 1, pages 1–13, 2007.

[Wu 98] Q. Wu, T.M. Sandrock, B.G. Turgeon, O.C. Yoder, S.G. Wirsel & J.R. Aist. *A Fungal Kinesin Required for Organelle Motility, Hyphal Growth, and Morphogenesis.* Molecular Biology of the Cell, vol. 9, no. 1, pages 89–101, 1998.

[Zong 06] C. Zong, T. Lu, T. Shen & P.G. Wolynes. *Nonequilibrium self-assembly of linear fibers: microscopic treatment of growth, decay, catastrophe and rescue.* Phys. Biol, vol. 3, pages 83–92, 2006.

Publications

K E P Sugden, M R Evans, W C K Poon and N D Read. Model of hyphal tip growth involving microtubule-based transport. In *Physical Review E*, vol. 75, no. 3, 2007.

M R Evans and K E P Sugden. An exclusion process for modelling fungal hyphal growth. In *Physica A: Statistical Mechanics and its Applications*, vol. 284, no. 1, pages 53–58, 2007.

K E P Sugden and M R Evans. A dynamically extending exclusion process. In *Journal of Statistical Mechanics: Theory and Experiment*, vol. 11 ,no. 11013, 2007.